MSc. Eng. Thanushree Suresh
Instytut Maszyn Przepływowych im. Roberta Szewalskiego
Polskiej Akademii Nauk
w Gdańsku

AEROACOUSTIC INVESTIGATION OF STREAMWISE VORTEX GENERATORS FOR FLOW CONTROL

Rozprawa doktorska przedłożona
Radzie Naukowej
Instytutu Maszyn Przepływowych im. Roberta Szewalskiego
Polskiej Akademii Nauk

Promotor:
Dr hab. inż. Paweł Flaszyński

Promotor pomocniczy:
Dr inż. Oskar Szulc

Gdańsk, *Październik 2023*

Acknowledgements

This research was supported by the European Union's Horizon 2020 research and innovation programme under the Marie Sklodowska-Curie grant agreement No. 722401-SmartANSWER, and by the CI TASK.

I would like to thank my supervisor Paweł Flaszyński for his immense support and guidance without which this work would not be possible. I express my gratitude for the valuable discussions and his continuous encouragement to undertake this work. I thank my co-supervisor Oskar Szulc for the instructive discussions and his encouragement to achieve perfection during this long journey. I would like to thank Prof. Piotr Doerffer for all his expert advice and guidance.

I would like to thank Daniele Ragni, Alejandro Rubio Carpio, Christopher Teruna and their team from Delft University of Technology for their immense support and guidance during the experimental campaign. I express my gratitude to all the supervisors and my fellow researchers in the SmartANSWER consortium for making this research a memorable learning experience.

I thank my colleagues – Michal for his support during numerical simulations and Marcin for his help during the manufacturing and conducting experiments. I express deep gratitude to Justyna from the Human Resource department for her invaluable support dealing with various administrative issues, which made my life easier in Gdansk. I would like to thank my colleagues – Filip, Januz, Nishchay, Shishir, Kaleesh for their valuable daily companionship and banter that made this work possible.

I express profound gratitude to my grandparents, parents, aunt, my siblings Lakshmi and Darshan for being my rock solid support and my cheerleaders through this journey. I thank them for making me the person I am and giving me the confidence to undertake adventurous and off the beaten paths. I thank my wonderful friends – Adam, Elenora, Manjunath, Sasha, Anubhav, Grace for making my life in Gdansk eventful and so memorable. I thank my friends Saul, Vatsal, Sunil and Aravind for their invaluable companionship and for going on impromptu vacations with me whenever I was overwhelmed. I thank my old friends Adeesh, Anurag, Sambhram and Pooja who have always been with me on this journey of life and been my comfort during hard times despite the various time zones.

Abstract

One of the main concerns of the renewable wind energy is their noise emissions, causing public reluctance for its widespread usage. Research into the sound emitted by wind turbine rotor blades specifically during the off-design operating condition such as the turbulent boundary layer flow separation is limited. A particular type of flow control device – the rod vortex generators (RVGs) have been investigated for separation reduction on wind turbines. However, their acoustic impact is unknown.

A fundamental understanding of the physics and mechanisms of sound generation and propagation that enables better design of noise mitigating flow control devices is the main objective of this research work. This was accomplished by developing a general, post-processing, aeroacoustic code for investigating sound predictions of rotating bodies in subsonic motion. It is based on the integral solution derived by Farassat to the exact Ffowcs-Williams and Hawkings (FW–H) acoustic analogy. The acoustic signal along with its various components (thickness, loading, near and far-field) are validated in great detail against the analytical solutions for elementary sources (monopole and dipole). Additionally, to obtain the analytical solutions, codes for both stationary/moving monopole and dipole were developed for single and distributed point sources. Thus, also enabling preliminary acoustic analysis for new projects.

The code is then utilized for the investigation of low frequency in-plane harmonic noise (LF-IPH) of a model helicopter rotor in hover. A good match of the predicted thickness noise with the literature (University of Maryland) was obtained. A detailed loading noise analysis was conducted through both Reynolds-averaged Navier-Stokes (RANS) simulations and Blade Element Momentum Theory (BEMT) methods. A satisfactory agreement with the signals from literature (another FW–H code) was obtained while the total pressure had the same agreement as the literature code with measurements.

The code is then used to investigate the impact of the RVGs on the noise emitted by the NREL Phase VI wind turbine rotor. The main focus of this investigation was the relative difference in the sound emitted (steady rotational noise) by the rotor blades with/without RVGs. Neither global nor local analysis showed any significant change in the overall sound pressure levels for both near and far-field microphones. Thus, the RVGs do not cause any significant noise penalty while improving aerodynamic performance by reducing turbulent boundary layer separation.

Since only steady rotational noise was analyzed for the NREL wind turbine rotor due to the limited availability of unsteady surface pressure data, the impact of the rods on the separation and broadband trailing edge noise for a wind turbine airfoil (DU96-W-180) was investigated through measurements. The impact of the rods on the boundary layer has been captured through various flow measurement techniques – surface pressure, oil flow visualization and Particle Image Velocimetry. Utilizing acoustic beamforming technique to analyze measurements from a microphone array, source identification and a comparitive analysis of sound pressure levels at various inflow angles (with separation) were conducted. A reduction in noise was achieved at low frequencies with RVGs implemented. However, the rods generate more broadband noise at mid and high frequencies. RVGs generate an additional self-noise only at higher frequencies. The increase of noise levels by the rods are all within $\sim$2 dB and occurs at total sound pressure levels which are significantly lower than the peak values generated at low frequencies, thus, making it difficult for human perception specifically for wind turbine applications.

Streszczenie

Jednym z głównych problemów związanych z odnawialną energią wiatrową jest powiązana emisja hałasu, która powoduje niechęć społeczeństwa do jej powszechnego stosowania. Badania nad dźwiękiem emitowanym przez łopaty wirnika turbiny wiatrowej, szczególnie w warunkach pracy niezgodnych z projektem, takich jak w obecności oderwania przepływu w turbulentnej warstwie przyściennej, są ograniczone. Szczególny typ urządzenia do sterowania przepływem – prętowe generatory wirów wzdłużnych RVGs (ang. Rod Vortex Generators) badano pod kątem redukcji oderwania w zastosowaniu do łopat turbin wiatrowych. Jednak ich wpływ akustyczny nie jest poznany.

Głównym celem tej pracy badawczej jest podstawowe zrozumienie fizyki oraz mechanizmów wytwarzania i propagacji dźwięku, które umożliwią projektowanie urządzeń przeznaczonych do sterowania przepływem i ograniczających hałas turbin wiatrowych. Osiągnięto to poprzez opracowanie ogólnego kodu aeroakustycznego przeznaczonego do badania emisji i propagacji dźwięku, którego źródłem są ciała poruszające się z prędkością poddźwiękową w przestrzeni (np. rotacja). Opiera się na całkowym rozwiązaniu Farassata dla analogii akustycznej Ffowcsa-Williamsa i Hawkingsa (FW–H). Sygnał akustyczny wraz z jego różnymi składowymi jest szczegółowo sprawdzany (walidowany) w oparciu o rozwiązania analityczne opracowane dla elementarnych źródeł akustycznych (monopolowych i dipolowych). Dodatkowo, w celu uzyskania rozwiązań analitycznych, opracowano dodatkowe kody numeryczne, zarówno dla źródła monopolowego nieruchomego/wirującego, jak i dipolowego, dla źródeł punktowych i rozproszonych. Umożliwia to również wstępną analizę akustyczną dla nowych projektów.

Opracowany kod numeryczny jest następnie wykorzystywany do badania niskoczęstotliwościowego hałasu harmonicznego w płaszczyźnie rotacji (ang. LF-IPH – low-frequency in-plane rotor harmonic noise) modelu wirnika śmigłowca w zawisie (University of Maryland). Uzyskano zadowalające porównanie przewidywanego hałasu monopolowego z danymi literaturowymi. Szczegółową analizę hałasu obciążeniowego (dipolowego) przeprowadzono zarówno za pomocą symulacji RANS (ang. Reynolds-averaged Navier-Stokes), jak i metod BEMT (ang. Blade Element Momentum Theory). Uzyskano dobrą zgodność z sygnałami z literatury (względem kodu referencyjnego FW–H). W stosunku do wyników pomiarów całkowity poziom ciśnienia akustycznego był podobnie przewidywany w stosunku do kodu literaturowego.

Kod FW–H wykorzystuje się następnie do badania wpływu RVGs na hałas rotacyjny emitowany przez wirnik turbiny wiatrowej NREL Phase VI. Głównym celem tego badania była względna różnica w poziomie dźwięku emitowanego przez łopaty wirnika z/bez RVGs. Ani analiza globalna, ani lokalna nie wykazały znaczących różnic w ogólnych poziomach ciśnienia akustycznego zarówno dla mikrofonu bliskiego, jak i dalekiego pola. Zatem RVGs nie powodują podwyższenia poziomu hałasu rotacyjnego, poprawiając jednocześnie właściwości aerodynamiczne poprzez zmniejszenie oderwania turbulentnej warstwy przyściennej.

Ponieważ dla wirnika turbiny wiatrowej NREL Phase VI analizowano numerycznie jedynie hałas rotacyjny (ze względu na niedostępność danych obliczeniowych dotyczących niestacjonarnego pola ciśnienia na powierzchni łopat), wpływ generatorów wirów na emisję szerokopasmową płata DU96 turbiny wiatrowej zbadano za pomocą technik pomiarowych w Delft University of Technology. Wpływ prętów na warstwę przyścienną zbadano za pomocą różnych metod – rejestracji ciśnienia na powierzchni, wizualizacji olejowej i PIV (ang. Particle Image Velocimetry). Wykorzystując technikę kształtowania wiązki akustycznej (ang. acoustic beamforming) do analizy pomiarów dźwięku z układu mikrofonów, przeprowadzono analizę porównawczą dystrybucji źródeł akustycznych oraz poziomów ciśnienia akustycznego przy różnych kątach napływu (oderwanie). Dzięki wdrożeniu RVGs uzyskano redukcję hałasu przy niskich częstotliwościach. Jednakże pręty generują więcej szumu szerokopasmowego przy średnich i wysokich częstotliwościach. RVGs generują dodatkowy szum własny tylko przy wyższych częstotliwościach. Wzrost poziomu hałasu powodowanego przez pręty mieści się w granicach $\sim$2 dB i występuje przy całkowitych poziomach ciśnienia akustycznego, które są znacznie niższe niż wartości szczytowe generowane przy niskich częstotliwościach, co utrudnia percepcję, szczególnie w przypadku zastosowań w turbinach wiatrowych.

Contents

List of symbols

Constant and non-dimensional symbols

H	shape factor
He	Helmholtz number
K	data block
n	number of panel
N	number of samples/total number of panels
Q	formulation
s	source number
S	total number of sources
St	Strouhal number
y^+	non dimensional wall distance
β	volume fraction
η	source panel
σ	radiating surface

Scalar

A	source power, [W]
c	chord, [m]
c_0	speed of sound, [m/s]
C	cross spectral matrix, [Hz]
d	distance, [m]
D	diametre of the rods, [m]
e	relative error, %
f	frequency, [Hz]
F	force, [N]
h	height of the rods, [m]
H	height of the wind turbine rotor, [m]
I	intensity of sound, dB

L	spanwise length of the section, length scale, beamformer output [m]
m	mass, [kg]
p	acoustic pressure, [Pa]
r	distance between the source and observer, [m]
R	arm of rotation, radius, [m]
t	observer time,time-step, [s]
T	time period, [s]
u	velocity of the flow, [m/s]
v	velocity of the body, [m/s]
V	control volume [m^3]
W	spanwise spacing between the rods, [m]
δ	boundary layer thickness, [m]
δ^*	displacement thickness, [m]
η	acoustic efficiency, %
γ	sweep angle at which the flow passes the trailing edge, [°]
λ	acoustic wavelength, [m]
μ	coefficient of viscosity, [Pa s]
ω	angular velocity of the blade surface, [s^{-1}]
Ω	rotational speed, [RPM]
ϕ	acoustic potential, [s], pitch angle of the rods, [°]
ψ	polar direction of the observer, [°]
ρ	density of air, [kg/m^3]
τ	source/emission time, [s]
θ	local angle between surface normal and radiation vector, skew angle of the rods, [°]
θ^*	momentum thickness, [m]
Λ	size of the eddy, [m]
φ	lateral direction of the observer, [°]
ϑ	angle between the source velocity vector and the observer's position from the source perspective, [°]

Vector

$\underline{e}$	steering vector
$\underline{n}$	outward normal vector
$\underline{r}$	radiation vector, [m]
$\underline{u}$	velocity of the flow, [m/s]

$\underline{v}$ velocity of the body, [m/s]

$\underline{w}$ weight vector

$\underline{x}$ observer location, [m]

$\underline{y}$ source location, [m]

Tensor

$\underline{\underline{P}}$ Fluid stress tensor

$\underline{\underline{T}}$ Lighthill tensor

$\underline{\underline{\tau}}$ Viscous stress tensor

Function

f_c control surface

g collapsing sphere

$G(x,t;y,\tau)$ Green's function

$H(f)$ Heaviside function

$s(\overrightarrow{x}_m, \overrightarrow{x}_s, \omega)$ steering function

δ_f Dirac delta function

δ_{ij} Kronecker delta function

Index

a acoustic, approximate

A amplitude

B source body

c collapsing sphere

d drag

e emission

ext extrapolated

f original

h hydrodynamic

i,j,k three normal components

img image

KIR Kirchoff

l lift

L loading noise

meas measured

n normal

nom	nominal value
0	ambient conditions
p	pressure
r	distance between the source and the observer
rms	root mean square
RVG	Rod Vortex Generator
s	sampling
t	total
T	thickness noise
v	velocity
w	wall
τ	friction

Acronym

APE	Acoustic Perturbation Equations
API	Application Programme Interface
AR	Aspect ratio
AWB	Acoustic Wind tunnel at Braunschweig
BEMT	Blade Element Momentum Theory
BVI	Blade Vortex Interaction noise
CAA	Computational AeroAcoustics
CBF	Conventional Beamforming
CCP	Constant Current Power
CFD	Computational Fluid Dynamics
CSM	Cross-Spectral Matrix
DAMAS	Deconvolution Approach for the Mapping of Acoustic Sources
DFFT	Discrete Fast Fourier Transform
DLR	German Aerospace Centre
DNS	Direct Numerical Simulations
EARSM	Explicit Algebraic Reynolds Stress Model
FLOWer	Structured CFD solver
FW–H	Ffowcs Williams-Hawkings Analogy
GCI	Grid Convergence Index
HR	High Resolution
HSI	High Speed Interaction noise
ID	In-disc-plane observer

IGG	Interactive Grid Generator
jBAY	jirasek Bender Anderson Yagle modeling
LBM	Lattice Boltzmann Methods
LEE	Linearized Euler Equations
LES	Large Eddy Simulations
LF-IPH	Low Frequency-In plane Harmonics
MEMS	Micro-ElectroMechanical system
MSR	Main to Side lobe Ratio
NASA	National Aeronautics and Space Administration
NLEE	decomposed Linearized Euler Equations
NREL	National Renewable Energy Laboratory
NSCBC	Navier-Stokes Characteristic Boundary Condition
OASPL	Overall Sound Pressure Level
OD	Out-of-disc-plane observer
PIV	Particle Image Velocimetry
PSD	Power Spectral Density
PSF	Point-Spread Function
RANS	Reynolds-Averaged Navier–Stokes
RBC	Radiation Boundary Condition
RD	On-axis observer
RHS	Right Hand Side
ROI	Region Of Interest
RPM	Revolutions per minute
RVG	Rod Vortex Generator
SA	Spalart-Allmaras model
SC	Source Coherence
SGS	Sub Grid Scale modelling
SODIX	SOurce Directivity modeling in cross-spectral-matriX
SPL	Sound Pressure Level
TPP	Tip Path Plane
TUD	Delft University of Technology
UMAC	University of Maryland Chamber
URANS	Unsteady Reynolds Averaged Navier-Stokes
VG	Vortex Generator

Chapter 1

Introduction and research objectives

1.1 Background

Sound is a perturbation of pressure that propagates as a wave in a transmission medium (gas/liquid/solid). Noise is sound that is an unwanted irritant depending on the sensitivity of the listener. The typical audible frequency range for humans is 20 Hz – 20 000 Hz corresponding to 0 - 140 dB, while anything over 85 dB is harmful. The maximum sensitivity of the human ear is typically in the range of 2000 Hz – 5000 Hz. The attenuation of the sound waves by the atmosphere increases with frequency, thus, low frequency waves travel long distances. The sound waves carry a large range of power levels from 10^{-10} W while whispering, to a high-end value of 10^5 W for a jet airplane.

In fluids, the rotating vortical motion induces centrifugal forces that are balanced by a local pressure gradient. As the deformation of the vortical motion takes place, the pressure variation induces a density variation due to compressibility, which propagates as sound. Variations of pressure can exist in a purely incompressible medium in vortical motion without becoming acoustic waves. The true acoustic variable is the density fluctuations which is of much smaller magnitude compared to the pressure. Chu and Kovasznay [1] described the three different physical properties of oscillating gas particles:

1. vortical mode – it consists of small rotating perturbations due to viscosity that are incompressible and convected by the mean flow
2. acoustic mode – it consists of potential (rotation free) disturbances that are compressible, isentropic and propagating
3. entropy mode – it consists of small convected motion due to thermal conductivity.

Aeroacoustics deals with the vortical and acoustic modes. The acoustic motion characterised by $|v'_a|$ (where motion is descibed by v, a denotes the acoustic nature and the symbol $'$ denotes fluctuations), is at least an order of magnitude smaller than the vortical motion given by $|v'_h|$ (h denotes the vortical nature), i.e, $|v'_a| << |v'_h|$. The total pressure fluctuations of a source p'_t consists of a summation of "hydrodynamic pressure" and "acoustic pressure". The hydrodynamic pressure p'_h is localized and incompressible, known as pseudo sound (varying as $p'_h \propto r^{-3}$ with r being the distance to the source). The acoustic pressure p' is compressible and radiating, hence known as sound (varying as $p' \propto r^{-1}$). The regions close to the source where the fluctuations are dominated

by the inertial effects due to vorticity i.e $p'_t \approx p'_h >> p'$ [2], are considered as the inner region. At regions far away from the source where the pressure fluctuations are reduced to propagating sound waves $p'_t \approx p'$ (Figure 1.1.1) are considered as the outer regions. These propagating pressure fluctuations to long distances are perceived as unpleasant sounds i.e. noise. Estimation of this far-field noise for rotating bodies (helicopter rotor blades, wind turbine rotor blades, etc.) in subsonic motion, to aid noise mitigation strategies is the focus of this research work.

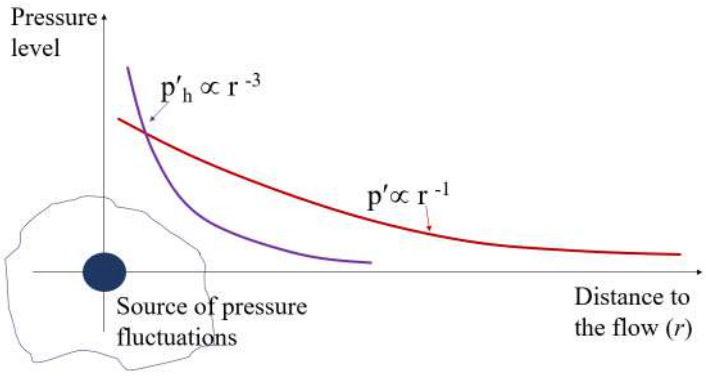

Fig. 1.1.1. Sound and pseudo sound [2].

Noise emission is a major concern for most industries such as automotive, aerospace, wind energy and turbomachines. The sound emitted by these industries cause community annoyance and hindrance to daily life [3, 4]. For instance, irritation due to the sound emitted by wind turbines has led to the general public's reluctance towards their widespread installation [5]. Modern daily life is enhanced by numerous machines and technology, all emitting sound. These emissions become a higher concern for military and medical applications. Thus, a global initiative to reduce noise levels that cause environmental and psychological concerns to human beings [6] has been undertaken. Research into noise generation and propagation that helps innovative noise mitigation strategies is being conducted [7, 8]. Therefore, noise control is now one of the design parameters rather than a post-production fix.

The main classifications of rotating machinery noise are mechanical and aerodynamic noise. Engine noise, transmission and gear box noise are all examples of mechanical noise [9, 10]. Mechanical noise can be mitigated by using mufflers, improved design and operating choices, modern rotor technology and other acoustic treatments which are subjected to design, performance and cost constraints. The aerodynamic noise on the other hand arises from flow physics and its interaction with the rotor body, which are complex to mitigate due to lack of sufficient knowledge on their generation and propagation mechanisms.

A field of study started in the fifties to primarily deal with the sound emitted by the new turbojet planes. This consisted of experimental work on jet noise supplemented by theoretical modelling [11]. During the sixties and seventies, focus on reducing supersonic jet noise due to the development of Concorde, led to the "first golden age of aeroacoustics". The term Computational Aeroacoustics (CAA) was formally summarized by Sir James Lighthill at the ICASE/NASA workshop in 1992. The main conclusions of that workshop were that the sound generating flow process and its near-field propagation were computationally resolved (comprehensive CAA), and the second

approach – hybrid CAA that consists of computationally resolving the sound generating non-linear flow process, while its far-field propagation was estimated by acoustic theory. Thus, began the "second golden age of aeroacoustics" [12] focussing on designing environmentally responsible (reduced noise levels) airplanes. Today, CAA encompasses a broad multi-disciplinary design, analysis and optimization of future airplanes, helicopters, propellers, compressors, wind turbine rotors, unmanned aerial vehicles, turbomachines etc. in dynamic and complex environments, leading to the "third golden age of aeroacoustics" [7]. Detailed description of CAA is provided in Chapter 2.

1.2 Flow control devices

Airfoils/blades when exposed to high-inflow angles develop adverse pressure gradients on their surface. This causes a separation of the flow from the surface leading to decreased aerodynamic performance. Additionally, flow separation also acts as an extra source of noise generation. To tackle separated flows, different types of flow control devices/add-ons have been developed and implemented in many applications. Some of the popular ones are vortex generators (VGs), actuators, roughness elements, trailing edge flaps, leading edge slats etc.

Different types of blade add-ons have been implemented on the wind turbine rotors to serve various purposes. Trailing edge flaps have been studied to control local variations in the aerodynamic forces at high frequencies [13, 14]. Plasma actuators have been investigated for control of flow separation at low Reynolds numbers [15, 16]. Tubercles have been implemented on leading/trailing edges to increase aerodynamic performance [17, 18]. To control boundary layer separation, different VGs [19] – aerodynamically shaped [20], vane type [21–23], air jet type [24, 25], rod type [26, 27] have been implemented.

Many flow control devices have been investigated specifically for helicopter rotors and can be found in literature. Active flow control such as steady/unsteady blowing to reduce parasitic fuselage drag [28,29], plasma flow control [30], gurney flaps [31], active control to reduce fuselage drag [32], etc. have been studied. Passive devices to control flow as well as noise have also been investigated [33–35].

The flow control device of particular interest in this research work is the vortex generator. The basic working principle of a streamwise VG is that it creates streamwise vortices that transfer high momentum fluid from the upper zone of the boundary layer towards the innermost part, closer to the wall/airfoil surface (Figure 1.2.2). This increases the wall shear stresses creating a velocity distribution less prone to separation [36]. Additionaly, the generated streamwise vortices modify the vortical structure close to the wall and enhance turbulence anisotropy in this zone.

VGs were first reported by Taylor in the 1940s [37]. Taylor investigated thin solid plates mounted normal to the surface and they effectively reduced boundary layer separation. However, these thin plates created non-trivial drag which hindered aerodynamic performance. This was because the height of the VGs (h) was of the same order as the boundary layer thickness (δ). Since then, VGs designed with many combinations of the two parameters (h and δ) have been investigated. Various shapes and types, passive ones – triangular VGs, delta shaped VGs, co- and counter rotating vanes, rod type VGs etc. have been studied. Active type like the Air-Jet VGs, that generate streamwise vortices by an inclined jet blown from an orifice/hole, were presented by Wallis and

Stuart [38].

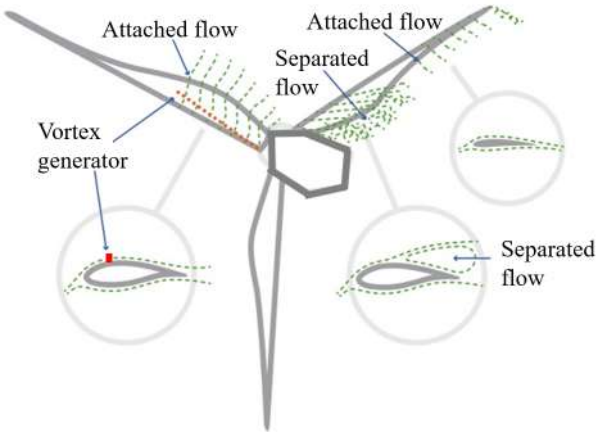

Fig. 1.2.2. Application of vortex generators on a wind turbine.

Lin [39] presented an in-depth review of low-profile vane type VGs ($h/\delta < 0.65$). Parametric studies of vane type VGs have been investigated extensively [40, 41]. Another type of VG called the rod vortex generator (RVG) investigated by Flaszynski et al. [36, 42], is the chosen type of VG for this research work. Streamwise vortices are created by cylindrical rods that are embedded inside the boundary layer (Figure 1.2.3). These rods have an advantage over classical vane types as they can be activated only at the off-design conditions by utilizing MEMS technology [43]. Thus, they can be used both as active and passive flow control.

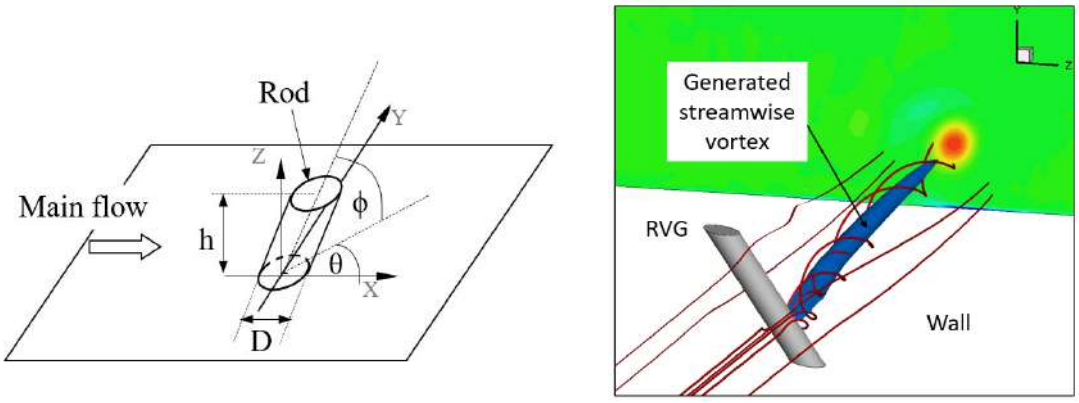

Fig. 1.2.3. A single RVG (left) and streamwise vortex induced by an RVG - mean isosurface of Q-criterion coloured by vorticity magnitude (right).

1.3 Motivation

Research on noise emission from applications such as wind turbines, helicopters, fans etc. at design conditions is available in literature. For the wind turbines at design conditions, trailing edge is the predominant noise source and is extensively studied

[44–46]. However, sound levels generated during the off-design conditions are still relatively unknown. These rotor blades are subjected to turbulence, gusts, high-inflow angles, dirt/impurities on the blade surface causing boundary layer flow separation. This leads to unsteady loading which cannot be mitigated by control systems thus, necessitating flow control devices. The unsteady loading alters the overall sound levels of wind turbines and could impact the annoying noise content perceived by humans. The implemented add-ons (eg. vortex generators) also alter the sound emission and generate additional self-noise.

Reducing the overall noise emission thereby addressing the general public's concerns is a primary goal particularly for the wind industry. The unique "swishing" nature (amplitude modulation) of the wind turbine noise has caused irritation to the public and has increased the community's opposition to wind farm installations. This has forced the turbines to operate at lower speeds and capacities, driving up per unit energy costs. Wind turbines have undergone a dramatic increase in size from approx. 11 m to a massive 252 m diameter rotors generating 22 kW – 13.6 MW power respectively for offshore and up to 126 m rotor generating 7.5 MW power for onshore turbines. Increasing the diameter increases the tip speed thus increasing annual energy production. This is accompanied by a penalty of increased sound levels (Figure 1.3.4). To satisfy community regulations of acceptable noise levels, many wind farms are forced to operate at lower speeds. Even a single decibel reduction in sound levels costs approx. 2 – 4% of the annual energy production [47]. Thus, reducing sound emissions by even 1 dB is non-trivial.

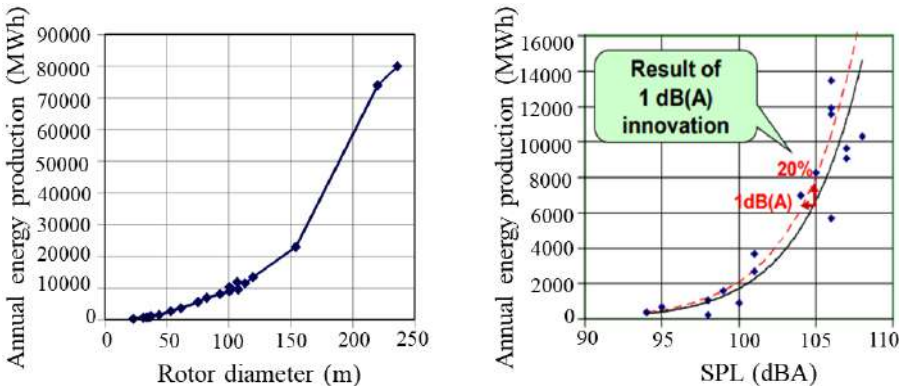

Fig. 1.3.4. Correlation between rotor size and energy production (left) and correlation between sound power level and annual energy production [47].

Given the dual requirements of flow control devices – controlling flow separation without any additional (significant) acoustic penalty, research into noise generation and propagation mechanisms of a particular type of flow control device – RVG, is undertaken. Impact of streamwise vortices (generated by the rods) on the boundary layer separation and the aerodynamic performance of wind turbine rotors have been investigated [26]. However, the detailed acoustic characteristics of this particular type of VG is unknown. Boundary layer flow separation is known to cause additional separation noise. Although vortex generators decrease separation, they also increase the pressure fluctuations due to re-energizing of the boundary layer and thereby alter the surface pressure distribution. This is expected to affect the trailing edge noise at certain

frequencies. Additionally, new surface elements are implemented on the blade possibly impacting the rotational noise. The acoustic impact of the RVGs on wind turbine rotors particularly in the low frequency ranges that propagate long distances (heard by residents living near wind farms) is of main concern.

1.4 Wind turbine noise

Modern wind turbines emit mostly aerodynamic noise since the mechanical noise is reduced through good design [48]. However, the public response and perception of noise levels from wind turbines has been largely negative. This has become a major roadblock for widespread usage of wind energy. In order to adhere to the stringent noise regulations imposed by governments, wind turbines have been forced to run at reduced power thus making noise mitigation the primary objective for the wind industry. There is an inflated annoyance at wind turbines, even though they emit the same noise levels as other daily sources i.e. trains/cars/planes (Figure 1.4.5).

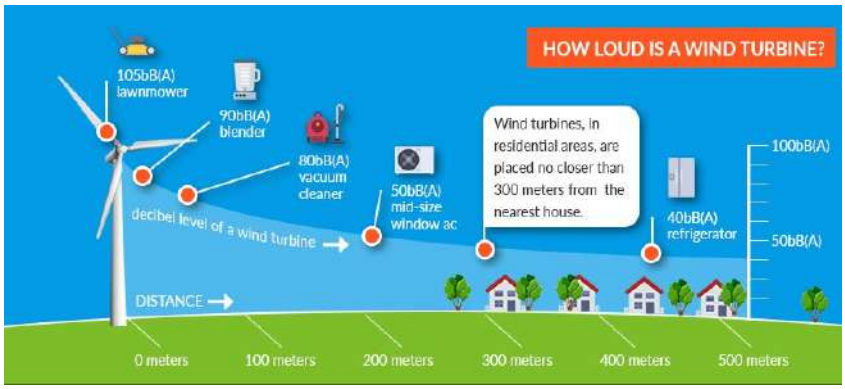

Fig. 1.4.5. Perception of wind turbine noise compared to daily appliances [49].

Wagner et al. [50] presented the various aerodynamic noise generation mechanisms for a wind turbine. They are broadly classified as inflow turbulence noise and airfoil self-noise. Airfoil self-noise is further classified into trailing edge noise, blunt trailing edge noise, boundary layer vortex shedding noise, tip noise, separation/stall noise, noise due to blade surface imperfections (Figure 1.4.6).

The inflow turbulence noise is created when the rotor blade (leading edge) interacts with the oncoming turbulence in the atmosphere [51]. It consists of two regimes of noise depending on the size of the turbulent eddy Λ in relation to the blade chord c, occuring in frequencies up to 1000 Hz. If the size of the eddy is significantly larger than the blade chord i.e. $\Lambda >> c$, the total blade loading changes. This leads to a dipole like emission characterised by the 6^{th} power of Mach number (see section 2.8). This low-frequency inflow turbulence noise is estimated as the net force on the blade, hence it is modelled as a dipole (elementary point source). The rotor blade can be regarded as acoustically compact [50]. If the eddy size is smaller than the blade chord, it affects the pressure fluctuations only locally. This is a much more complicated noise mechanism occuring at high frequencies and the rotor blade is acoustically non compact. Turbulent eddies are distorted by the mean flow and emit sound waves. These waves are then scattered by both the leading and the trailing edges. The intensity of sound waves varies with

the 5^{th} power of Mach number [52]. Some of the parameters that could reduce inflow turbulence noise is the airfoil shape i.e the leading edge [53].

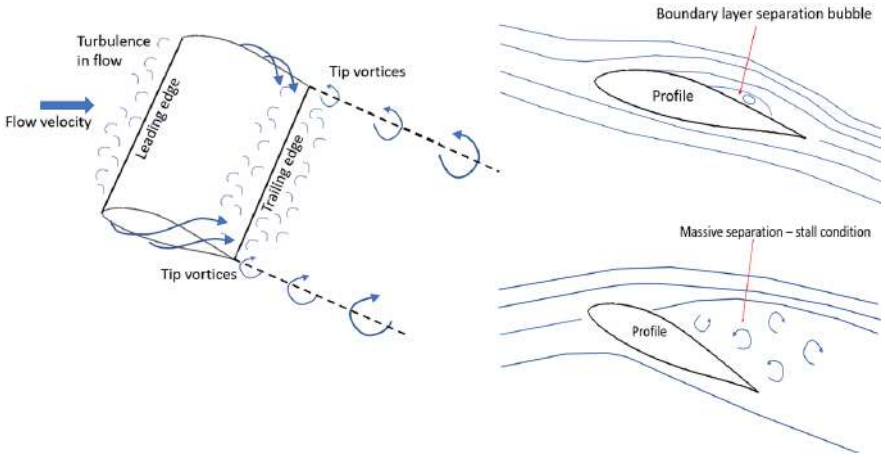

Fig. 1.4.6. Sources of airfoil self-noise.

Airfoil tip noise generates high-frequency broadband noise. The turbulence in the local separated flow region caused due to the formation of the tip vortex creates tip noise. The flow over the blade tip consists of a strong vortex with highly viscous core which is very turbulent. The mechanism for noise production is the trailing edge noise due to the passage of this turbulence over the trailing edge portion of the tip region [54, 55]. This broadband noise depends on the tip vortex strength, convection speed of the vortex, vortex spanwise extent and the shape of the blade tip. Brooks et al. [56] estimate that this noise adds about 1 dB – 2 dB at certain frequencies.

Airfoil tonal noise is generated when vortices originating from the boundary layer or the wake region creates tones. A self-reinforcing feedback loop may or may not strengthen this interaction. This noise is of concern for small wind turbines ($\leq$10 kW) operating at low-to-moderate Reynolds numbers [57, 58].

Blade tower interaction noise is generated when the tower wake interacts with the rotor blades. The eddies created by the tower interacts with the blades similar to the leading edge interaction noise. This can be eliminated by adjusting the relative position of the tower and the rotor blades [59].

Trailing edge noise is the most prominent noise source and is extensively researched [14, 46]. This noise is emitted when the eddies from the turbulent boundary layer pass over to the trailing edge and gets scattered to the far-field. Undisturbed turbulence is a poor radiator of sound [57] but when it encounters a sharp edge (trailing edge), the acoustic waves are augmented by edge diffraction mechanism [60]. The directivity pattern of the trailing edge is a cardioid pattern with sound radiating prominently in the direction of rotation, forward of the wind turbine rotor. This creates a periodic fluctuations of acoustic waves known as “swish”. It is defined as the amplitude modulation of broadband noise generated by rotor blades at the blade passing frequency [44].

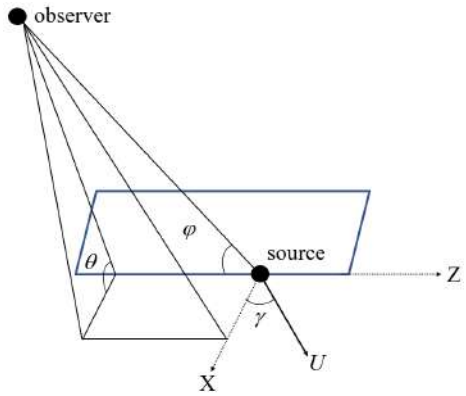

Fig. 1.4.7. Trailing edge noise angle definitions.

The trailing edge noise characteristics is described by Equation 1.4.1. It assumes that the trailing edge is a semi-infinite plate [61].

$$p' \propto \sqrt{v^5 \frac{L\delta}{r^2} \cos^3(\gamma) \sin^2(\psi/2) \sin(\varphi)} \tag{1.4.1}$$

where, p' is the acoustic pressure produced by a 2D blade section, v is the local flow speed, L is the spanwise length of the 2D section, δ is the boundary layer thickness at the trailing edge, r is the distance to the observer, γ is the sweep angle at which the flow passes the trailing edge, ψ is the polar direction of the observer and φ is the lateral direction of the observer (Figure 1.4.7).

The driving parameter for the trailing edge noise is the flow speed v driven by the rotor RPM (5^{th} power). Since the outboard part of the blades have the highest speeds, they are also the major sources of noise [62]. Hence, reducing rotor RPM reduces noise. The directivity of the trailing edge noise is governed by the angle ψ. For instance, for an observer on the ground i.e. $\psi = 0$, the noise is radiated in the direction of the leading edge. This pattern along with the doppler amplification causes the blades moving downwards to emit louder noise than the upward moving blades. This asymmetry causes the annoying "swish" noise.

When the inflow angle increases for instance, due to sudden atmospheric gusts etc., separation of flow on the blade surface occurs. This leads to separation noise [63]. The periodic separation and reattachment of boundary layers on the wind turbine blades causes dynamic stall noise – strong amplitude modulations that can cause public inconvenience at long distances [64]. Flow separation is tackled by implementing various flow control devices discussed in section 1.2. However, the research on the impact of these control devices on noise emitted is rather limited. Kolkman et al. [65] conducted acoustic measurements for vane type vortex generators on an airfoil. The acoustic impact of the rod type VGs is still unknown and forms the core of this research work.

At much higher inflow angles, massive separation occurs leading to stall. This phenemenon leads to stall noise [66]. Stall noise is broadband in nature and can be avoided by avoiding stall conditions [56, 67]. Stall is an extreme condition for rotor blades that leads to failure and thus is not a primary acoustic concern while designing.

1.5 Helicopter rotor noise

Sound emission of helicopters, often operating at low altitudes, causes community annoyance and hindrance to daily life for people living around airports [68]. It is of even higher concern in military applications which led to a push for "quiet helicopters" in the U.S Army during the 1960s [69]. Helicopter rotor noise is discussed in detail since it is used in the verification of the developed aeroacoustic code presented in Chapter 4. This particular application is chosen as numerical and experimental data exists within the research group and in literature respectively, aiding a thorough validation.

Cox et al. [70] presented experimental and analytical investigations for a single rotor turbine HU–1A helicopter, identifying the important sources of noise and their order of prominence for a far-field observer. Henderson et al. [71] showed that the harmonic noise from the main rotor is the primary source in forward flight and that tail rotor noise is predominant in hover mode. Numerous experimental campaigns were conducted to study rotor noise [72–75]. Schmitz introduced a novel measuring technique for helicopters and has provided an in-depth understanding of the various noise mechanisms [76–78]. Theory for predicting rotational noise in forward flight was studied by Loewy et al. [79]. Utilizing the theoretical methods of propellers, led to poor noise comparison of theoretical prediction against experiments in helicopter rotors [80]. Through computational investigations, Loewy and Sutton [79] found the cause of the discrepancy – large fluctuating forces on the helicopter rotor blade similar to findings of Schlegel et al. [81].

The helicopter rotor noise has a variety of sources in a broad range of frequencies, whose importance is decided by the distance to the observer, nature of propagating medium and the acoustic objectives envisioned in each case. The main types are the noise generated by the main rotor at low frequencies, tail rotor harmonics generated at low and mid frequencies, broadband noise sources in the medium frequency range, blade-vortex interaction noise (BVI) and high-speed impulsive noise (HSI) at mid frequencies, engine and the transmission noise at high frequencies [10].

The fluctuating loads on the blade (loading noise) causes the main rotor noise, while the tail rotor noise is characterised by both thickness and loading noise components. The most significant main rotor impulsive noise is characterised by HSI and BVI [69]. For most considerations, low-frequency rotor harmonic noise becomes important since they travel long distances [82] causing annoyance to humans and aiding detection. This gets further exacerbated by helicopters flying at low altitudes and in the rotor tip-path-plane (TPP). The tip-path-plane is the plane connecting the rotor blade tips as they rotate. This plane is horizontal during hover and is rotated slightly in the forward direction during forward flights [83].

Rotor harmonic noise can be broadly classified into fundamental noise types and complex mechanisms. The three fundamental noise types discussed below are emitted generally (in various degrees) by rotating body applications while the specific complex mechanisms discussed below are for the helicopter rotor.

One of the fundamental types of noise is the thickness noise. It is generated by moving bodies that displace the air medium surrounding it thus making it relevant at all operating conditions. To understand it, Schmitz [69] modelled it as a pair of monopoles of equal but opposing strength – source and sink located at the leading and trailing edge respectively. The time delay in the pressure fluctuations reaching the

observer due to their varied distance to the source and sink characterises the shape of the thickness noise. Typically it consists of a large negative pulse (strongest in the rotor plane) followed by smaller positive peaks. This is presented in section 3.6.

The second fundamental noise is the loading noise. It is caused due to steady/varying aerodynamic forces (exerted by the rotor blade) acting on the surrounding medium. Since the loading forces (in-plane and out-of-plane) are subject to the operating conditions, the loading noise becomes significant only at specific conditions. The in-plane loading noise usually emits in the TPP at low frequencies thus causing concern for residents at the far-field.

Broadband noise is the third fundamental type. It is caused due to the random unsteady disturbances in the flow leading to localized pressure variations on the blade (for example: shock waves). This becomes significant when the rotor tip Mach numbers are high subsonic and transonic [84].

High-speed impulsive noise (HSI) is a complex harmonic noise generated by both the main and tail rotors, causing annoyance. It is emitted mostly by the tip region on the advancing side of the rotor. The tip Mach numbers at this region reach higher values causing amplification of the noise mechanisms. This creates a shock wave on the blade surface that extends past the blade into the far-field (delocalization) [76]. However, this noise was present in the older helicopters, but by reducing tip speeds, sweeping the blade tips and through some design changes, HSI noise is largely avoided in modern rotors.

Blade vortex interaction noise (BVI) is also an impulsive type of noise caused by sudden, drastic pressure changes occuring on rotor blades. This happens when rotor blades interact with their own vortices/wakes generated by a preceding blade, i.e rotor wake is aligned with the TPP. This occurs mainly during rotor landing. This noise is characterised by the unique "wop-wop" sound that is at high frequency and high energy content. This high-frequency nature makes it less troublesome for helicopter detection. [77, 85–87].

Low-frequency in-plane harmonic noise (LF-IPH) is a linear summation of thickness and loading noise near the TPP. It is dominated by the thickness noise but there is a non trivial contribution of the in-plane loading noise at low frequencies. This contribution is a function of the phase difference between the two noise mechanisms (thickness and in-plane loading). The low-frequency nature of this noise is of particular concern for helicopter detection since they do not undergo strong atmospheric attenuation.

Tail rotor harmonic noise is a high-frequency noise content that contributes to in-plane harmonic noise radiation. This makes it important while trying to avoid helicopter detection. Detailed research on tail rotor noise is available in literature [88, 89].

All the various types of noise described above can be represented as either individually or as a combination of the three elementary sources – monopole, dipole and quadrupole. These elementary sources have their unique acoustic characteristics that are described in detail in section 2.8.

1.6 Thesis objectives and outline

The current research is undertaken to understand thoroughly the noise generation and propagation mechanisms that would further aid in reducing the sound emissions. Inves-

tigation into the sound emitted by wind turbine rotor blades/airfoil specifically during the off-design operating condition such as the turbulent boundary layer flow separation is the main focus. The central objective is to analyze the acoustic impact of a particular type of flow control device – the rod vortex generators (RVGs) that reduce boundary layer separation.

The hypothesis of this research is that **"the rod vortex generators reduce flow separation thereby reducing separation noise, however, they also act as an additional source of noise thus increasing noise at certain frequencies."**

Primarily, the methodology to estimate the acoustics of rotating bodies (in subsonic motion) is implemented in this research work. The aim is to develop, validate and verify a post-processing acoustic code based on the FW–H analogy, capable of investigating add-ons on rotating bodies in both time and frequency domains. To implement a tool to predict acoustic pressure signals in several details (components of noise, near- and far-field details etc.) for various applications. This code can be used to analyze existing data (post-processing) as well as during the design phase of new rotors and applications. Although analysis of an helicopter rotor and a wind turbine rotor (equipped with RVGs) is presented in this work, the developed code is implemented in such a way to allow for investigation of any rotating body (subsonic motion) equipped with blade add-ons.

Furthermore, to understand and estimate the impact of the rod type of vortex generators on the separation noise, broadband trailing edge noise and rod self-noise levels, an experimental campaign is undertaken. The impact of the rods on the flow separation zone and the boundary layer flow characteristics is investigated using different flow measurement techniques. The effect of implementing RVGs on the overall sound pressure levels of the airfoil is studied through acoustic beamforming techniques. To summarize the main objectives:

1. implement and validate a general aeroacoustic code to predict acoustic pressure in great detail for rotating bodies in subsonic motion
2. investigate the noise emitted by a model helicopter rotor in hover utilizing the developed aeroacoustic code (further verification of the code)
3. investigate the acoustic impact (rotational noise) of RVGs implemented on a wind turbine rotor blade
4. investigate the acoustic impact (separation and trailing edge noise) of RVGs implemented on a wind turbine airfoil.

The numerical approach to enable aeroacoustic analysis is to implement a general acoustic code to predict acoustic pressure signals emitted by rotating bodies in subsonic motion. A flexible tool based on the popular Ffowcs–Williams and Hawkings (FW–H) acoustic analogy is envisioned. A brief introduction to the fundamentals of computational aeroacoustics and various acoustic analogies is presented in Chapter 2. The theory of the elementary acoustic sources utilized for the validation of the developed code is also detailed.

For bodies in subsonic motion the acoustic pressure is a combination of predominantly two types of noise – thickness and loading noise. Their mechanism can be understood using the elementary sources – the monopole and the dipole. A thorough validation of the code against analytical solutions for the elementary sources is presented in Chapter 3. To achieve this, the following cases are validated:

1. stationary source of mass i.e. stationary monopole (section 3.4)

2. stationary source of momentum i.e. stationary dipole (section 3.5)
3. fluctuating and/or rotating source of mass i.e. thickness noise mechanism (section 3.6)
4. rotating source of momentum i.e. loading noise mechanism (section 3.7).

To perform this validation, additional numerical codes are written to discretize the analytical solutions for sources (section 3.2.1). The elementary point source codes are also extended to include distribution of the point sources to mimic noise such as thickness noise (section 3.2.2) and loading noise (section 3.2.3) emitted by practical applications. Apart from serving their original function of validation, these computationally inexpensive codes can also be used for preliminary acoustic analysis and testing various design strategies for rotors to enable reduction of noise levels. To summarize all the codes developed and validated:

1. aeroacoustic code based on the FW–H acoustic analogy
2. numerical codes to obtain analytical solutions for:
    i. stationary, elementary point sources – monopole and dipole
    ii. rotating, elementary point sources – monopole and dipole
    iii. distributed monopoles (thickness noise modelling)
    iv. distributed dipoles (loading noise modelling).

After an extensive validation, the acoustic analysis of a helicopter rotor in hover is conducted. The FW–H prediction is compared against measurements for the model helicopter rotor of Sargent (Chapter 4) with tip Mach number 0.66. The FW–H code predictions are compared thoroughly (component wise, near and far-field contributions, in-plane and out-of-plane contributions) against numerical data from literature (reference acoustic FW–H code) and experimental data from the University of Maryland.

The acoustic analysis of the NREL Phase VI wind turbine rotor blades equipped with RVGs is presented in Chapter 5. The impact of the flow control devices – additional surfaces sticking out of the blades (RVGs), on the thickness and steady loading noise for the wind energy application is analyzed. Steady surface pressure data (RANS) for the NREL wind turbine which is already available within the Aerodynamics department [26] is utilized. Relative acoustic differences (both qualitative and quantitative) between the reference rotor and the rotor equipped with the RVGs are the main focus of this investigation. The directivity of emitted sound is also presented through an analysis of sound at different microphone locations. Apart from a global analysis, local acoustic analysis of specific regions of the rotor blade where the flow control devices are implemented is also presented.

Since only steady rotational noise analysis was presented in the previous chapter due to limited availability of unsteady pressure data, the influence of the RVGs specifically on the broadband trailing edge noise emitted by a wind turbine airfoil is assessed through acoustic measurements in Chapter 6. A study on the impact of Rod Vortex Generators (RVGs) on the flow characteristics and the acoustic far-field pressure (separation and trailing edge noise) of a wind turbine airfoil (DU96-W-180) is conducted through an experimental campaign at Delft University of Technology (TUD). The wall pressure distribution on the airfoil is estimated through static pressure tap measurements on the suction side. The impact of the RVGs on the flow structures and the separation zone reduction is characterised by oil flow visualization. Additionally, the

effect of streamwise vortices (generated by the rods) on the boundary layer characteristics is assessed through Particle Image Velocimetry (PIV) measurements. These findings are presented in Chapter 6. Acoustic analysis is accomplished through the data measured utilizing a microphone array and post-processed using acoustic beamforming code (available within TUD). Additionally, the self-noise generated by the rods is also quantified. To provide an overall acoustic perspective of the RVGs, sound spectral analysis for a range of frequencies for the wind turbine airfoil with/without RVGs is conducted.

Important observations and analysis obtained from the analysis of the impact of flow control devices on the trailing edge noise emitted by an airfoil and the steady rotational noise emitted by a wind turbine are all encapsulated in Chapter 7. A concise summary of all the activities performed in this research work are provided in this last Conclusions chapter.

Some of the RANS simulations for designing the airfoil model utilized in the experimental campaign at TUD were conducted by Michal Piotrowicz (IMP-PAN). Support during manufacturing of the model and PIV set-up was provided by Marcin Kurowski (IMP-PAN). The measurement campaign at TUD was conducted under the guidance of Daniele Ragni and his team. Oil flow visualization was conducted with the help of Christopher Teruna (TUD). Support during the PIV set-up and initial settings of the post-processing system was provided by Daniele Ragni (TUD). Setting up the microphone array for measurements was conducted with the help of Alejandro Rubio Carpio (TUD). The beamforming code utilized for post-processing the measured acoustic data is obtained from Salil Luesutthiviboon (TUD). Although the setting up of various measurement techniques was conducted with the support of others, the collection of data, the post-processing and analysis of all the results presented in this work are performed by the author.

Chapter 2

Key aspects of aeroacoustics

2.1 Introduction

Computational aeroacoustics (CAA) aims to provide solutions to acoustic problems that are generated by aerodynamic flows in various power and transport industries that run the modern world using computational mathematics. Aeroacoustics deals with the prediction of pressure fields induced as a by-product of inhomogeneous flows, secondary effects of turbulence and the back reaction of these fields on the turbulence [90]. The central idea is to provide feasible tools to understand the physics and propagation of sound emission. The rapid progress in the computing capabilities achieved by the latest computers has eased the high computational costs of CAA techniques, thus making it more accessible and widely used [7, 91]. The reason for the high costs of CAA techniques compared to CFD simulations is firstly, a large computational domain is needed to account for both, the region surrounding the body where the sound sources are generated (source region) and the region where the sound propagates and is heard by observers (far-field). There exists also a non trivial difference in the length scale of the source region and the region of propagation. The sound intensity levels are of six orders lower in magnitude compared to the mean flow characteristics, thus, imposing strict limits on numerical errors (dissipation and dispersion) for aeroacoustics [92].

CAA techniques can be broadly classified as Direct methods and Integral methods (Hybrid). Direct method consists of solving the compressible flow governing equations and acoustic fluctuations simultaneously. The flow equations describing the mean flow and the acoustic source region is resolved using high fidelity CFD methods such as large eddy simulation (LES), zonal LES, detached eddy simulations (DES), hybrid RANS–LES and DNS [93]. These exhaustive simulations should include the domain at the far-field thus making them computationally very expensive. This makes Direct methods impractical for industrial analysis, thereby restricting them to near-field sound predictions. Hybrid methods on the other hand, decouples the sound generation and sound propagation mechanisms [12]. This allows for high fidelity methods in the source near-field region and then integral methods for long distances of sound propagation using acoustic analogies (Figure 2.1.1).

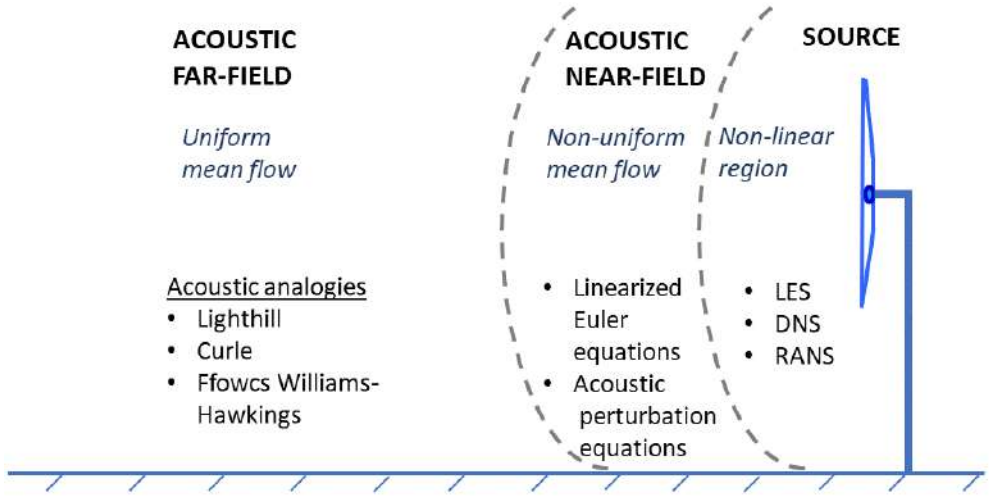

Fig. 2.1.1. Overview of CAA methods.

The main principle of the Hybrid approach is based on separating the source physics (sound generation) and source motion (sound propagation). The data from the source region is then coupled with the propagation equations to obtain far-field acoustics. This can be achieved by two ways - equivalent acoustic sources or the acoustic boundary conditions. The equivalent sources method consists of computing the source region to obtain equivalent aeroacoustic sources that act as source terms on the right hand side of the propagation equations, for instance, all the acoustic analogies. The acoustic boundary method involves computing the source region to obtain acoustic pressure/velocities on a fictitious surface surrounding the source region. The obtained acoustic variables then act as boundary conditions for the propagation equations thus eliminating the need for additional source terms, for example, the Linearized Euler Equations (LEE)/Acoustic Perturbation Equations (APE-SGS method) [94–96].

The key governing feature of CAA is to limit the numerical errors that degrade the propagation of sound waves to the far-field. Dissipation of the acoustic energy leads to peak amplitude reduction and the phase difference between the various acoustic pressures reaching the observer, is extremely sensitive to dispersion. Artificial dispersion of waves could lead to improper wave interference altering sound levels [7]. This has necessitated high-order numerical schemes for complex topologies [97]. For example, two-step Taylor-Galerkin finite element schemes [98, 99], discontinuous Galerkin method [100, 101] and hybrid DG-finite difference methods [102], lattice Boltzmann method (LBM) [103,104] etc. Another key feature of CAA is to implement appropriate boundary conditions to avoid reflections [105]. Research into different types of boundary conditions such as Navier-Stokes characteristic boundary condition (NSCBC) [106,107], radiation boundary condition (RBC) [108] have been conducted.

The acoustic propagation domain is generally classified into acoustic near-field and far-field. The region where there is a linear interaction between the flow physics and the acoustic field is considered as the acoustic near-field. In this region, convection, refraction and diffraction of sound waves is undertaken by the flow [94]. To handle the non-uniform mean flow [109], Linearized Euler equations (LEE) [110], decomposed LEE (NLEE) [111], the acoustic perturbation equations (APE) [112] or the perturbed compressible equations [113] can be applied in this region. The main disadvantage of

LEE/NLEE is that they take into account the propagation of acoustic, vorticity and entropy waves [94]. This could result in unphysical or unstable solutions. To tackle this, the LEE are filtered in a Laplace/Fourier space to only allow for the propagation of acoustic waves [112].

Acoustic far-field is the region where the flow field can be considered as uniform or the medium is at rest [94]. In this region, the diffraction effects of the flow on the pressure waves are neglected. Hence, linear acoustic wave equation or the convective wave equation can be ultilized in this region leading to the popular acoustic analogies. The accuracy of the prediction depends upon the accuracy of the CFD simulations ultilized to characterize the source region. No additional numerical errors are introduced in the far-field propagation. However, the limitation of this approach is that the observer has to be at a certain distance from the source (far-field approximations).

The theoretical foundation to aeroacoustics was laid down by Stokes, Helmholtz, Kirchoff and Rayleigh [114]. The fundamental ideas are summarized by Lord Rayleigh in "Theory of Sound" [115]. A moving medium (air/fluid) characterised by small amplitude fluctuations, contains three types of motion - acoustic wave motion, motion due to vorticity diffusion and motion due to thermal diffusion (described in Chapter 1). The resulting movement is a linear superposition of the above three types and that a linear coupling between them occurs at the boundaries of the fluid region (provided small amplitudes and uniform ambient conditions). Rayleigh also studied the large amplitude fluctuations where he proposed that one type of motion i.e. motion due to vorticity is generated by self/mutual second-order interactions of a first-order acoustic field. This idea is similar to Lighthill's theory of jet noise i.e. jet noise is generated due to the second-order interactions of turbulence (first-order vorticity) with itself [1]. Lighthill formulated his brilliant idea of an exact acoustic analogy for sound due to turbulence in his famous "On sound generated aerodynamically: 1. General theory" in 1952 [11]. Although, before him, Gutin developed the earliest theoretical model of rotor noise by recognizing steady aerodynamic forces on a propeller to be dipole sources [80]. Gutin assumed that the net forces were acting as acoustic dipoles at a distinct point along the blade, neglecting the retarded time effect and the distribution of forces along the blade. This idea was extended to uniformly moving propeller by Garrick et al. [116]. The effect of blade thickness on acoustics was studied by Deming [117] but, he too, assumed the compact source conditions neglecting the retarded time effects. Lighthill's exact formulation of the acoustic analogy streamlined fundamental acoustic research. Chu and Kovasznay presented Lighthill's stress tensor as an acoustic source generated by self interaction of the vortical mode [1]. They propounded the importance of non-linearities in the generation of fluctuations. In 1972, Doak [114] formulated a theory for a generic non-linear fluctuating motion.

2.2 Lighthill's analogy

Lighthill derived from exact equations of motion (mass, momentum and energy conservation equation), a non-homogeneous wave equation with aerodynamic sound sources. The observer characterised in space-time by (x, t) is in a uniform stagnant medium characterised by speed of sound c_0. A slight variation in the ambient flow conditions $(c_0/\rho_0/p_0)$ itself acts as a source of sound [11, 60]. The sound heard by the observer

can be defined by the wave equation 2.2.1:

$$\frac{\partial^2 \rho'}{\partial t^2} - c_0^2 \bigtriangledown^2 \rho' = 0. \tag{2.2.1}$$

The mass and momentum conservation equations are given by Equations 2.2.2 and 2.2.3 respectively:

$$\frac{\partial \rho}{\partial t} + \frac{\partial}{\partial x_i}(\rho v_i) = m, \tag{2.2.2}$$

$$\frac{\partial}{\partial t}(\rho v_i) + \frac{\partial}{\partial x_j}(\rho v_i v_j + P_{ij}) = F_i. \tag{2.2.3}$$

Without mass injection and external forces, rewriting the above equations as equations of the propagation of sound in a uniform medium at rest due to externally applied fluctuating stresses [11]:

$$\frac{\partial \rho}{\partial t} + \frac{\partial}{\partial x_i}(\rho v_i) = 0, \tag{2.2.4}$$

$$\frac{\partial}{\partial t}(\rho v_i) + \frac{\partial}{\partial x_j}(\rho v_i v_j + P_{ij}) = \frac{\partial \tau_{ij}}{\partial x_j}. \tag{2.2.5}$$

Taking time derivative of the mass conservation equation and divergence of momentum conservation, adding and subtracting $c_0^2(\frac{\partial^2 \rho'}{\partial x_i^2})$, leads to Lighthill's equation (2.2.6):

$$\frac{\partial^2 \rho'}{\partial t^2} - c_0^2 \frac{\partial^2 \rho'}{\partial x_i^2} = \frac{\partial^2 T_{ij}}{\partial x_i \partial x_j} \tag{2.2.6}$$

where T_{ij} is the Lighthill stress tensor. The perturbations are given by isentropic conditions as $p' = p - p_0$ and $\rho' = \rho - \rho_0$. With μ as the coefficient of viscosity, the viscous stress tensor is defined as:

$$\tau_{ij} = \mu\left(-\frac{\partial v_i}{\partial x_j} - \frac{\partial v_j}{\partial x_j} + \frac{2}{3}\left[\frac{\partial v_k}{\partial x_k}\right]\delta_{ij}\right). \tag{2.2.7}$$

Utilizing the definitions of the viscous stress tensor τ_{ij} and Kronecker delta δ_{ij}, the Lighthill stress tensor is expressed as:

$$T_{ij} = \rho v_i v_j - \tau_{ij} + (p' - c_0^2 \rho')\delta_{ij}. \tag{2.2.8}$$

The sources of sound obtained from the Lighthill stress tensor are :

1. Reynolds stress tensor $\rho v_i v_j$ (describes the non-linear convective forces)
2. viscous forces defined by τ_{ij}
3. deviations from isentropic condition $p' - c_0^2 \rho'$ i.e. variations from uniform reference state such as ambient sound velocity (c_0)/ambient pressure (p_0)/ambient density (ρ_0).

It is important to note that the Lighthill's analogy assumes a known uniform flow field and that a feedback loop between the flow field and the acoustic field is not explicitly addressed. It is also not suitable for high Mach number applications when the body is no longer compact.

2.3 Kirchhoff's equation

The estimation of the source terms due to flow non-linearities (volumetric/quadrupole) cannot be neglected for high-speed applications (eg. HSI noise in helicopters). Kirchhoff developed an alternative idea to resolve volumetric source terms and obtain their propagation in the far-field. He introduced a fictitious control surface known as the Kirchhoff's surface that encompasses the source region including non-linearities [118, 119]. The volume integrals are converted into surface integrals on the Kirchhoff's surface. CFD simulations can be conducted inside of the control surface to get the necessary input for acoustics (Figure 2.3.2). This idea is analogous to the porous/penetrable surface FW–H formulation originally proposed by Ffowcs-Williams and Hawkings and formally applied by di Francescantonio for helicopter rotor noise prediction [120]. Brentner and Farassat present a thorough comparison (analytical and numerical) of the two approaches [121] which points out the superiority of FW-H formulation due to it's conservation laws foundation unlike the wave equation basis of Kirchhoff's theorem. Kirchhoff's formulation requires the fictitious surface to be placed in a flow linear region (cumbersome) while the FW-H permeable surface has no such restrictions [122].

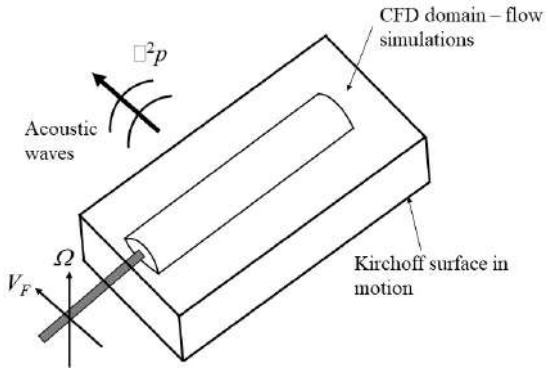

Fig. 2.3.2. Kirchhoff surface definition.

The acoustic pressure $p(x,t)$ at the far-field is defined based on the surface $f_c = 0$ which encloses all the acoustic sources inside such that:

$$\tilde{p} = \begin{cases} p & f_c > 0 \\ 0 & f_c < 0 \end{cases} \tag{2.3.1}$$

where, p is a solution of the wave equation on $f_c = 0$. The Kirchhoff formulation is given by the Equation [123]:

$$\begin{aligned} \Box^2 p(x,t) = &- \left(\frac{\partial p}{\partial t} \frac{v_n}{c_0^2} + \frac{\partial p}{\partial n} \right) \delta(f_c) - \frac{\partial}{\partial t} \left[p \frac{v_n}{c_0^2} \delta(f_c) \right] - \frac{\partial}{\partial x_i} \left[p \hat{n_i} \delta(f_c) \right] \equiv \\ &\equiv Q_{KIR}. \end{aligned} \tag{2.3.2}$$

This formulation is valid only in the regions where wave equation is the correct governing equation [118, 119]. The additional source terms not included here are of second order and can be neglected in the linear flow region thus limiting its location.

2.4 Curle's analogy

Curle proposed an extension to the Lighthill's theory in order to take into account the presence of solid boundaries. Thus, two key factors were incorporated [124]:

1. reflection and diffraction of the sound waves at the solid walls
2. a resultant dipole field at the solid boundaries which are the limits of the quadrupole distribution.

This resulted in a distribution of dipoles representing the force/unit area with which the solid surface acts on the fluid. Curle's method involves predicting sound using free-field Green's function G_0 to solve Lighthill's equation. Consider a body enclosed by the control surface f_c. The control volume V is defined at the fluid side of f_c with the outer normal n acting towards the body enclosed by f_c (Figure 2.4.3).

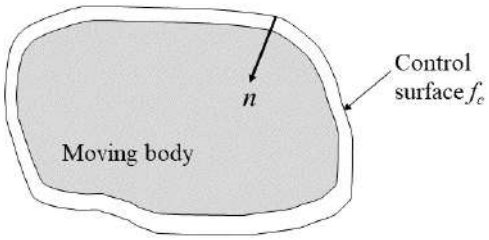

Fig. 2.4.3. Curle body definition.

From Lighthill's Equation 2.2.6 and utilizing the unique properties of the Green's function, an integral equation for pressure is taken as the starting point (Equation 2.4.1). Implementing the principles of reciprocity the source characteristics (y, τ) are replaced by the observer data (x, t) [125].

$$\begin{aligned}\rho' = &\int_{-\infty}^{t}\iiint_V \frac{\partial^2 T_{ij}}{\partial y_i \partial y_j} G_0(x,t|y,\tau)dyd\tau - \\ &- c_0^2 \int_{-\infty}^{t}\iint_{f_c}\left[\rho' \frac{\partial G_0}{\partial y_i} - G_0 \frac{\partial \rho'}{\partial y_i}\right] n_i d\sigma d\tau.\end{aligned} \tag{2.4.1}$$

Using partial integration and symmetry property $T_{ij} = T_{ji}$ leads to Equation 2.4.2:

$$\begin{aligned}\rho' = &\int_{-\infty}^{t}\iiint_V T_{ij}\frac{\partial^2 G_0}{\partial y_i \partial y_j} dyd\tau + \int_{-\infty}^{t}\iint_{f_c} G_0\left(\frac{\partial P_{ij} + \rho v_i v_j}{\partial y_j}\right) n_i d\sigma d\tau - \\ &- \int_{-\infty}^{t}\iint_{f_c}\left(P_{ij} + \rho v_i v_j\right)\frac{\partial G_0}{\partial y_j} n_i d\sigma d\tau.\end{aligned} \tag{2.4.2}$$

From momentum conservation (Equation 2.2.3) with no external forces ($F_i = 0$) and symmetry principle, moving the time derivative using partial integration we obtain Curle's equation:

$$\begin{aligned}\rho' \simeq &\frac{x_i x_j}{4\pi|x|^2 c_0^4}\frac{\partial^2}{\partial t^2}\iiint_V \left[\frac{T_{ij}}{r}\right]_{t=t_e} dy - \frac{1}{4\pi c_0^2}\frac{\partial}{\partial t}\iint_{f_c}\left[\frac{\rho v_i n_i}{r}\right]_{t=t_e} d\sigma - \\ &- \frac{x_j}{4\pi|x|c_0^3}\frac{\partial}{\partial t}\iint_{f_c}\left[\left(P_{ij} + \rho v_i v_j\right)\frac{n_i}{r}\right]_{t=t_e} d\sigma.\end{aligned} \tag{2.4.3}$$

where, $r = |x - y|$ and the retarded time is given by Equation 2.4.4. The retarded time concept is explained in detail in section 2.6. It is important to note that the the control volume excludes the moving body (Figure 2.4.3). In Equation 2.4.3, the first term on the right hand side denotes the turbulence noise, the second term takes into account the movement of the body (i.e.. the fluid displaced by the body; not mass injection), the third term is the momentum flux through the control surface (pressure and viscous forces).

$$t_e = t - \frac{r}{c_0} \simeq t - \frac{|x|}{c_0}. \tag{2.4.4}$$

For a fixed, rigid and compact body, the emission time does not vary significantly along the body, thus, $r \simeq |x|$. Hence, the instantaneous force of the fluid on the body (lift and drag) is given by Equation 2.4.5:

$$F_i(t_e) \simeq \iint_{f_c} [P_{ij}]_{t=t_e} n_j d\sigma. \tag{2.4.5}$$

For such a compact body, utilizing Equation 2.4.5, the Curle's theorem (Equation 2.4.3) gets reduced to an exact equation:

$$\begin{aligned} \rho'(x,t) = \frac{x_i x_j}{4\pi|x|^3 c_0^4} \frac{\partial^2}{\partial t^2} \iiint_V T_{ij}\left(y, t - \frac{|x|}{c_0}\right) dy - \\ - \frac{x_j}{4\pi|x|^2 c_0^3} \frac{\partial}{\partial t} F_j\left(t - \frac{|x|}{c_0}\right). \end{aligned} \tag{2.4.6}$$

2.5 Ffowcs Williams - Hawkings analogy

Ffowcs Williams and Hawkings reformulated Lighthill's acoustic analogy to include the effects of moving solid bodies [123]. Using generalized functions they rearranged the classical Navier-Stokes equations into an inhomogeneous wave equation consisting of quadrupoles, dipoles and monopoles (see section 2.8). This is derived using a novel idea of embedding the exterior flow problem in an unbounded space to utilize generalized Green's functions to solve the original external flow problem [126]. An unbounded fluid is divided into regions using a mathematical surface that exactly coincides with the physical body. The motion of the fluid both outside and on the control surface mimics the real fluid while the inside of the control surface is defined to be a simple and arbitrary motion. This creates a difference in the properties of the fluid between the inside and the outside of the control surface leading to discontinuities at the boundary (control surface). Mass and momentum sources characterised by generalized functions are introduced to handle these discontinuities, thus, acting as acoustic sources [123]. The unbounded fluid is governed by homogeneous, conservation equations with sources. Two key original ideas were developed to achieve this [84]:

1. Green's function can be used to obtain discontinuous solutions of diffential equations on the condition that the problem is defined in the generalized function space [122, 127, 128]
2. classical conservation equations of mass and momentum are valid for flows with real/artificial discontinuities if the derivatives are written as generalized derivatives [129, 130].

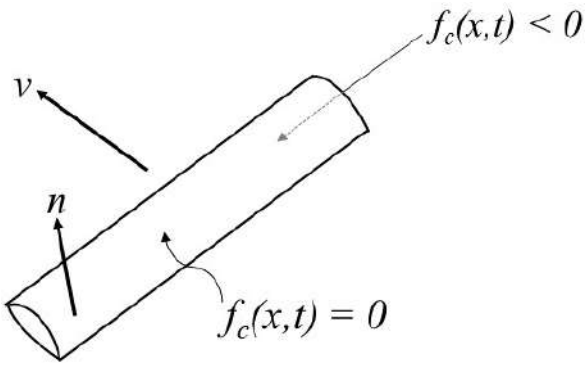

Fig. 2.5.4. FW–H body definition.

Let $f_c(x,t) = 0$ be a moving surface enclosing the sound source region (rotor blades) defined such as $\bigtriangledown f_c = \hat{n}$ with $\hat{n}$ as the outward unit normal vector (Figure 2.5.4). Using the above mentioned two original ideas, all the flow parameters are generalized functions with discontinuities only at the source surface. To emphasize, this implies that the fluid extends into the surface having the characteristics of the undisturbed medium allowing for the wave equation to be valid in the entire 3D space.

The conservation of mass is given by Equation 2.2.2 and the conservation of momentum by Equation 2.2.3 with the source terms equal to zero. Taking into account the artifical discontinuities that were introduced at the source surface $f_c = 0$, Equation 2.2.2 then becomes:

$$\begin{aligned}\frac{\bar{\partial}\rho}{\partial t} + \frac{\bar{\partial}}{\partial x_i}(\rho u_i) &= \frac{\partial \rho}{\partial t} + (\rho - \rho_0)\frac{\partial f_c}{\partial t}\delta(f_c) + \frac{\partial}{\partial x_i}(\rho u_i) + (\rho u_i)\frac{\partial f_c}{\partial x_i}\delta(f_c) = \\ &= \Big[\rho_0 v_n + \rho(u_n - v_n)\Big]\delta(f_c)\end{aligned} \tag{2.5.1}$$

where, $u_n = u_i n_i$ is the local velocity of the fluid in the normal direction to the surface, $n_i = \partial f_c / \partial x_i$ is the component of the unit outward normal to the surface and $v_n = -\partial f_c / \partial t$ is the local normal velocity of the data surface itself. The bar symbol on the variables denotes generalized functions. The artifical discontinuities ($\rho - \rho_0$ and ρu_i) at the surface boundary ($f_c = 0$), introduce a source term on the right side of the mass conservation that is proportional to the local rate of mass injection into the outer domain. Similarly, source terms are added to the momentum equation given by Equation 2.5.2:

$$\begin{aligned}\frac{\bar{\partial}}{\partial t}(\rho u_i) + \frac{\bar{\partial}}{\partial x_j}(\rho u_i u_j + P_{ij}) &= \frac{\partial}{\partial t}(\rho u_i) + \rho u_i \frac{\partial f_c}{\partial t}\delta(f_c) + \\ &+ \frac{\partial}{\partial x_j}(\rho u_i u_j + P_{ij}) + (\rho u_i u_j + \triangle P_{ij})\frac{\partial f_c}{\partial x_j}\delta(f_c) = \\ &= [\rho u_i (u_n - v_n) + \triangle P_{ij} n_j]\,\delta(f_c).\end{aligned} \tag{2.5.2}$$

The introduced source term is proportional to the sum of the local force intensity $\triangle P_{ij} n_j$ on $f_c = 0$ and the rate of momentum injection $\rho u_i (u_n - v_n)$. Taking time derivative on Equation 2.5.1 and space derivative on Equation 2.5.2, subtracting them with each other and rearranging to have the wave operator $c_0^2(\rho - \rho_0)$, results in the

porous/permeable FW–H formulation given by Equation 2.5.3:

$$\begin{aligned}\bar{\Box}^2 p(x,t) = &\frac{\partial}{\partial t}\{[\rho_0 v_n + \rho\,(u_n - v_n)]\delta(f_c)\} - \\ &- \frac{\partial}{\partial x_i}\{[\triangle P_{ij}\hat{n_j} + \rho u_i\,(u_n - v_n)]\delta(f_c)\} + \\ &+ \frac{\bar{\partial}^2}{\partial x_i \partial x_j}\,[T_{ij}H(f_c)]\end{aligned} \tag{2.5.3}$$

with, $\bar{\Box}^2 = [(1/c_0^2)(\bar{\partial}^2/\partial t^2)] - \bar{\bigtriangledown}^2$, $p = c_0^2(\rho - \rho_0)$ and $T_{ij} = \rho u_i u_j + P_{ij} - c_0^2\rho'$ as the Lighthill stress tensor. The Heaviside function ($H(f_c)$) denotes the volumetric term that is exterior to the moving body surface ($f_c = 0$) with $T_{ij} = 0$ inside the surface. $\triangle P_{ij} = (p - p_0)\delta_{ij}$ where δ_{ij} is the Kronecker delta and the viscous terms are neglected.

If the moving body surface $f_c = 0$ is defined to coincide with the solid rotor body, then the normal velocity of the fluid is equal to the normal velocity of the surface i.e. $u_n = v_n$, thus Equation 2.5.3 can be rewritten as the solid FW–H Equation:

$$\bar{\Box}^2 p(x,t) = \frac{\partial}{\partial t}\{[\rho_0 v_n]\delta(f_c)\} - \frac{\partial}{\partial x_i}\{[\triangle P_{ij}\hat{n_j}]\delta(f_c)\} + \frac{\bar{\partial}^2}{\partial x_i \partial x_j}\,[T_{ij}H(f_c)]\,. \tag{2.5.4}$$

The first term on the right hand side is the thickness noise (monopole) generated due to the displacement of the fluid by the moving solid rotor body. The second term is the loading noise (dipole) generated due to varying pressure forces on the body. Both these sources are surface sources defined on $f_c = 0$. The last term is a volumetric source term consisting of flow non-linearities (local speed variation and finite fluid velocity near the body) defined exterior to the body ($H(f_c)$). This term is significant for separated flows, flows with discontinuities, transonic and supersonic applications. Flow discontinuities such as shock waves, thin wakes, vortices can be included in the acoustic prediction by carefully defining the generalized space derivatives of T_{ij} to have the surface sources defined on the discontinuity region. It is important to note that the form of the source terms in the above equation is not unique [90]. Further details about the elementary sources are provided in section 2.8.

2.6 Farassat Formulations

Ffowcs Williams-Hawkings derived an exact, generalized form of the Lighthill's equation for a body in arbitrary motion. Farassat presented solutions to this exact equation known as the Farassat Formulations 1 and 1A for bodies in subsonic motion [131, 132] and Formulation Q1 for bodies in transonic and supersonic motion [133]. To reduce the complexity in solving this equation some important approximations are made by Farassat [131]:

1. the moving body does not disturb the medium strongly, hence the non-linearities are neglected
2. the rotor applications that are investigated (acoustically) such as propellers, rotor blades, fan blades, wind turbines can all be considered as "slender bodies". This implies that the turbulent flow region around the moving bodies is small and since turbulence is also known to be an ineffective noise generating mechanism, the Lighthill stress tensor and the viscosity effects are neglected [60]

3. the moving bodies do not deform and hence, are considered as rigid bodies
4. the compact body assumption and the subsequent far-field approximation imposed on the observer, made in FW-H theory for moving bodies are dependent on observer time and position. These conditions are difficult to quantify/satisfy (for each panel at every position and time-step) for rotating bodies at medium tip speeds with observers in the plane of rotation. Such restrictions are not imposed while deriving the Formulations.

There are several solutions to the FW-H equation, Farassat has presented an excellent summary and description of the various compact and non-compact solutions that have been derived by various authors and also noted each of their limitations in [134]. Starting from the FW-H equation, the volumetric term T_{ij} is neglected due to the above approximation 1. This reduces the wave equation to the addition of the two source terms – one from the normal velocity of the surface of the body (first term on the right side of Equation 2.6.1) and the other from the net local force of the body on the fluid (second term on the right side of Equation 2.6.1). The observer space derivative is converted to observer time derivative analytically.

$$\Box^2 p = \frac{\partial}{\partial \tau}\Big[\rho_0 v_n \mid \nabla f_c \mid \delta\left(f_c\right)\Big] - \frac{\partial}{\partial y_i}\Big[p n_i \mid \nabla f_c \mid \delta\left(f_c\right)\Big]. \tag{2.6.1}$$

To solve the above equation, generalized Green's function for the wave equation in an unbounded three dimensional space is defined as follows [129]:

$$G(x,t;y,\tau) = \begin{cases} 0 & \tau > t \\ \delta(\tau - t + r/c_0)/4\pi r & \tau \leqslant t \end{cases} \tag{2.6.2}$$

where, $r = |x - y|$ and the variables (x,t), (y,τ) and δ represent the observer space - time, source space - time and Dirac delta function respectively. With the fixed observer position, the surface is described by the Equation 2.6.3:

$$g = \tau - t + \frac{r}{c_0} = 0 \qquad\qquad -\infty < \tau \leqslant t \tag{2.6.3}$$

This surface is a collapsing sphere with center at x and radius $= c_0(t - \tau)$. As the source time increases from $-\infty < \tau \leqslant t$, the sphere size shrinks from infinity to zero. The decreasing sphere radius is controlled by the speed of sound. A fictitious radiating surface $\sum$ described by Γ curves is generated by the intersection of the collapsing sphere and the moving body as presented in Figure 2.6.5. This surface is defined by the locus of the points on the moving body surface whose pressure signals reach the observer at the same time t [131].

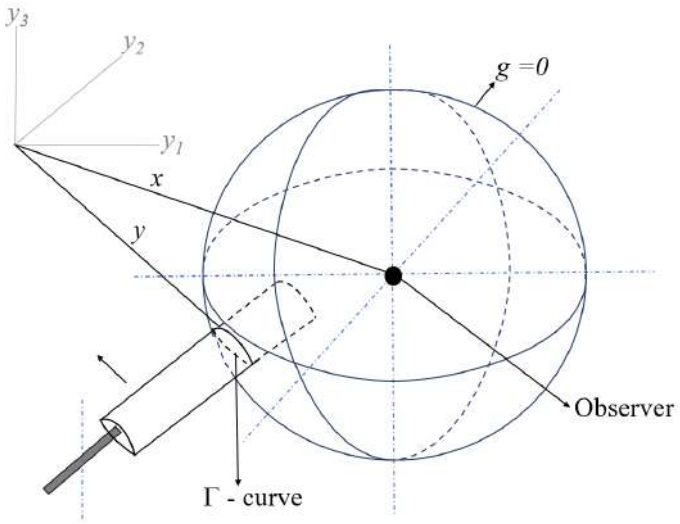

Fig. 2.6.5. Formation of Γ curve by the intersection of the collapsing sphere and a moving body [131].

The sphere (having maximum radius) with centre at observer position x and at source time τ_1, starts to shrink at the speed of sound. The sphere shrinks until it leaves the moving body at time τ_2. The intersection of the sphere and the moving body is bounded in the time region $\tau_1 - \tau_2$. The time history of the moving body contains this information [131].

For applications such as rotor blades with complicated geometrical shapes, the acoustic pressure integration for the $\sum$ surface is difficult. To simplify this, a change in the variables of integration is introduced [126]. The moving body is defined in the η – frame that is fixed relative to the surface. η is the Lagragian variable of a point on the moving body. The trajectory of a point on the body (fixed η – frame) is defined in the y – frame given by Equation 2.6.4:

$$y = \eta + \int_0^\tau v(\eta, \tau) d\tau = y(\eta, \tau) \tag{2.6.4}$$

where, the velocity of a point on the moving body is given by $v(\eta, \tau)$. The two coordinate systems coincide at $\tau = 0$. Using the Jacobian transformation $\tau \rightarrow g$, the emission time is defined by Equation 2.6.5:

$$g = \tau - t + \frac{|x - y(\eta, \tau)|}{c_0} = 0. \tag{2.6.5}$$

The $g = 0$ implies that the source time is dependent on the observer position and time (x, t) in the y – frame. This transcendental equation is solved numerically through iteration. This is known as the retarded time formulation. To obtain this at an observer time t, a fixed point source on the moving body surface is followed in small source time steps ($\tau < t$) to satisfy Equation 2.6.5 as seen in Figure 2.6.6. The emission time also known as the source time is defined by τ, the emission position is $y = y(\eta, \tau)$ and r is the emission distance between the observer position x and the source position η. All these variables are defined in the y – frame fixed to the stationary medium. Solving the Equation 2.6.5, the source time can be obtained. This predicts that for sources in

subsonic motion there is a single emission time and for bodies in supersonic motion the equation predicts two emission times [126].

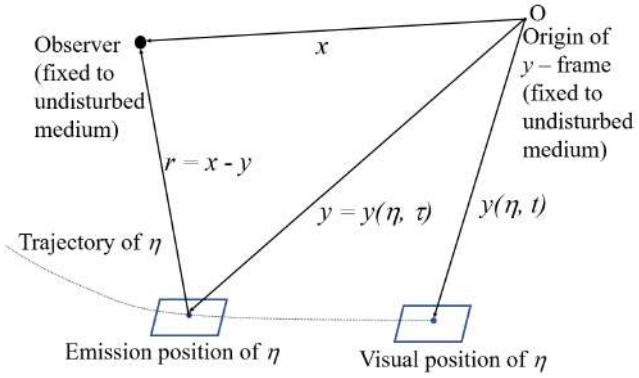

Fig. 2.6.6. Trajectory of a source point as seen by an observer in y - frame.

The far-field observer approximation is given by:

$$\frac{\partial}{\partial x_i} \simeq -\frac{\hat{r}_i}{c_0}\frac{\partial}{\partial t}, \tag{2.6.6}$$

where, $\hat{r}_i = (x_i - y_i)/r$ is the radiation vector. Using the far-field approximation and with the time derivatives taken outside the integral sign, the acoustic pressure is predicted by Equation 2.6.7 known as Farassat Formulation 1 [134]:

$$\begin{aligned} 4\pi p(x,t) &= 4\pi(p_T(x,t) + p_L(x,t)) = \\ &= \frac{\partial}{\partial t}\int_{f_c=0}\left[\frac{c_0\rho_0 v_n + p\cos\theta}{c_0 r(1-M_r)}\right]_\tau dS + \int_{f_c=0}\left[\frac{p\cos\theta}{r^2(1-M_r)}\right]_\tau dS, \end{aligned} \tag{2.6.7}$$

where, M_r is the Mach number of the source in the radiation direction towards the observer at time τ, $\cos\theta = n_i\hat{r}_i$, i.e. θ is the local angle between the normal to the surface and radiation direction $\hat{r}$ at emission time.

To remove the numerical differentiation of an integral thereby reducing computational costs and to improve the numerical accuracy, Formulation 1A was developed [132]. The moving body is defined in a blade fixed frame/Lagragian frame η and the emission time is a function of observer time. The variables (x, η) are also kept fixed. The following relations are utilized [126]:

$$\left.\frac{\partial}{\partial t}\right|_x = \left(\frac{1}{1-M_r}\left.\frac{\partial}{\partial \tau}\right|_x\right)_{ret}, \tag{2.6.8}$$

$$\left(\frac{\partial r}{\partial \tau}\right)_{(x,\eta)} = \frac{\partial r}{\partial y_i}\left(\frac{\partial y_i}{\partial \tau}\right)_{(x,\eta)} = -\hat{r_i}v_i = -v_r, \tag{2.6.9}$$

$$\left(\frac{\partial r}{\partial t}\right)_{(x,\eta)} = \left(\frac{\partial r}{\partial \tau}\right)_{(x,\eta)}\left(\frac{\partial \tau}{\partial t}\right)_{(x,\eta)}. \tag{2.6.10}$$

Applying partial derivative to the emission time equation 2.6.5 and utilizing the above relations yields:

$$\left(\frac{\partial \tau}{\partial t}\right)_{(x,\eta)} = \frac{1}{1-M_r}. \tag{2.6.11}$$

It is important to note here that the variables v_n, M, p and n are functions of (η, τ) and the variable r is a function of $(x; \eta, \tau)$. Taking source time derivatives of the variables:

$$\frac{\partial \hat{r_i}}{\partial \tau} = \frac{\hat{r_i} v_r - v_i}{r}, \tag{2.6.12}$$

$$\frac{\partial M_r}{\partial \tau} = \frac{1}{c_0 r}\left(r_i \dot{v_i} + v_r^2 - v^2\right) = \hat{r_i}\dot{M_i} + \frac{c_0\left(M_r^2 - M^2\right)}{r}, \tag{2.6.13}$$

$$\dot{v_n} \equiv \frac{\partial}{\partial \tau}(v \cdot n) = \dot{v} \cdot n + v \cdot \dot{n} = a_n + v \cdot \omega \times n. \tag{2.6.14}$$

This leads to acoustic pressure prediction formulation known as the Formulation 1A:

$$\begin{aligned} 4\pi p_T(x,t) = &\int_{f_c=0}\left[\frac{\rho_0 \dot{v_n}}{r(1-M_r)^2} + \frac{\rho_0 v_n \hat{r_i}\dot{M_i}}{r(1-M_r)^3}\right]_{ret} dS + \\ &+ \int_{f_c=0}\left[\frac{\rho_0 c_0 v_n (M_r - M^2)}{r^2(1-M_r)^3}\right]_{ret} dS, \end{aligned} \tag{2.6.15}$$

$$\begin{aligned} 4\pi p_L(x,t) = &\int_{f_c=0}\left[\frac{\dot{p}\cos\theta}{c_0 r(1-M_r)^2} + \frac{\hat{r_i}\dot{M_i} p\cos\theta}{c_0 r(1-M_r)^3}\right]_{ret} dS + \\ &+ \int_{f_c=0}\left[\frac{p(\cos\theta - M_i n_i)}{r^2(1-M_r)^2} + \frac{(M_r - M^2)p\cos\theta}{r^2(1-M_r)^3}\right]_{ret} dS. \end{aligned} \tag{2.6.16}$$

These equations are valid for arbitrary blade motion and geometry and is most suitable for bodies with subsonic tip speeds. The above obtained solutions (Farassat's Formulations) to the FW–H analogy are all derived based on acoustic compact body assumptions described in detail in the next section. Compactness conditions for moving bodies are not as simplistic as for the stationary bodies and difficult to adhere to at all conditions. Compact body theories are derived only as a limit of noncompact theories.

The characteristics of the pressure signals in both time and frequency domains are obtained from the following methods. The peak amplitude, the root-mean square of pressure fluctuations (P_{rms}) and the resulting Overall Sound Pressure Level (OASPL) are quantified in the time domain. P_{rms} is defined as the root mean square of the acoustic pressure fluctuations given by Equation 2.6.17 with $p(t)$ being the pressure at time t [125, 135]

$$P_{rms} = \sqrt{\frac{1}{T_2 - T_1}\int_{T_1}^{T_2} p(t)^2 dt}. \tag{2.6.17}$$

The OASPL is given by Equation 2.6.18 with P_0 as reference pressure [125] with a value of 2×10^5 Pa.

$$OASPL = 10\log_{10}\left(\frac{P_{rms}^2}{P_0^2}\right) \tag{2.6.18}$$

For the frequency domain analysis, Discrete Fast Fourier Transform (DFFT) is employed. The dominant frequency, Sound Pressure Level (SPL) spectrum, and the OASPL are computed using Equations 2.6.19 and 2.6.20.

$$SPL = 10\log_{10}\left(\frac{L}{2N^2}\frac{f_A^2}{P_0^2}\right) \tag{2.6.19}$$

where, N is the number of samples in the total time of analysis L and f_A is the amplitude of frequency.

$$OASPL = 10\log_{10}\left(\int_0^\infty 10^{0.1(SPL)}df\right). \tag{2.6.20}$$

2.7 Acoustic compactness

2.7.1 Stationary bodies

For stationary bodies, if the body (source) size is much smaller than the acoustic wavelength λ, it is considered compact. A dimensionless wave equation is given by [125]:

$$\sum_{i=1}^{3}\frac{\partial^2\phi'}{\partial\bar{x_i}^2} = (He)^2\frac{\partial^2\phi'}{\partial\bar{t}^2}, \qquad He = \frac{L}{c_0\tau} = \frac{\omega L}{c_0} = \frac{2\pi L}{\lambda} = kL, \tag{2.7.1}$$

where, τ, L and He are the time, length scale and Helmholtz number respectively. Here, $\bar{t} = t/\tau$ and $\bar{x_i} = x_i/L$. For a body to be compact source $He << 1$ has to be satisfied. This allows for utilizing incompressible potential flow theories to estimate the source behaviour generally at low frequencies where the time derivatives become small. This implies that a compact source body acts as a point source embedded in a larger acoustic field allowing for local incompressible approximations to match far-field solutions such as spherical/plane waves [125].

2.7.2 Moving bodies

The various methods of deriving the integral solutions to the classical equation are based on the acoustic compactness of sources. Obviously this imposes restrictions on the observer position and time. Farassat [131] explained this in great detail using the $\sum$ surface solution. From the right hand side of the wave equation with the two types of acoustic sources (Equation 2.6.1):

$$\Box^2 p = -\frac{\partial}{\partial y_i}\Big[pn_i\left|\nabla f_c\right|\delta\left(f_c\right)\Big]. \tag{2.7.2}$$

The solution to the above equation (2.7.2) is given as follows [131]:

$$4\pi p(x,t) = -\frac{\partial}{\partial x_i}\int_{f_c=0}\left(\frac{pn_i}{r|1-M_r|}\right)_\tau dS. \tag{2.7.3}$$

For a stationary observer, let the time taken by the collapsing sphere to cross the moving body completely be $\tau_c(x,t)$ and $L(x,t)$ is the largest $\sum$ surface characteristic dimension. Implementing certain approximations and using the above solution, a set of conditions on the characteristic scales are evaluated as given below [136]:

1. time scale of pressure variation on the surface (τ_p) is much greater than the time taken by the collapsing sphere to cross the entire body i.e.

$$\tau_p >> \tau_c(x,t), \tag{2.7.4}$$

2. time scale of the variation of speed of the body (τ_v) is much greater than the time taken by the collapsing sphere to cross the entire body i.e.

$$\tau_v >> \tau_c(x,t), \tag{2.7.5}$$

3. shortest distance from the observer to the $\sum$ surface (r_{min}) is much greater than the largest $\sum$ surface i.e.

$$r_{min} >> L(x,t). \tag{2.7.6}$$

If the above conditions are satisfied, then Equation 2.7.3 is rewritten as Equation 2.7.7 effectively treating the moving body as a point source [131].

$$4\pi p(x,t) = -\frac{\partial}{\partial x_i}\frac{1}{(r|1-M_r|)_{\bar{\tau}}}\int_S (pn_i)_\tau dS = -\frac{\partial}{\partial x_i}\left(\frac{F_{pi}}{r|1-M_r|}\right)_{\bar{\tau}} \tag{2.7.7}$$

where, F_p is the net pressure force exerted by the surface S on the medium. The mean source time $\bar{\tau}$ is computed using the following equation:

$$\bar{\tau} - t + \frac{|x - y_B(\bar{\tau})|}{c_0} = 0 \tag{2.7.8}$$

where, $y_B(\bar{\tau})$ is the mean location of the body. If a moving body satisfies the three conditions (Equations 2.7.4 to 2.7.6), it is then considered as a compact source distribution. These conditions depend on the observer position and time. Physically the implication of these compactness conditions is that the global parameters of the moving body influences the acoustic pressure prediction. If the sources are noncompact, then the local pressure on the surface influences the loading signal instead of the net force on the body. Similarly for the thickness signal, the local rate of mass injection is taken instead of the net rate of mass injection. Satisfying all the three conditions for every source panel on the moving body for each and every observer position and time-step makes the usability of the compact theory codes extremely restrictive for moderate and high tip Mach number rotors.

2.7.3 Noncompact source formula

To overcome these compactness restrictions and to be able to predict noise at higher tip speeds ($M_r > 0.98$) and include volumetric source terms, the non-compact source Formulation given by Equation 2.7.9 is derived by Farassat [134]. Since only rotors at subsonic speeds are investigated in this research work, noncompact theory is not presented here. Further details into various noncompact solutions can be found in literature [132].

$$\begin{aligned} 4\pi p(x,t) &= 4\pi(p_T(x,t) + p_L(x,t)) = \\ &= \frac{\partial}{\partial t}\int_{\substack{f_c=0\\g=0}} \frac{\rho_0 c_0 v_n}{r\sin\theta} d\Gamma d\tau + \frac{\partial}{\partial t}\int_{\substack{f_c=0\\g=0}} \frac{l_r}{r\sin\theta} d\Gamma d\tau + \int_{\substack{f_c=0\\g=0}} \frac{c_0 l_r}{r^2\sin\theta} d\Gamma d\tau. \end{aligned} \tag{2.7.9}$$

2.8 Elementary acoustic sources

All acoustic analogies represent various noise generating mechanisms as equivalent elementary sources. The three fundamental acoustic sources namely the monopole, dipole and quadrupole are explained in detail in this section.

2.8.1 Monopole

A monopole or a point source of mass can be visualized as a finite sphere which is pulsating with time. The unsteady volumetric flow addition generates sound. The directivity of a monopole is omnidirectional as observed in the Figure 2.8.7.

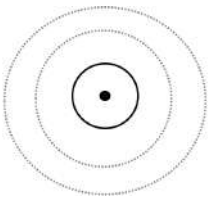

Fig. 2.8.7. Directivity of a monopole.

The sound field for a point source defined by volume flux $Q(t)$ in subsonic motion described by $\overrightarrow{r}(t) = \overrightarrow{x} - \overrightarrow{x_s}(t)$, is given by:

$$\frac{1}{c_0^2}\frac{\partial^2 p}{\partial t^2} - \bigtriangledown^2 p = \rho_0 \frac{\partial}{\partial t} Q(t)\delta(\overrightarrow{r}(t)). \tag{2.8.1}$$

Using the free-field Green's function (Equation 2.6.2), the potential solution is given by Equation 2.8.2:

$$4\pi\phi(x,t) = -\int_{-\infty}^{\infty} \frac{Q(\tau)}{r(\tau)}\delta\left(t - \tau - \frac{r(\tau)}{c_0}\right) d\tau, \qquad r \quad = \quad |\overrightarrow{r}| \tag{2.8.2}$$

where, $p = -\rho_0 \frac{\partial}{\partial t}\phi$. Using the δ function integral form of this solution and applying chain rule differentiation, the acoustic pressure for a moving monopole is given by Equation 2.8.3:

$$4\pi p(x,t) = \frac{\rho_0 Q'_\tau}{r_\tau \left(1 - M_\tau \cos\vartheta_\tau\right)^2} + \rho_0 Q_\tau \frac{\overrightarrow{r_\tau} \cdot \overrightarrow{M'_\tau} + c_0 M_\tau \left(\cos\vartheta_\tau - M_\tau\right)}{r_\tau^2 \left(1 - M_\tau \cos\vartheta_\tau\right)^3}. \tag{2.8.3}$$

The pressure and the potential fields are increased by the Doppler factor $1/\left(1 - M_\tau \cos\vartheta_\tau\right)$, due to the motion of the body. The acoustic pressure for a stationary monopole is obtained from Equation 2.8.3 by setting all variables related to motion, to zero. Thus, all velocity and Mach number variables are excluded leading to Equation 2.8.4:

$$4\pi p(x,t) = \frac{\rho_0 Q'_\tau}{r_\tau}. \tag{2.8.4}$$

The intensity of sound I, for a monopole is defined as $I \propto \rho_0 v_0^4 c_0^{-1} L^2 r^{-2}$. The acoustic efficiency η, i.e. the ratio of acoustic power output to the energy supplied is given by:

$$\eta \propto \left(\frac{v_0}{c_0}\right)^1. \tag{2.8.5}$$

For subsonic Mach number applications, the monopole is the most efficient radiator of sound followed by the dipole and the quadrupole.

2.8.2 Dipole

A dipole or a point source of momentum/force generates sound due to the time-varying forces for example varying forces due to flow separation or vortex shedding etc. It can be visualized as two monopoles that are at a certain distance from each other, with equal strength but of opposite phase. One of them generates a net outflow while the other produces an opposite inflow. A net thrust exerted on the fluid from the positive one to the negative one fluctuates periodically in orientation. The time rate of change of this force on the fluid creates sound. The distance between the two monopoles is kept infinitesimally small compared to the radiated wavelength. The directivity of a dipole is as observed in Figure 2.8.8.

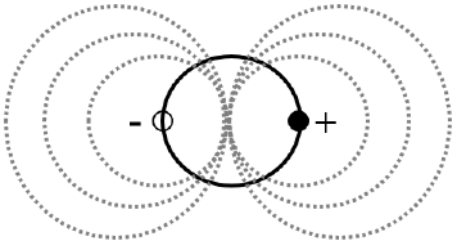

Fig. 2.8.8. Directivity of a dipole.

The acoustic pressure for a dipole/moving point force is derived from the linearized gas Equation 2.8.6 with point force described by $\overrightarrow{F}(t)\delta(\overrightarrow{x} - \overrightarrow{x_s}(t))$.

$$\frac{1}{c_0^2}\frac{\partial^2 p}{\partial t^2} - \bigtriangledown^2 p = \bigtriangledown \cdot \left\{ \overrightarrow{F}(t)\delta(\overrightarrow{r}(t)) \right\}. \tag{2.8.6}$$

Implementing similar mathematical concepts used in the moving monopole derivation, the following solution to the above equation is obtained:

$$4\pi p(x,t) = - \bigtriangledown \cdot \left(\frac{\overrightarrow{F}_\tau}{r_\tau(1 - M_\tau \cos\vartheta_\tau)} \right). \tag{2.8.7}$$

Applying chain rule differentiation, the general equation for the acoustic pressure of a moving point force is given by:

$$4\pi p(x,t) = \frac{\overrightarrow{r}_\tau \cdot \overrightarrow{F'}_\tau - c_0 \overrightarrow{M}_\tau \cdot \overrightarrow{F}_\tau}{c_0 r_\tau^2 (1 - M_\tau \cos\vartheta_\tau)^2} + (\overrightarrow{r}_\tau \cdot \overrightarrow{F}_\tau)\frac{\overrightarrow{r}_\tau \cdot \overrightarrow{M'}_\tau + c_0(1 - M_\tau^2)}{c_0 r_\tau^3 (1 - M_\tau \cos\vartheta_\tau)^3}. \tag{2.8.8}$$

Setting the variables of motion like velocity and Mach numbers to zero in Equation 2.8.8, the acoustic pressure for a stationary dipole with fluctuating force is given by Equation 2.8.9:

$$4\pi p(x,t) = \frac{\overrightarrow{r}_\tau \cdot \overrightarrow{F'}_\tau}{c_0 r_\tau^2} + \frac{\overrightarrow{r}_\tau \cdot \overrightarrow{F}_\tau}{r_\tau^3}. \tag{2.8.9}$$

For both monopole and dipole equations, the $O(r_\tau^{-1})$ denotes the acoustic far-field region while the $O(r_\tau^{-2})$ denotes the acoustic near-field. This demarcation is quite clear for the monopole but, for the dipole a rearrangement of the equation is needed

to separate the near- and far-field terms as presented in Equations 2.8.10 and 2.8.11 respectively:

$$4\pi p_N(x,t) = \frac{-c_0 \overrightarrow{M}_\tau \cdot \overrightarrow{F}_\tau}{c_0 r_\tau^2 (1 - M_\tau \cos\vartheta_\tau)^2} + (\overrightarrow{r}_\tau \cdot \overrightarrow{F}_\tau) \frac{c_0(1 - M_\tau^2)}{c_0 r_\tau^3 (1 - M_\tau \cos\vartheta_\tau)^3}, \tag{2.8.10}$$

$$4\pi p_F(x,t) = \frac{\overrightarrow{r}_\tau \cdot \overrightarrow{F'}_\tau}{c_0 r_\tau^2 (1 - M_\tau \cos\vartheta_\tau)^2} + (\overrightarrow{r}_\tau \cdot \overrightarrow{F}_\tau) \frac{\overrightarrow{r}_\tau \cdot \overrightarrow{M'}_\tau}{c_0 r_\tau^3 (1 - M_\tau \cos\vartheta_\tau)^3}. \tag{2.8.11}$$

The intensity of sound I, for a dipole is defined as $I \propto \rho_0 v_0^6 c_0^{-3} L^2 r^{-2}$ with L being the dimension of the body [124]. The dipole strength per unit volume is proportional to the frequency of velocity fluctuations. The acoustic efficiency η for a dipole is given by:

$$\eta \propto \left(\frac{v_0}{c_0}\right)^3. \tag{2.8.12}$$

2.8.3 Quadrupole

A quadrupole is a volumetric source term that is generated due to fluctuating Reynolds stresses. It can be visualized as four monopoles (or two dipoles) created by collisions of fluid elements. The net shear effects of the flow may reduce to a local stress on the fluid. The time rate of change of this stress produces sound. The fluid flow does not support such forces strongly thus quadrupoles are relatively poor radiators of noise except in mixing region of jet flow. The directivity is given by Figure 2.8.9.

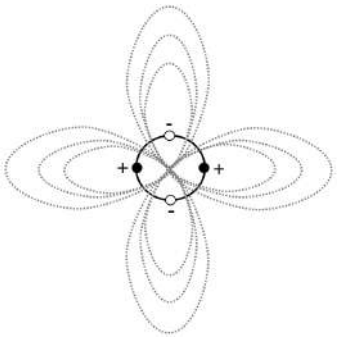

Fig. 2.8.9. Directivity of a quadrupole.

The strength of a quadrupole per unit volume is proportional to double the frequency of the fluctuating velocity. The intensity is given by $I_Q \sim \rho_0 v_0^8 c_0^{-5} L^2 r^{-2}$. The acoustic efficiency is given by:

$$\eta \propto \left(\frac{v_0}{c_0}\right)^5. \tag{2.8.13}$$

The characteristics of all the three elementary sources [50] are summarized in the Table 2.8.1.

Tab. 2.8.1. Properties of elementary sources

Source	Monopole	Dipole	Quadrupole
Mechanism	Fluctuating injection of mass	Fluctuating injection of momentum/ unsteady forces acting on the fluid	Fluctuating Reynolds stresses/system of both normal and shear stresses
Strength	Rate of change of mass inflow/outflow	Forces acting on the fluid	Lighthill tensor T_{ij}
Quantity	Scalar	Vector	Tensor
Directivity	Omnidirectional	Two lobes	Four lobes for lateral and two lobes for longitudinal
Applications	Siren, moving volume	Rotating/fluctuating forces on blades/ propellers/fans	Turbulent flows

2.9 Acoustic beamforming

Acoustic beamforming is an acoustic imaging method to localize and quantify sound sources by measuring pressure signals in the time domain using phased microphone array and interpreting the signals in the frequency domain [137]. Depending on the propagation distance i.e. the distance between the source and each microphone, the array will perceive a different phase. Since the source position and the sensor locations are exactly defined, the complex sound sources are modelled as a distribution of monopole sources. The pressure signals excite the microphone membrane that converts the signals into AC voltage. This voltage then gets amplified in the microphone preamplifier (reduces background electronic noise). It is low-pass filtered (to avoid alias effects) by the analog-to-digital convertor [138]. The continuous measured pressure signal $p(t)$ is stored as a discrete set of data $p(n\Delta t)$ at constant time steps $\Delta t = 1/f_s$, where f_s is the sampling frequency and n is an integer. To allow for the use of complex post-processing beamforming techniques (section 2.9.1), the Fast Fourier Transform is applied on the discrete data:

$$p(f) = \frac{2}{K} \sum_{n=1}^{K} p(t) e^{-2\pi i f n \Delta t} \tag{2.9.1}$$

where, K is the data block with a power of 2. The frequency domain data is represented as discrete frequencies in steps of an integer multiple (n) of f_s/K with an upper Nyquist frequency limit of $f_s/2$. Analysis of the measured acoustic data presented in Chapter 6 is conducted utilizing a beamforming code (implemented in Matlab) available within the Wind Energy team at Delft University of Technology.

2.9.1 Conventional frequency domain beamforming (CBF)

Conventional frequency domain beamforming (CBF) technique allows for a complex post-processing of the measured data, thus, improving results [139]. The noise source is considered as a search grid plane which is located at a certain fixed distance from the array of microphones m (Figure 2.9.10). For every grid node the corresponding time signal is obtained by each microphone at a retarded time. The beamformer output

map is obtained by summing and dividing the signals from all the microphones by the number of microphones. A constructive interference occurs when there is a source causing the beamformer signal to amplify while a destructive interference occurs in the absence of a source leading to small amplitudes [138].

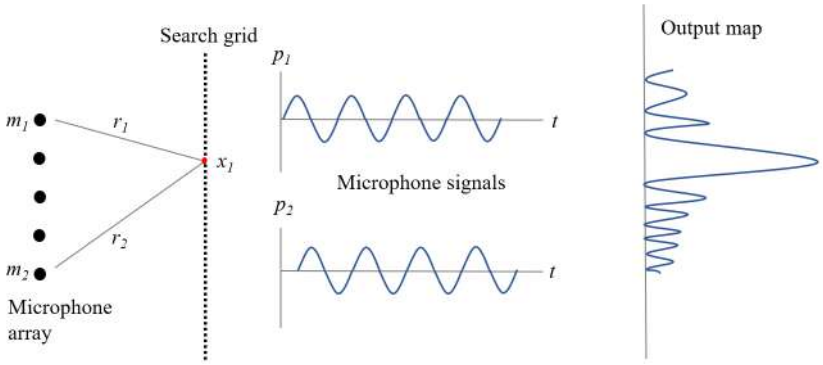

Fig. 2.9.10. Beamforming technique [140].

The beamformer signal is presented in Equation 2.9.2 and it's Fourier transform in Equation 2.9.3:

$$L(t, \overrightarrow{x}_s) = \frac{4\pi}{N} \sum_{n=1}^{N} p_m(\overrightarrow{x}_s, t + t_0) |\overrightarrow{x} - \overrightarrow{x}_0| \tag{2.9.2}$$

$$L(\omega, \overrightarrow{x}_0) = \mathcal{F}z(t) = \frac{1}{M} \sum_{n=1}^{M} s(\overrightarrow{x}, \omega) P(\overrightarrow{x}, \overrightarrow{x_s}, \omega) \tag{2.9.3}$$

where, p_m is the pressure measured by the microphone, $L(t)$ is the beamformer output, N is the number of microphones, x_m is the microphone location, x_s is the source position, ω is the angular frequency and $s(\overrightarrow{x}_m, \overrightarrow{x}_s, \omega)$ is the steering function.

$$s(\overrightarrow{x}_m, \overrightarrow{x}_s, \omega) = 4\pi |\overrightarrow{x} - \overrightarrow{x}_s| e^{-i\omega t_0} \tag{2.9.4}$$

The steering vector which is normalized by the distance between the source and the microphone array centre is given below:

$$\hat{e}(\overrightarrow{x}, \omega) = \frac{1}{|\overrightarrow{x}_c - \overrightarrow{x}_0|} \begin{pmatrix} |\overrightarrow{x}_1 - \overrightarrow{x}_0 e^{-i\omega t_1}| \\ |\overrightarrow{x}_1 - \overrightarrow{x}_0 e^{-i\omega t_2}| \\ \cdot \\ \cdot \\ \cdot \\ |\overrightarrow{x}_N - \overrightarrow{x}_0 e^{-i\omega t_N}| \end{pmatrix} \tag{2.9.5}$$

where, $x_1 ....x_N$ is the position of each microphone, $t_1 .....t_N$ is the propagation time between the source grid points and the corresponding microphone and x_c is the microphone array center position. The vector form of the Fourier transformed microphone signals is presented in Equation 2.9.6 and the beamformer output in the matrix form by Equation 2.9.7.

$$Y(\omega) = \begin{pmatrix} P_1(\omega) \\ P_2(\omega) \\ . \\ . \\ . \\ P_N(\omega) \end{pmatrix} \tag{2.9.6}$$

$$Z(\omega) = \frac{g(\overrightarrow{x}, \omega)^{\dagger} Y(\omega)}{N} \tag{2.9.7}$$

where, † denotes a transpose and complex conjugated vector. The power spectral density (PSD) of a signal describes its power distribution over the frequency. The Cross-Spectral Matrix (CSM) is a method of estimating the degree of correlation between two signals. It is defined using the cross-power spectral densities of each microphone pair combination along with their complex conjugates and the auto-power spectra of each microphone in the diagonal [140]. It is defined for all frequencies. The diagonal elements of the matrix describes the statistical variance of the noise. Often times the pseudo noise contaminates the diagonal elements for instance when the microphones are subjected to the flow. This effect can be minimized by removing the diagonal elements [138]. There are several methods available for estimating CSM, the Welch method being the most popular one [141].

$$C_{mn} = E(p_m(f)(p_m(f))^*) + \sigma^2 I \tag{2.9.8}$$

where, m, n are the microphone numbers, $\sigma^2 I$ represents the statistical variance.

$$CSM(\omega) = Y(\omega)Y(\omega)^{\dagger} = \begin{pmatrix} Y_1 Y_1^* & ... & Y_1 Y_N^* \\ & . & \\ & . & \\ & . & \\ Y_N Y_1^* & ... & Y_N Y_N^* \end{pmatrix} \tag{2.9.9}$$

Each individual microphone has a certain spatial distribution. The array acts as a spatial filter bank since it is not feasible to have a continuous distribution of microphones [140]. A perfect array would capture a monopole source as an infinitesimally small point output without any pseudo sound sources. But, in reality, due to the discontinuous distribution of the microphones in the array and its finite size, contamination of the beamforming output map with side-lobes (pseudo sound sources) occurs. This is quantified using the Point-Spread-Function (PSF). PSF defines how a particular microphone array responds to a point source (monopole) placed in front of the array. It gives the main to side-lobe ratio (MSR) that describes the array performance capabilities. This has been investigated extensively and suitable recommendations for array geometries to have higher MSR ratios are proposed [138].

Due to both practical and financial constraints on increasing the number of microphones, data acquisition systems etc., effective deconvolution techniques have been developed to improve array performance [142]. The idea behind deconvolution techniques is that, an image (h_{img}) is a convolution of the actual image (f_{img}) and a certain transfer function (g_{img}) that represents the array response to a given source (array PSF) with $*$ as the convolution operator:

$$h_{img} = f_{img} * g_{img}. \tag{2.9.10}$$

2.9.2 CleanSC method

Since the source distribution is convoluted with the source map, deconvolution techniques are applied to quantify the noise sources. Several deconvolution techniques for example linear programming method [143], global optimization methods [144], DAMAS [142], CLEAN-PSF [145], SODIX [146] etc. have been investigated. One such method that is utilized in the analysis of measured data in section 6.5 is the CLEAN-SC method. At high frequencies, the CBF method has the drawback of the presence of side-lobes from the dominant sources. These side-lobes mask weaker secondary sound sources hiding important acoustic characteristics [145]. The Rayleigh resolution of the array also imposes an important limitation. To address this, a deconvolution method called the CLEAN-SC based on the CLEAN technique from astronomy is implemented [147]. Different techniques have been investigated to improve the CLEAN-SC method such as the High Resolution CLEAN-SC (HR-CLEAN-SC) [148], Enhanced HR-CLEAN-SC [149].

Deconvolution techniques can only be applied to statistically uncorrelated sources, which is in reality not possible [140]. Due to their finite size, acoustic sources in practical applications exhibit spatial correlation. The side-lobes which are quantified using the PSF of a microphone array, are assumed to be spatially coherent with the main lobe in the CLEAN-SC method. The contribution of side-lobes are removed from the CSM matrix in an iterative process to have only clean beams in the source map. Further details on the particular beamforming procedure used in this research work can be found in [149]. The measured CSM is divided into two parts - the incoherent sources (K) and the $C_{degraded}$ which consists of not yet extracted source information:

$$C_{meas} = \sum_{k=1}^{K} p_k p_k^* + C_{degraded} \tag{2.9.11}$$

where, p_k are the N dimensional acoustic source vectors representing the Fourier components of the signals from the k^{th} source. At the first iterative step since the number of sources is unknown, $C_{meas} = C_{degraded}$. To obtain the source information from C_{meas} and transfer it to the first term on the RHS of Equation 2.9.11, the source power is defined by Equation 2.9.12. With some approximations such as the contribution from the other sources is small compared to the first one etc. as explained in [149], Equation 2.9.13 is derived.

$$\tilde{A}_s = w_s^* C_{meas} w_s = w_s^* \left[\sum_{k=1}^{K} p_k p_k^* + C_{degraded} \right] w_s \tag{2.9.12}$$

$$\tilde{A}_s \approx |p_1^* w_s|^2 + \sum_{k=2}^{K} |p_k^* w_s|^2 \approx |p_1^* w_s|^2 \tag{2.9.13}$$

where, $\tilde{A}_s$ is the estimated source power at grid point s and w_s is the weight vector defined as $w_s = e_s/||e_s||^2$ with e being the steering vector. The source component h_s that represents the particular source's contribution to the CSM is defined as:

$$h_s \equiv \frac{C_{meas} w_s}{|p_1^* w_s|^2} \approx \frac{p_1}{|p_1^* w_s|} \tag{2.9.14}$$

The source component is removed from the measured CSM before the next iterative step. A loop gain ϕ is defined to include the small contribution from other unidentified sources:

$$\phi \tilde{A}_s = |p_1^* w_s|^2 \tag{2.9.15}$$

with the loop gain varying as $0 < \phi \leq 1$. This estimates the contribution of the identified source at $k = 1$ to the total source power at grid point s. The degraded CSM is obtained by:

$$C_{degraded} = C_{meas} - p_1 p_1^* = C_{meas} - |p_1^* w_s|^2 h_s h_s^* = C_{meas} - \phi \tilde{A}_s h_s h_s^* \tag{2.9.16}$$

which replaces C_{meas} in Equation 2.9.12 for the next iteration to identify the next grid point with the source peak. This process is then repeated until the $C_{degraded}$ is empty. This implies all the source components of all the incoherent sources are removed i.e. $||C_{degraded}|| < \epsilon ||C_{meas}||$ with $\epsilon = 0.01$ constant. Thus the exact number of sources are identified and the summation of all the clean beamformer maps is conducted such as:

$$\tilde{A}_j = \sum_{k' \in S} \phi \tilde{A}_{k'} 10^{\beta d_{j,k'}^2} + w_j^* C_{degraded} w_j \tag{2.9.17}$$

where β, $d_{j,k'}$ are the shape parameter for the clean map, the distance from grid point j to the identified source location at grid point k' respectively [149]. The CLEAN-SC method removes the side-lobes which are spatially coherent with the main lobe. The sources which are spaced closer than the Rayleigh limit, the CLEAN-SC locates the source markers between them.

Chapter 3

FW–H code development and validation

The detailed implementation and validation of the aeroacoustic code based on the integral solution to the exact FW–H equation derived by Farassat are presented in this chapter[1]. Additionally, the computationally inexpensive numerical codes to obtain the analytical solutions for elementary acoustic sources are also presented here. A thorough validation of the code for the envisioned four main elementary cases (described in section 1.6) are presented both qualitatively and quantitatively.

The primary reason to implement a FW–H code is to have a general in-house tool to investigate the sound emitted by various rotating bodies operating at both design and off-design conditions. This code is capable of investigating rotor blades equipped with different add-ons – passive flow control devices (vortex generators etc.) or active flow control devices (impinging jets etc.). It is a tool enabled to conduct acoustic investigations on existing CFD flow data (post-processing code) and also for new investigations during design stages. This is achieved by implementing the code using Tecplot 360 EX, a commercial post-processing software developed by Tecplot Inc [151]. The analytical solutions (for elementary sources) that are utilized for the validation of the FW–H code, obtained from equations (Equations 2.8.3 and 2.8.8) are also solved using Tecplot scripting.

Tecplot is a collection of tools for visualizing and in-depth analysis of diverse, large CFD data sets and automated workflows. It is a robust application for post-processing technical data. It allows large data import from a wide range of data formats (ordered/finite element, non-commercial/commercial CFD solvers etc.). This strong feature of Tecplot allows the developed aeroacoustic code to be utilized as a general tool. The scripting language of Tecplot provides several in-built features particularly the spatial and time integration of flow variables, computation of surface normals and volume and Discrete Fast Fourier Transform options that are currently utilized in the code implementation. These features enable complex manipulation of very large data sets and reduces the computation time. Hence, the aeroacoustic code based on the Farassat's Formulations (Equations 2.6.15 and 2.6.16) are implemented using Tecplot's macro scripting language.

Additionally, it enables for parallelization of the code through parallel processing (shared memory) and multiple zones and variables. This allows for running the code on a large CFD mesh by splitting the domain into individual zones and running analysis.

[1]Some parts of the text in this chapter have been published in Archives of Mechanics [150].

This drastically reduces the computation time. Furthermore, the code can be sped up by converting it into a python code using PyTecplot API in the future. Eventually, the entire code can be completely implemented in Python by adding input CFD data functionality thus making it fully open source.

The developed aeroacoustic code allows for a detailed acoustic analysis for various applications, thus, aiding a deep understanding of the sound generation and propagation mechanisms. The benefits of the in-house code over a commerical code is presented in detail at the end of the following section.

3.1 Aeroacoustic code based on FW–H analogy

A post-processing aeroacoustic code based on the linear integral solution to the FW–H analogy derived by Farassat is developed. Firstly, the relatively simpler Formulation 1 (Equation 2.6.7) is implemented. This was tested against the experimental data for a model UH-1H helicopter rotor [152]. Based on this experience, implementation of the more sophisticated Formulation 1A (Equations 2.6.15 and 2.6.16) is conducted. The benefits of utilizing Formulation 1A over Formulation 1 is discussed in section 2.6.

The code is split into two parts – main script and addition script presented in Figure 3.1.1. Firstly, the rotor parameters such as rotor blade radius, rotational speed, time period, number of revolutions, number of panels, microphone location etc. and ambient conditions such as pressure, temperature and density are provided. Followed by the surface grid (rotor blade geometric data) and the surface pressure distribution over the body which are fed as input for thickness and loading noise respectively. This input data can be obtained from low fidelity methods such as BEMT or from detailed CFD analysis. The blade is discretized (from CFD analysis) into a few blocks with each block containing mesh cells. These mesh cells act as acoustic sources that are fed as input to the acoustic code. The blocks can be analyzed together – serial computation or individually – parallel computation to obtain the acoustic potential. The code rotates the body to have the necessary revolutions required for frequency analysis. The required source data such as source location (with reference to the frame fixed to the undisturbed medium) and pressure distribution for each panel at every time-step is computed if it is not provided with the input data. Then the code computes all the variables of the Formulation for every panel at each emission time-step and location. The acoustic potential for all the source panels at all the time-steps are estimated and stored in subzones. This data is written to an intermediary output file. This file can also be used for in-depth analysis of particular acoustic variables and their influence on the overall sound levels.

The addition script loads all the subzones with the acoustic potential. It computes the correct observer time for all the panels based on the retarded time approach (Equation 2.6.5). The total acoustic pressure signal in time domain is then obtained by linear integration of the acoustic potential from all contributing panels at every observer time-step. To obtain the pressure signals in the frequency domain and to obtain the OASPL, Fourier analysis is performed.

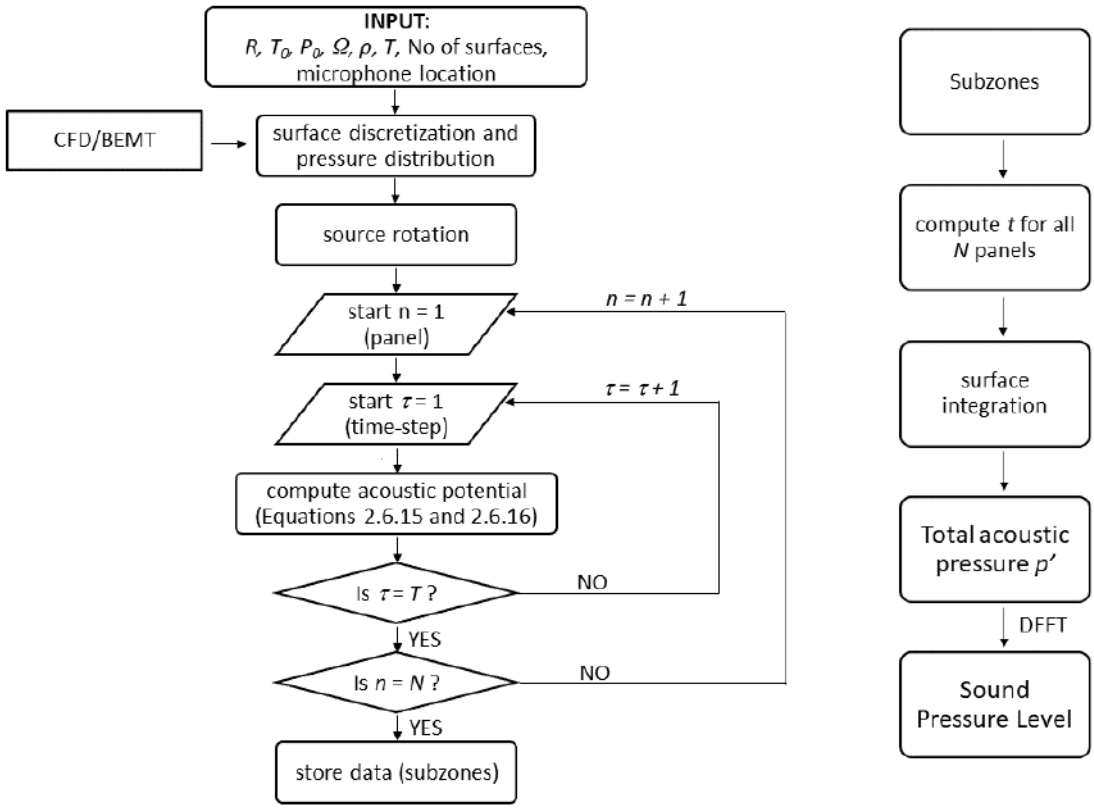

Fig. 3.1.1. Schematic representation of the FW–H code algorithm - main script (left) and addition scipt (right).

For acoustic prediction of complex rotating bodies (such as helicopter rotor blades, wind turbine blades etc.), the CFD grid discretization (used for flow analysis), can be directly used as equivalent elementary source panels. Thus, allowing for acoustic analysis to be conducted on existing flow data. The required surface pressure distribution can be obtained from either low fidelity methods such as Blade Element Momentum Theory (BEMT) for preliminary analysis or through detailed CFD steady/unsteady flow simulations.

The surface under the acoustic investigation is discretized into several acoustic panels. Each surface mesh cell is treated as a distinct source panel (Figure 3.1.2) for which the acoustic potential (i.e. integrands in Equations 2.6.15 and 2.6.16) are evaluated in emission time (τ) domain. The acoustic potential of a single panel depends on its initial position (orientation in space) and motion in relation to the observer. All the required variables that make up the acoustic potential such as the total velocity (V), normal velocity (v_n), normal vector (n), Mach number (M), Mach towards the observer (M_r), distance between the panel and the observer (r) are computed for every panel.

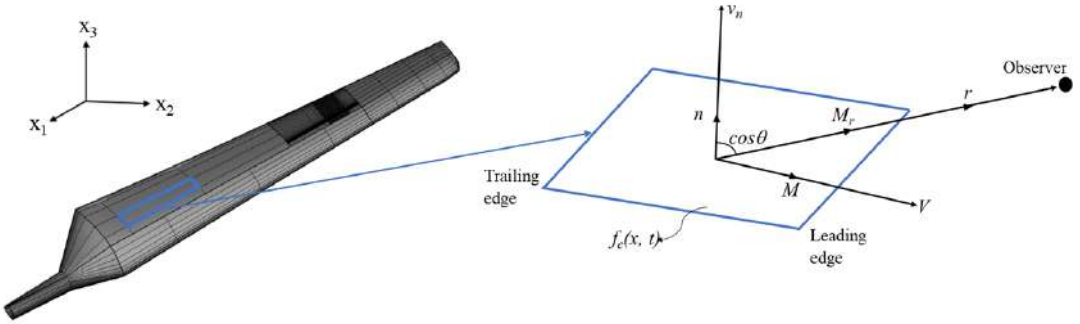

Fig. 3.1.2. Sketch of a single acoustic source panel.

It is important to note that some scalar variables like the pressure and Mach number are to be expressed with both their magnitude and direction. This is to account for their variation in space that is caused by the motion of the body. In many cases even though their magnitude remains constant, their components in the coordinate system varies with the rotating body. This is counter intuitive for flow analysts. A thumb rule to follow is that all the variables are a function of both space and time and are defined in the Lagrangian reference frame – η, which is fixed to the blade known as blade-fixed frame. The final acoustic pressure is evaluated in the observer space-time reference.

There are numerous retarded time algorithms designed for evaluation of Farassat's Formulation 1A integrals, such as source-time dominant, mid-panel and high accuracy quadratures, or supersonic source motion [84]. The source-time dominant method is implemented in the FW–H code, since it is numerically simple (non-iterative) and relatively easy to interpret. All the variables are evaluated at the source retarded (emission) time. The primary application of the developed FW–H code is the acoustic analysis of rotating blades for stationary observers. Thus the unique observer time (t) is computed for every acoustic panel at each emission time-step using the retarded time relation (Equation 2.4.4). Finally, the multiple source contributions at correct observer time are added together to obtain the total acoustic pressure signal at the listener position.

For numerical time differentiation, the fourth-order schemes have been implemented [152], while for surface integrals, a second order mid-panel approximation is used. It is important to emphasize that the final noise signature recorded at given observer location depends not only on the strength of the sources, but is significantly affected by the cancellation/amplification effects due to the variability of the reception time (phase difference) of the acoustic panels (distributed sources).

The features of developing this particular general code for acoustic analysis are listed below:

1. the aeroacoustic code allows for multiple data format input capabilities. Therefore it can be utilized for acoustic investigations for new projects and also for post-processing of existing numerical data (e.g. RANS/URANS)
2. it can be used for investigating several applications (helicopter rotor blades, wind turbine rotors, propellers, unmanned aerial vehicles etc.) with varying geometric shapes (e.g. twisted/untwisted blades, root/tip caps etc.) in subsonic motion as long as the surface discretization and its pressure distribution are provided

3. investigation of various add-ons and flow control techniques (e.g. VGs, serrations, porous materials etc.) implemented on different applications can be conducted
4. calculation of the acoustic variables for a single panel is performed independently of the other neighbouring panels. Thereby, facilitating both serial and parallel runs, thus reducing computational costs. Parallel computation involves analyzing the rotor blade in smaller discrete sections/blocks. This allows for both local and global analysis of specific parts of the blade (e.g. root/tip section, leading/trailing edge, add-ons etc.) aiding quick and efficient design for noise control
5. the total pressure signal along with its various components - thickness and loading noise with further classification into their near- and far-field components are predicted. Furthermore, it allows for analyzing each variable (along with it's behaviour over time) of the acoustic potential independently in any specific/entire region of the blade. This enables a thorough understanding of the various noise source mechanisms aiding better design of noise control methods for specific operating conditions and purposes
6. feasible for an easy extension of the code for investigating transonic/supersonic flows using porous surface FW–H analysis to include volumetric source terms. This extension can be readily implemented on the existing framework.

3.2 Codes to obtain analytical solutions

The validation of the FW–H code is achieved through analytical solutions to the acoustic pressure prediction for the fundamental sources - monopole (Equation 2.8.3) and dipole (Equation 2.8.8), compared against the FW–H code predictions. The discretization of the analytical solutions are also implemented using the Tecplot macro scipting language. The main idea behind these codes is to have a point source (instead of a solid body) that mimics real life applications for instance a rotating rotor blade. This is accomplished through two sets of numerical codes - one set for a single point source, both monopole and dipole (section 3.2.1) and another set of codes for distributed point sources, again, both, monopole and dipole (sections 3.2.2 and 3.2.3). The code performs the relatively simpler computation of the variables of the analytical equations for either a single point source (section 3.2.1) or a distibution of point sources (sections 3.2.2 and 3.2.3) to obtain the acoustic potential. The acoustic potentials at different time-steps are then simply added to obtain the total signal. To summarize the various numerical codes to obtain analytical solutions for:

1. the two, stationary, elementary point sources – monopole and dipole (section 3.2.1)
2. the two, rotating, elementary point sources – monopole and dipole (section 3.2.1)
3. the distributed monopoles – thickness noise modelling (section 3.2.2)
4. the distributed dipoles – loading noise modelling (section 3.2.3).

3.2.1 Elementary point source code

For the stationary monopole case, the variables for motion in Equation 2.8.3 such as velocity, Mach number, Mach towards the observer etc. are all set to zero. The estimation of all the variables are performed similarly to the FW–H code. The algorithm of the code along with the numerical schemes are also retained from the acoustic code. Similarly, for the analytical loading noise prediction, codes based on the Equation 2.8.8

are developed for a point force to obtain results. As for the stationary monopole case, the movement variables are set to zero for the stationary dipole case. The algorithm of these codes is represented in Figure 3.2.3.

The input to the code consists of source parameters such as distance of the source to origin, rotational speed, time period, number of revolutions, microphone location etc. and ambient conditions such as pressure, temperature and density. In addition an input of volumetric mass flux is needed if the source is monopole and of force if the source is a dipole. Next, the point source is rotated to have the necessary periods of revolution. All the variables of the acoustic potential given by Equation 2.8.3 for a monopole or by Equation 2.8.8 for a dipole are computed at every time-step. The total acoustic pressure signal is then estimated through linear summation of all the potentials. To obtain the signal in frequency domain, DFFT is conducted.

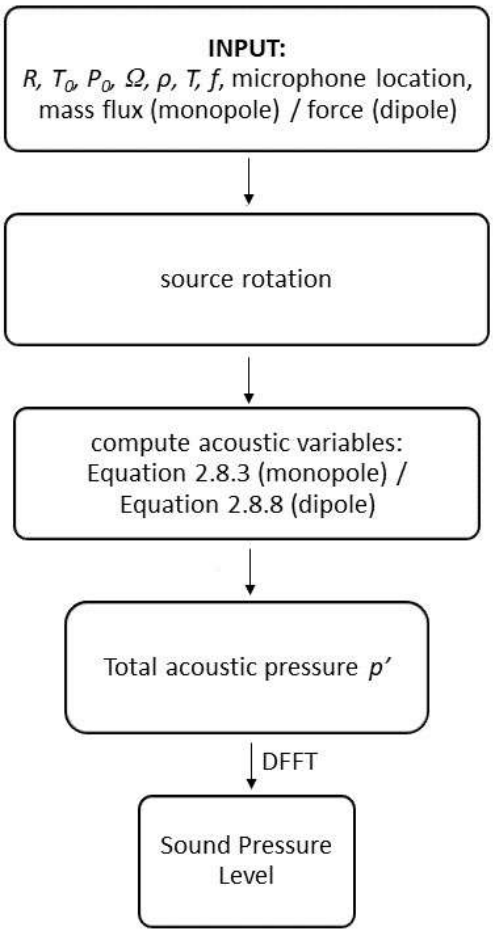

Fig. 3.2.3. Schematic representation of the elementary point source code.

For the analytical solutions, the impact of the number of samples is limited by taking a sufficiently small time-step $\triangle t$. Furthermore, the signal length is kept sufficient for reasonable DFFT of the acoustic pressure (Appendix A.1).

3.2.2 Thickness noise modelling

The FW–H code prediction of noise for rotating body applications is computationally expensive and time consuming. Instead, a quick preliminary analysis can also be conducted by utilizing the analytical elementary source codes (for a single point source) with some modifications (distributed point sources) to investigate complex geometries. This is presented in Figure 3.2.4 where s defines a single source. The framework for the distributed sources code is based on the single elementary source code approach presented in Figure 3.2.3. The single source code is extended to include a distribution of sources that represent the practical application (for instance the rotor blade). The sources can be distributed depending on the type of investigation.

To investigate thickness noise for example, a simple source-sink pair of monopoles can be applied at the leading and trailing edge respectively (with the distance between them = chord) at the tip of the rotor blade [69] similar to what is presented in section 3.6 or can have a number of these source-sink pairs along the entire span of the blade. The point source is modelled as a source/sink depending on the positive/negative mass flux respectively. It consists of running the analytical monopole code twice, each time independently as source and sink to collect their respective acoustic potentials obtained from Equation 2.8.3. These potentials for the source-sink pair are then linearly summed up at correct observer time to obtain the total thickness noise.

3.2.3 Loading noise modelling

Similarly, the FW–H code prediction of loading noise for practical appplications is cumbersome and requires extensive flow analysis (RANS/URANS/LES) to obtain the surface pressure distribution over the rotating blades. For a simplified approximate estimation (Figure 3.2.4), the loading noise is modelled as an equivalent distribution of moving forces – both in-plane and out-of-plane forces along the span of the blade (presented in Chapter 4). The acoustic pressure obtained from Equation 2.8.8 for each point force is summed up to obtain the total loading pressure. The forces are applied at quarter chord of the blade (compact chord assumption [153]). Both in-plane and out-of-plane forces can be obtained from the classical CFD pressure distribution or from the relatively quicker BEMT method (Chapter 4). Coupling the simplified source generation method i.e. BEMT with the simplified source propagation method i.e. analytical loading distributed code reduces the computational cost required for acoustic analysis significantly and provides a reasonable intial estimation. It also allows for acoustic analysis of add-ons such as vortex generators. The impact of VGs can be estimated through the modelling of forces (for example jBAY modelling [154]) and used as an input to the distributed loading noise code.

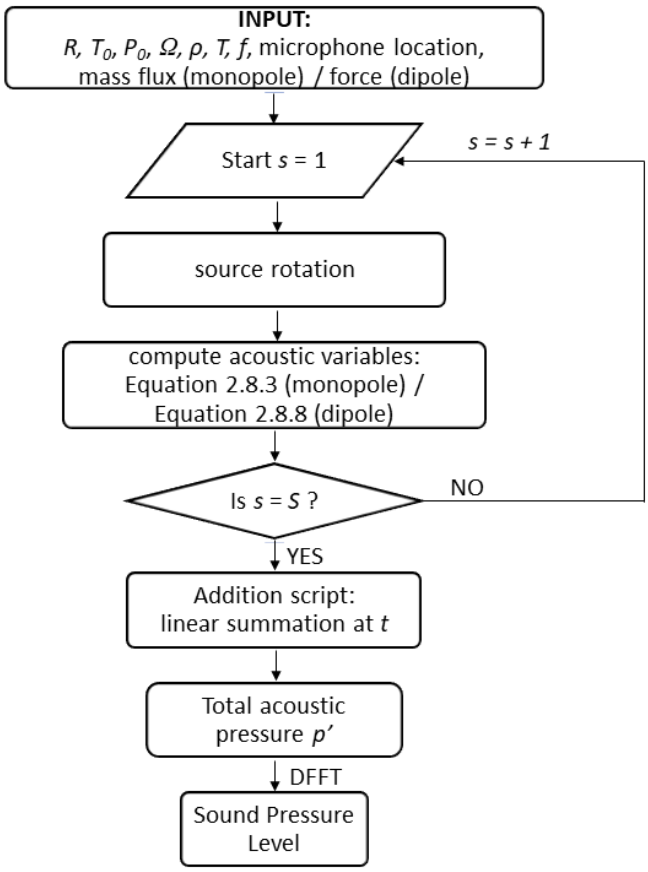

Fig. 3.2.4. Schematic representation of the distributed elementary source code.

3.3 Methodology of validation

The accuracy of the developed FW–H code is validated for the primarily important thickness and loading noise mechanisms of rotor blades through the elementary acoustic sources (monopole and dipole) both, for stationary and moving sources. The stationary sources consist of unsteady source of mass (monopole) and fluctuating source of momentum/force (dipole) while the rotating sources consist of rotating source of steady/unsteady mass (monopole) and rotating source of steady momentum (dipole). The acoustic pressure predicted by the code is compared against analytical solutions obtained from Equations 2.8.3, 2.8.4, 2.8.8 and 2.8.9. Firstly, the simple non-rotating point sources are validated followed by the rotating sources.

3.3.1 Monopole model

The monopole (point source of mass) is modelled as a sphere of finite (small) radius with constant/fluctuating surface mass flux. The surface of this sphere is meshed using Interactive Grid Generator (IGG)/Numeca (now Cadence). The topology of the structured multi-block mesh contains 6 blocks. Each of these blocks contains 16×16 (256) mesh cells (Figure 3.3.5). Each mesh cell is considered as an acoustic panel. Mesh convergence study is conducted to determine the number of cells required on

each block. To achieve this, coarse, medium and fine grids consisting of 96, 384, and 1536 cells, each mesh block refined twice in all directions are utilized.

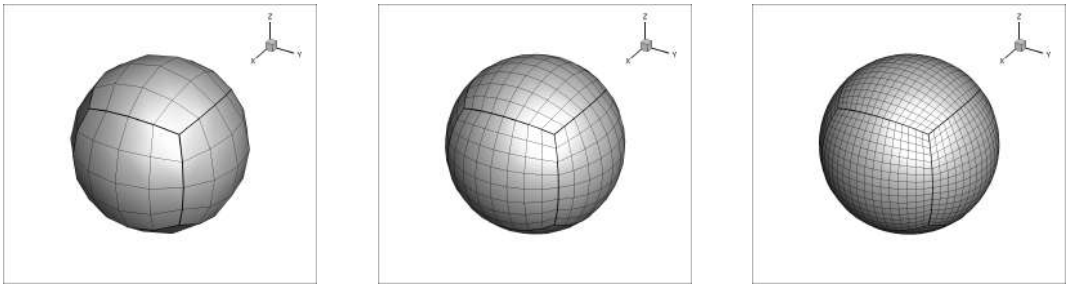

(a) Coarse (b) Medium (c) Fine

Fig. 3.3.5. Surface grid refinement for the modelled monopole source.

3.3.2 Dipole model

Analogously, dipole is modelled as a point source of momentum – in-plane/out-of-plane/radial forces. These point forces can be stationary or rotating, steady or fluctuating. It is equivalent to a disc of finite (small) radius with a force applied perpendicularly. The orientation of the disc along with the force is rotated to model the three types - the out-of-plane, the in-plane and the radial dipoles. The topology of the structured multi-block grid of the disc surface contains 5 blocks (IGG). Each block contains 16×16 (256) cells. The convergence study for the mesh cells on the disc is conducted with coarse (80 elements), medium (320 elements) and fine grids (1280 elements) as observed in Figure 3.3.6.

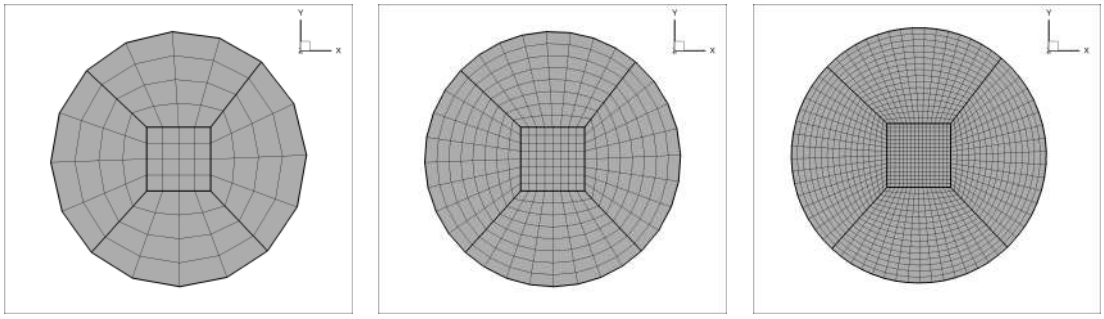

(a) Coarse (b) Medium (c) Fine

Fig. 3.3.6. Surface grid refinement for the modelled dipole source.

The source discretizetions are comparable between the monopole and dipole by ensuring that the number of acoustic panels per unit surface area is constant at each refinement level. The source size dependency analysis is conducted for the sphere/disc of radii 0.025 m, 0.0125 m, 0.006 25 m (relative factor of 2). Ideally, the source is a point with zero radius. But, since it is modelled here as a small sphere/disc with a finite radius, these above mentioned radii values are arbitrarily chosen. To ensure this choice does not affect the solutions, convergence studies are performed. Additionally,

the time-step convergence study is performed for T/180, T/360, T/720 (T = period of rotation) with a relative growth factor of 2. However, solutions with a much higher time-step of T/5760 samples are presented, since they produce signals with significantly improved characteristics specifically in the frequency domain.

The acoustic signals predicted by both analytical and FW–H code, are compared in time and frequency domains both qualitatively and quantitatively. All analytical solutions presented are computed with $\triangle t = T/10000$, T being the period of rotation and for at least 2.5 periods of rotation (see convergence study in Appendix A.1).

The discretizetion of the source size, time-step and element size is improved until the relative error for all the considered metrics falls below 0.5%. The relative error is computed as the difference between analytical and predicted FW–H code values divided by the reference analytical one. This criterion of $< 0.5\%$ is chosen since it provides sufficient accuracy and there is no observable difference in the signals with further lower error values. Additionally, the computational cost also increases significantly if the error criterion is decreased further.

3.4 Stationary monopole

The stationary monopole is modelled as a sphere with fluctuating volumetric mass flux. This sphere has a mass flux $Q = A\sin(\omega t)$ of maximum amplitude A = 0.1 kg/s, pulsating with a frequency (f) of 100 Hz. These values are an arbitrary choice. The far-field stationary observer is located at a distance of 8 m in the source plane. This location is chosen to mimic the model helicopter rotor case presented in Chapter 4. For a stationary monopole, the thickness near-field terms (right hand terms in Equation 2.8.3) are absent thus, the far-field terms (left hand terms in Equation 2.8.3) contribute wholly to the total acoustic pressure. The predicted signal is compared with the analytical solution obtained from Equation 2.8.4. If the sphere has a positive rate of varying mass flow ($Q+$), it acts as an elementary source and if it is a negative mass flux, it acts as an elementary sink ($Q-$). The sound heard by the far-field observer is presented in Figure 3.4.7.

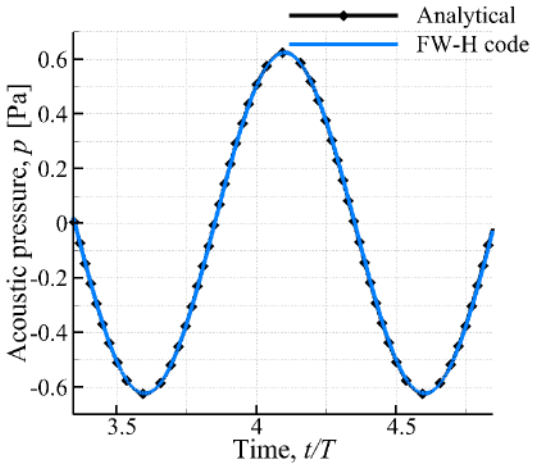

Fig. 3.4.7. Total acoustic pressure (p') for a stationary monopole.

The sound emitted at the far-field is of sinusoidal nature (Figure 3.4.7). The FW–H code prediction is in good agreement with the analytical solution qualitatively. Further noise metrics are presented in the time domain (Table 3.4.1) and frequency domain (Table 3.4.2). These values are computed from Equations 2.6.17-2.6.20.

Tab. 3.4.1. Time domain analysis

	P_{rms} (Pa)	Error (%)	OASPL (dB)	Error (dB)
Analytical	0.195	–	86.886	–
FW-H	0.194	-0.47	86.865	-0.02

Tab. 3.4.2. Frequency domain analysis

	Frequency (Hz)	Error (%)	OASPL (dB)	Error (dB)
Analytical	100.006	–	86.886	–
FW-H	100.063	0.05	86.863	-0.02

The convergence of radius, time-step and grid is achieved when all these above parameters (both time and frequency domain) have an error of $< 0.5\,\%$ compared to the analytical values (see Appendix A.2). For this case, sphere of radius 0.006 25 m, with 1536 source panels and time step of T/720 predicts the converged solution.

3.5 Stationary dipole

A stationary dipole is modelled as a stationary disc with fluctuating force (F) of absolute magnitude 100 N, applied through a uniform pressure distribution on the surface. This value of force is an arbitrary choice. The code is validated for different positions of the observer in relation to the disc and the applied force to validate the sound directivity of the dipole. The three main configurations tested are as below:
1. Out-of-disc-plane (OD)- disc in the xy plane, force applied in the “z” direction and the far-field stationary observer is located at a distance of 8 m on the axis above the disc plane.
2. In-disc-plane (ID) - disc in the xz plane, force in the “y” direction and the stationary observer is in-plane at a distance of 8 m.
3. On-axis (RD) - disc in the yz plane, force in the “x” direction and the stationary observer is in-plane at a distance of 8 m.

These observer distances are chosen to mimic the model helicopter rotor case presented in Chapter 4. Depending on the location of the observer, some variables in the FW-H code can become zero. In order to validate all the features of the code, observer locations are chosen to have all the variables active and contributing to the acoustic potential. The predicted signal is compared with the analytical solution obtained from Equation 2.8.9. The total acoustic signal for the out-of-disc-plane observer is presented in the Figure 3.5.8. The prediction of the detailed components of the acoustic pressure are presented in Appendix A.3.

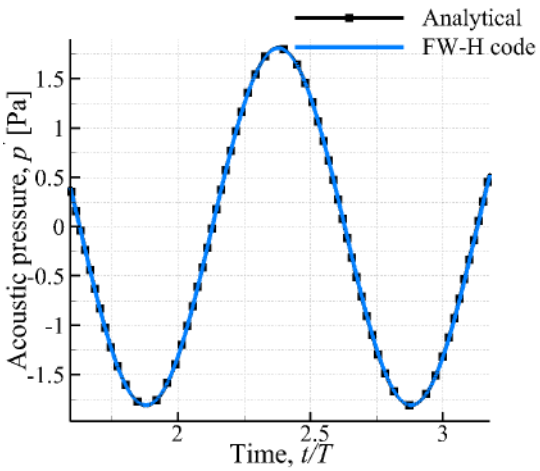

Fig. 3.5.8. Acoustic signal for r = 0.006 25 m, 1280 source cells, $\triangle t$ = T/720 for out-of-disc-plane observer (OD).

For this case, disc of radius 0.006 25 m, with 1280 source panels and time step of T/720 predicts the converged solution (error of $< 0.5\,\%$). For this particular orientation and observer location, the far-field component is predominant compared to the near-field one (see Appendix A.3). There is a good agreement between the predicted and the analytical signals in the time domain. Similar comparison is presented for the in-disc-plane and on-axis observers in Figure 3.5.9 (a) and (b) respectively.

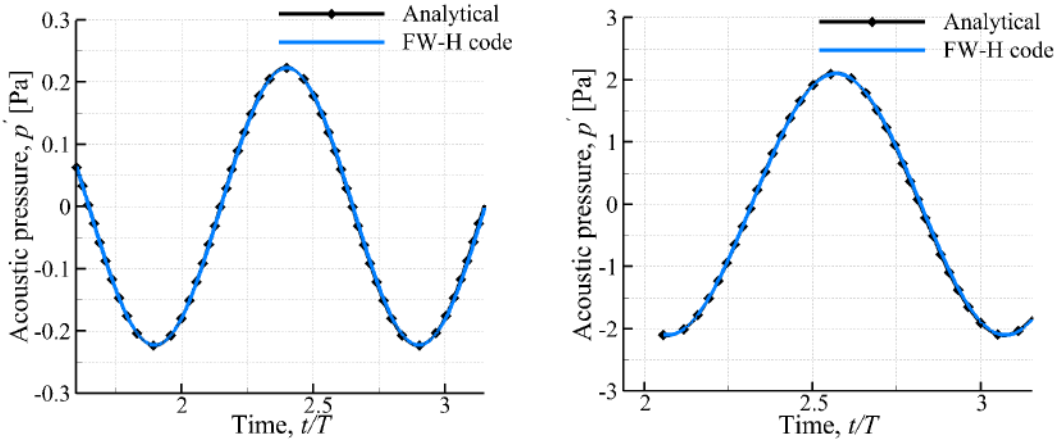

(a) In-disc-plane (ID) (b) On-axis (RD)

Fig. 3.5.9. Total acoustic signal for r = 0.006 25 m, 1445 source cells, $\triangle t$ = T/720.

Both the in-disc-plane and on-axis dipole predictions are also in good agreement with the analytical solutions in both time and frequency (dominant) domains. The total signals along with their components (see Appendix A.3) are captured accurately thus verifying the capabilities of the code to handle different orientations and forces. Frequency and OASPL computed from time and frequency analysis for all the three dipoles are presented in Tables 3.5.1 and 3.5.2.

Tab. 3.5.1. Time domain analysis

		Amplitude (Pa)	Error (%)	P_{rms} (Pa)	Error (%)	OASPL (dB)	Error (dB)
OD	Analytical	1.81	–	1.64	–	96.13	–
	FW-H	1.80	0.16	1.63	0.34	96.12	0.01
ID	Analytical	0.223	–	0.0248	–	77.94	–
	FW-H	0.222	0.17	0.0247	0.44	77.92	0.01
RD	Analytical	2.105	–	2.16	–	97.34	–
	FW-H	2.101	0.16	2.15	0.41	97.29	0.04

Tab. 3.5.2. Frequency domain analysis

		Frequency (Hz)	Error (%)	OASPL (dB)	Error (dB)
OD	Analytical	100.005	–	96.13	–
	FW-H Code	100.045	-0.04	96.11	0.01
ID	Analytical	100.005	–	77.94	–
	FW-H	100.087	-0.08	77.67	0.26
RD	Analytical	100.005	–	97.43	–
	FW-H	100.392	-0.38	97.37	0.06

FW-H predictions are in good agreement with the analytical solutions for all the sound metrics and all configurations. The converged solutions are all within the acceptable error range ($< 0.5\,\%$).

3.6 Rotating source/sink of mass (thickness noise)

The rotating source/sink of mass case is designed specifically to mimic thickness noise pulse (large negative peak surrounded by two smaller positive humps) generation mechanism (monopole) and is described in detail by Schmitz in [69] for a helicopter rotor radiation. The tip of the rotor blade (region that contributes the most to the thickness noise) is modelled as an equivalent body in motion. It consists of two small radii spheres subjected to surface mass transfer and positioned equivalently to leading (source) and trailing (sink) edges of the airfoil (Figure 3.6.10). It is the time delay in receiving the pulses emitted by the source and by the sink at the far-field observer location that is responsible for the the recorded acoustic pressure signal.

Two spheres of the same size are placed at a relative distance equal to the chord length ($c = 0.1\,\mathrm{m}$) of Sargent–Schmitz helicopter rotor blade investigated in Chapter 4. Additionally, the rotation arm ($R = 1\,\mathrm{m}$), the rotation frequency ($f_{rot} = 36\,\mathrm{Hz}$), the ambient conditions of $P_0 = 103\,630\,\mathrm{Pa}$ and $T_0 = 288.15\,\mathrm{K}$ are all replicated. The mass flow rates of the source and of the sink are equal in strength $q = +0.1\,\mathrm{kg/s}$ but opposite in terms of direction (sign). This value of mass flow rate is an arbitrary choice. Since the far-field acoustic signatures are of major concern, a stationary observer is placed at a distance of $8\,\mathrm{m}$ ($8R$) from the centre and in the rotation plane. The FW–H code acoustic prediction is compared with the analytical solution (Equation 2.8.3), first in

terms of the near- and the far-field components (and the total signal) of the source and of the sink separately. Finally, a combined acoustic presure pulse of the rotating source/sink pair is presented (in time and frequency domains) resembling in many details the thickness noise signal shape radiated in-plane by a helicopter rotor blade.

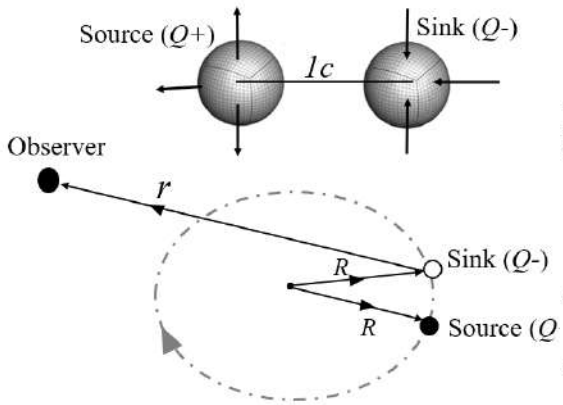

Fig. 3.6.10. Rotating source/sink of mass – model of thickness noise radiation.

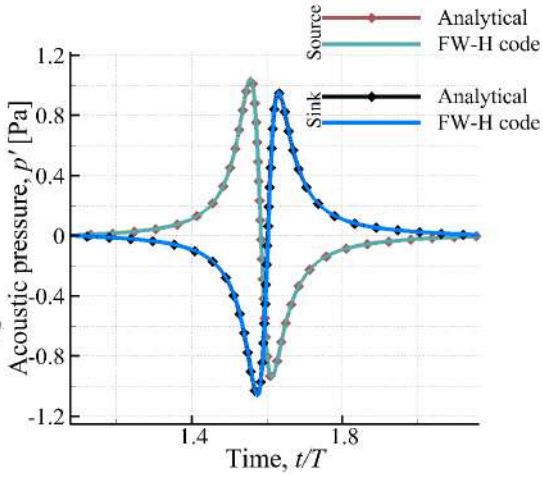

Fig. 3.6.11. Total acoustic pressure (p') signals for a rotating source and a rotating sink.

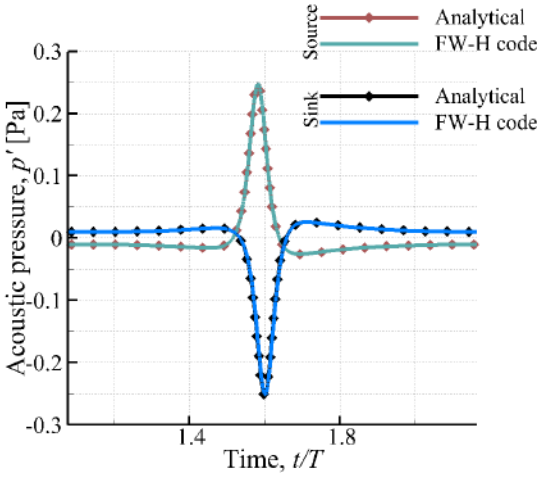

(a) Near-field

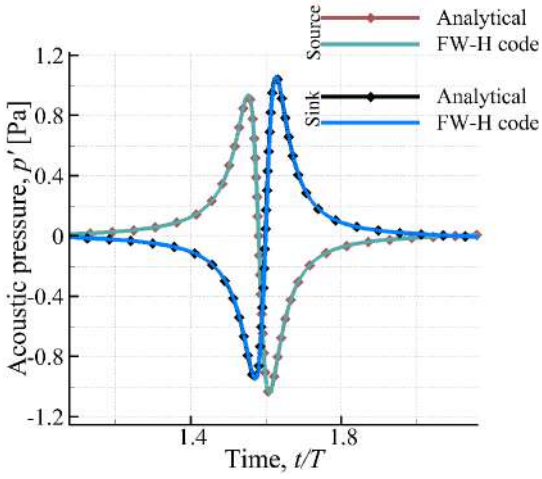

(b) Far-field

Fig. 3.6.12. Acoustic pressure (p') signal components for a rotating source and a rotating sink.

As a result of sphere size, grid, and time-step dependency studies (Appendix A.4), the spheres of radii of 0.006 25 m, the surface grid of 1536 source panels, and the time-step of $T/5760$ ($T = 27$ ms – period of rotation) are chosen for further acoustic analysis. The FW–H solution error is below 0.5% for almost all depicted noise metrics. The

rotating source and the rotating sink acoustic pressure signals are of opposite nature (and slightly delayed in relation to each other), i.e. the source emits a positive peak followed by a negative peak, while the sink radiates the inverse pattern (Figure 3.6.11). For the chosen in-plane observer location, the far-field component of the acoustic pulse is predominant over the near-field one (Figure 3.6.12). The evident shift in the observer time for both acoustic sources prevents the two signals from cancelling out each other completely (which is exactly the case for an observer located on the rotation axis) [155]. The FW–H code predictions of the total acoustic signal, split into near-field and far-field terms, are in good agreement with the analytical solutions (Figures 3.6.11, 3.6.12).

The acoustic signals emitted by the source and by the sink are then linearly summed up at the correct observer time to obtain the combined noise pulse shape (Figure 3.6.13). For an in-plane observer location, due to the existence of the time delay between the maximum acoustic emission of the source and of the sink (separated in space), the resultant pulse width is very narrow and constitutes only a fraction of the rotation period T (approximately 2.25 ms, i.e. 30° of rotation). The basic characteristics of this signal are similar to the thickness noise that is generated as a consequence of the displacement of mass of fluid by the movement of rotating bodies in space (e.g. propeller or helicopter rotor blades). Because the ambient conditions (and speed of sound) are considered as constant, the radiation mechanism of the symmetrical negative peak followed by two smaller positive humps is governed mainly by the projection of the normal velocity v_n at each acoustic panel on the radiation vector connecting the source and the observer r (integrated over the source area). Here, the v_n velocity consists of two separate components, i.e. due to surface rotation and mass transfer. The FW–H code prediction of the combined acoustic signal of source-sink pair is also in good agreement with the analytical solution for both, the time (Figure 3.6.13a) and the frequency (Figure 3.6.13b) domains. As expected, the acoustic spectra are dominated by low frequencies (maximum at approx. 250 Hz), with significant emission taking place in the bass and midrange bands (up to 1kHz).

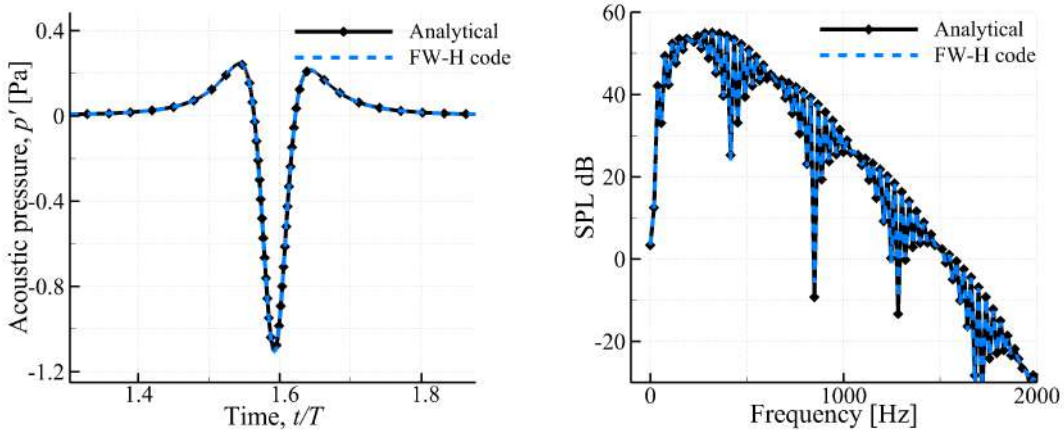

(a) Time domain (b) Frequency domain

Fig. 3.6.13. Total acoustic pressure emitted by the addition of rotating source-sink pair.

A quantitative analysis of the FW–H code accuracy in relation to the analytical solutions is presented in Tables 3.6.1 and 3.6.2. The amplitude (1 Pa), the root-mean-square of pressure fluctuations P_{rms} (0.3 Pa), the frequency of the first harmonic (36 Hz) and the OASPL (84 dB) of separate source and sink signals are practically equal. When both sources are radiating (source and sink), a partial cancellation effect takes place, i.e. OASPL is reduced by 5 dB. It is important to note that 6 dB difference in OASPL signifies two times lower P_{rms}. Due to the thickness noise generation mechanism, the combined (source+sink) pulse shape analysis is very sensitive to the time-step size choice, therefore is more difficult to predict. Still, the relative error for all presented cases and parameters is below 0.7%, which validates the FW–H code functionality in terms of the monopole radiation. Moreover, an important verification is that the OASPL values computed from time signals (P_{rms}) and obtained by integration of SPL spectra are equal within 0.3 dB accuracy.

Tab. 3.6.1. Time domain analysis for a rotating source, sink and a source-sink pair.

		Amplitude (Pa)	Error (%)	P_{rms} (Pa)	Error (%)	OASPL (dB)	Error (dB)
Source	Analytical	1.046	–	0.313	–	83.879	–
	FW–H	1.045	0.095	0.312	0.102	83.870	0.009
Sink	Analytical	0.955	–	0.316	–	83.966	–
	FW–H	0.954	0.094	0.315	0.151	83.957	0.009
Source + Sink	Analytical	-1.100	–	0.1767	–	78.920	–
	FW–H	-1.108	-0.699	0.1767	0.005	79.072	-0.152

Tab. 3.6.2. Frequency domain analysis for a rotating source, sink and source-sink pair.

		Frequency (Hz)	Error (%)	OASPL (dB)	Error (dB)
Source	Analytical	36.082	–	83.87	–
	FW–H Code	36.083	-0.002	83.65	0.22
Sink	Analytical	36.081	–	83.83	–
	FW–H Code	36.083	-0.005	83.74	0.09
Source + Sink	Analytical	37.47	–	78.71	–
	FW–H Code	37.48	-0.026	78.77	-0.06

3.7 Rotating dipole (loading noise)

The rotating dipole case is designed specifically to mimic loading noise generation mechanism for rotors (eg: helicopter, wind turbine). Again, the tip of the rotor blade (the most efficient source of loading noise) is modelled as an equivalent body in motion. It consists of a small radius disc subjected to a force of constant magnitude (out-of-plane/in-plane/radial) and positioned at the quarter chord of the airfoil (Figure 3.7.14). The magnitude of the force (100 N) is assured by proper surface pressure distribution (uniform), while the force direction is always perpendicular to the rotating disk. For the out-of-plane force acting on a rotating body, the disc is kept parallel to the rotation

plane (XY) and the force components (0,0,100 N) do not change in time. The value of the force is an arbitrary choice. This set-up is analogous to the thrust (axial) force acting on the rotor blades. However, for the rotating in-plane and radial force cases, the disc orientation and the force direction are varying in time, although the force magnitude remains constant.

For a helicopter rotor the in-plane force is responsible for the shaft torque generation. Replicating the same input values as in the helicopter rotor case, the rotation arm is R = 1 m, with $f_{rot} = 36$ Hz, $P_0 = 101\,325$ Pa and $T_0 = 288$ K. Since the far-field acoustic signatures are of major concern, stationary observers are placed 8 m above the rotation plane (1,0,8) for the out-of-plane case, and 8 m from the rotation centre (8,0,0) for both the in-plane and radial force cases. The origin of the coordinate system is at the centre of rotation. Although the rotating radial force case has insignificant acoustic contribution specifically for rotor bodies presented in Chapters 4 and 5, it is presented here to depict a full matrix of validation cases.

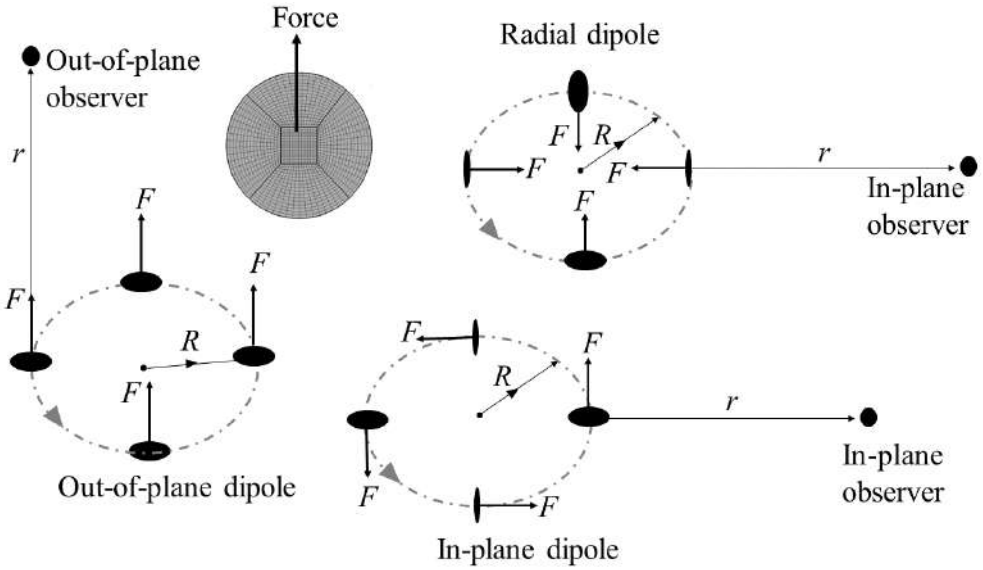

Fig. 3.7.14. Rotating force – representative model of loading (dipole) noise radiation.

As a result of disc size, grid, and time-step dependency studies (Appendix A.5), the disc radius of 0.006 25 m, the surface grid of 1280 source panels, and the time-step of $T/720$ ($T = 27$ ms – period of rotation) are chosen for further acoustic analysis. The FW–H solution error is below 0.5% for all depicted noise metrics (amplitude, P_{rms}, frequency, and OASPL). However, for improved comparison of the SPL spectra with analytical solutions and for consistency with the monopole radiation model case, a much finer time-step of $T/5760$ is assumed for all subsequent plots. The FW–H code acoustic prediction is compared with the analytical solution (Equation 2.8.8).

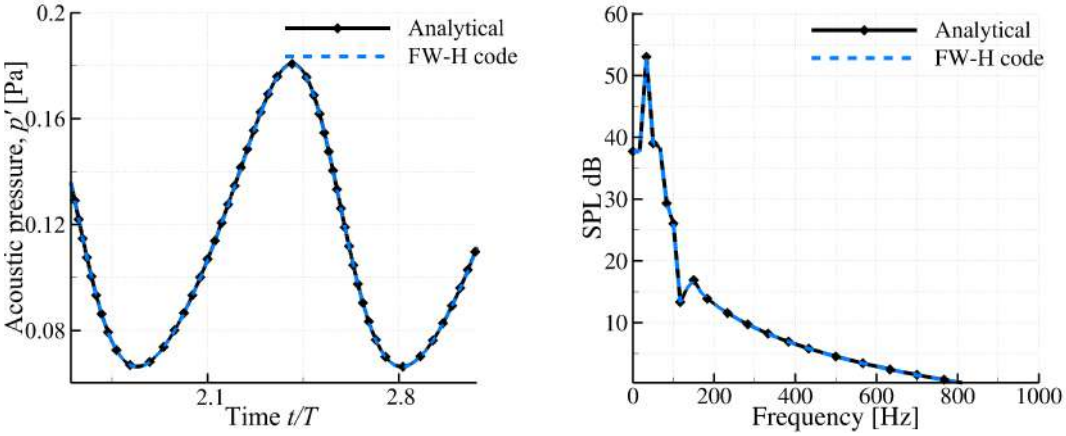

(a) Time domain (b) Frequency domain

Fig. 3.7.15. Acoustic pressure (p') signal and SPL for a rotating out-of-plane force.

The FW–H code predictions of the total acoustic signal (Figure 3.7.15a) and its components (see Appendix A.5) are in good agreement with the analytical solutions in both time and frequency domains.

The total acoustic pressure pulse comparison for the rotating in-plane and radial forces are presented in Figures 3.7.16 and 3.7.17 respectively. Again, the FW–H code prediction is in satisfactory agreement with the analytical solution, both qualitatively and quantitatively, for time (Figures 3.7.16a and 3.7.17a) and spectral (Figures 3.7.16b and 3.7.17b) analysis. The detailed component wise comparison are presented in Appendix A.5. Despite the equal force magnitude (100 N), rotation arm (1 m), and frequency (36 Hz) and similar distance between the rotation centre and the observer location, the amplitude of the signal emitted due to the in-plane force is much higher than due to the out-of-plane force. Such feature is not only a consequence of the force vector acting in the direction tangent to the rotation plane (therefore its components significantly varying in time), but also of the in-plane observer position (maximum acoustic radiation). As expected, the acoustic spectra are dominated by low frequencies (maximum at approx. 100 Hz), with significant emission taking place in the bass and midrange bands (up to 1 kHz). As will be presented in Chapter 4, apart from the dominating thickness (monopole) component, both the out-of-plane and the in-plane forces acting on the rotor blades do contribute to the final amplitude and shape of the acoustic signal of the LF-IPH noise for helicopter rotors (high-speed subsonic applications). On the contrary, for the noise prediction of the wind turbine rotors (see Chapter 5), the rotating forces are the dominant noise sources that govern the nature of the total acoustic signal against the insignificant thickness noise (low-speed applications).

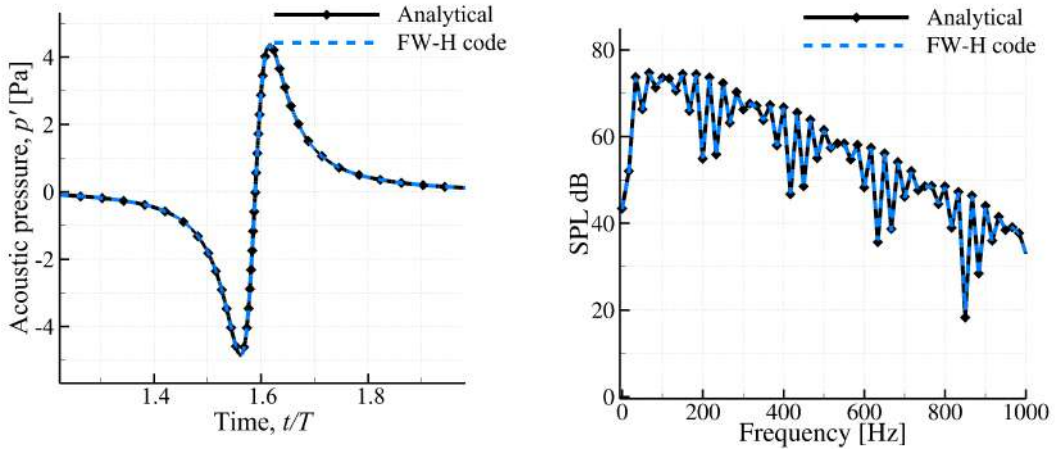

(a) Time domain (b) Frequency domain

Fig. 3.7.16. Acoustic pressure (p') signal components and SPL for a rotating in-plane force.

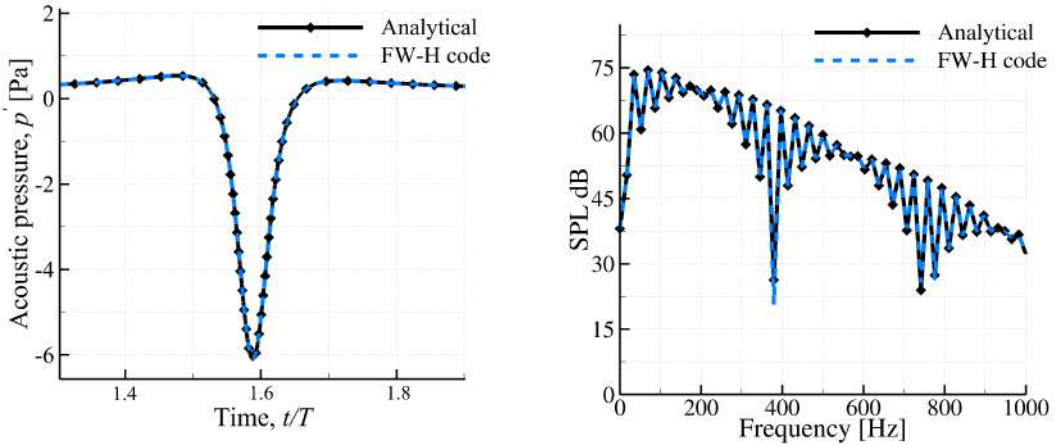

(a) Time domain (b) Frequency domain

Fig. 3.7.17. Acoustic pressure (p') signal components and SPL for a rotating radial force.

A quantitative evaluation of the FW–H code accuracy in relation to the analytical solutions is presented in Tables 3.7.1 and 3.7.2. The amplitude, the P_{rms} and the OASPL differ between the three sources due to their different maximum acoustic radiations positions and directions. Still, the frequencies of the first harmonics are equal (36 Hz). The relative error for all presented cases and depicted parameters is below 0.5% (see Appendix A.5), which validates the FW–H code functionality in terms of the dipole radiation. Moreover, an important verification is that the OASPL values computed from time signals (P_{rms}) and obtained by integration of SPL spectra are within 0.4 dB accuracy.

Tab. 3.7.1. Time domain analysis for a rotating out-of-plane/in-plane/radial forces.

Dipole	Code	Amplitude (Pa)	Error (%)	P_{rms} (Pa)	Error (%)	OASPL (dB)	Error (dB)
Out-of-plane	Analytical	0.1807	–	0.1233	–	75.80	–
	FW–H	0.1804	0.16	0.1229	0.33	75.78	0.02
In-plane	Analytical	4.36	–	1.414	–	96.99	–
	FW–H	4.35	0.22	1.412	0.15	96.98	0.01
Radial	Analytical	-6.10	–	3.139	–	98.947	–
	FW-H	-6.09	0.19	3.138	0.025	98.946	0.001

Tab. 3.7.2. Frequency domain analysis for a rotating out-of-plane/in-plane/radial forces.

Dipole	Code	Frequency (Hz)	Error (%)	OASPL (dB)	Error (dB)
Out-of-plane	Analytical	36.364	–	75.78	–
	FW–H	36.365	-0.002	75.76	0.02
In-plane	Analytical	36.367	–	96.96	–
	FW–H	36.365	0.005	97.00	-0.05
Radial	Analytical	36.365	–	98.26	–
	FW-H	36.367	-0.002	98.40	-0.14

3.8 Summary

The successful implementation of the aeroacoustic code based on the FW–H analogy is presented in this chapter. A thorough validation of the code for the two main types of noise - thickness and loading noise mechanisms have been presented. This was achieved through comparison of the acoustic signal predicted by the code with the analytical solutions of the elementary sources - monopole and dipole. Validation has been presented for four main configurations - stationary monopole/dipole and rotating monopole/dipole. The rotating pair of monopoles (source-sink pair) mimics the mechanism of thickness noise while the rotating source of momentum (dipole) mimics the loading noise. Comparison of the acoustic pressure in both time and frequency domain along with the various sound metrics such as root-mean-square pressure, SPL, OASPL have been presented for all the cases. The FW–H code prediction is in good agreement with the analytical solution ($< 0.5\%$ relative error) both qualitatively and quantitatively for all the various configurations considered. The functionality of the code for handling various noise generation mechanisms has been thoroughly validated. The flexibility of the code in analyzing different orientations of the loading force has also been established.

Additionally, numerical codes based on the analytical solutions for the fundamental sound sources - monopole and dipole were implemented for validation purposes. Four analytical codes for the individual elementary sources - stationary and rotating monopole and dipole have been implemented. Two more codes for distributed sources - the rotating monopole and dipole codes (point sources) have been extended to have a distribution of sources to closely relate to mechanisms of thickness and loading noise

respectively. These computationally inexpensive analytical codes can also be used for preliminary analysis that aid efficient design in new projects.

Thus, the implemented aeroacoustic code based on FW–H analogy has been tested for simple sound sources in this chapter and it's application to complex bodies is presented in the next chapter.

Chapter 4

Aeroacoustic analysis of an helicopter rotor in hover

The developed FW–H code is employed for the acoustic investigation of a model helicopter rotor in hover (subsonic motion) in this chapter[2]. In this case, the low-frequency harmonic noise (LF-IPH) radiated by the rotor consists of two main noise mechanisms - thickness and loading [156]. The quadrupole source term is insignificant at this particular Mach number (0.661), hence, neglected [157].

The Sargent-Schmitz (S–S) single-bladed model rotor is acoustically analyzed for a chosen microphone (M1, located at 2.40 R from the rotation axis and 1.63 c above the rotor plane) and compared component wise with the reference code and the total acoustic signal with the measurements (University of Maryland) [157]. For thickness noise calculation, the blade surface grid is extracted directly from the 3D CFD model, with its each cell constituting a separate acoustic source panel. The input for the loading noise is obtained from two methods - the quick and simple BEMT method and from the computationally expensive but detailed CFD/RANS (FLOWer solver) conducted by Oskar Szulc, published in Suresh et al. [150].

The same BEMT method (identical input parameters and blade/time disretizations of 95 radial sections and time-step of $T/360$) from the reference literature code [157] is also employed here to facilitate a direct one-on-one comparison. BEMT is a hybrid method, combining the blade element and the momentum theories, that is designed for rotary wing analysis [153]. It is able to predict rotor loading, depending on: the number of blades, the blade radius and shape, the operating conditions, and the induced inflow model (non-uniform inflow with Prandtl tip-loss function). The sectional lift c_l and drag c_d coefficients are assumed to be known though, e.g. from a separate 2d analysis (experimental or numerical). As a result the rotor thrust c_t and torque c_q coefficients as well as the blade radial distribution of in-plane and out-of-plane components of the aerodynamic force are obtained, which may be directly used as input to the FW–H solver for acoustic predictions of rotor loading noise. The compact chord form of this loading is applied at $0.25\,c$ along the blade span. The simplest approach is to assume that the lift curve slope is equal to $c_{l\alpha} = 2\pi$ and the drag coefficient is constant regardless of the angle of attack α (e.g. $c_d = c_{d0} = 0.015$), as in [157].

The experimental model rotor consists of one untwisted, untapered and rigid blade (and a counter-weight) having rectangular planform and NACA 0012 symmetrical cross-section [157]. The computational model however consists of 2 blades and an artificial

[2]Some parts of the text in this chapter have been published in Archives of Mechanics [150].

hub surface [150]. Single-bladed rotor systems are rarely exploited for computation, they are meant for experimental research. For both rotor designs (1- and 2-bladed) the radiated thickness noise and loading noise due to in-plane forces are the same. However, due to the increased induced inflow velocity, the 2-bladed rotor exhibits 30% lower blade loading (out-of-plane force) compared to the original design. For the in-plane microphone location (M1) the acoustic consequences of the associated rotor thrust reduction are of ternary importance only and will be quantified (by BEMT) and discussed in more details in section 4.2.

Keeping the aspect ratio constant ($AR = 9.75$), the geometry is up-scaled to chord length $c = 1$ (radius $R = 9.75$). The radius of the artificial hub is $0.5\,c$, while the inner part of the blade is removed and the blade root is located at $1.0\,c$. The blade trailing edge is sharp (zero thickness) and the pitch axis is set to $0.25\,c$. The computational domain consists of 160 blocks and block-structured C–H–H grid ($11.39 \cdot 10^6$ of control volumes). The rotor dimensions and operating conditions are summarized in Table 4.0.1.

Parameter	Experimental model	CFD model
rotor radius, R $[m]$	0.9906	9.75
blade chord length, c $[m]$	0.1016	1.0
rotor aspect ratio, AR	9.75	9.75
blade collective angle, θ $[^\circ]$	2.0	2.0
ambient pressure, P_0 $[Pa]$	101325	10530
ambient temperature, T_0 $[K]$	288.15	288.15
ambient density, ρ_0 $[kg/m^3]$	1.22	0.127
ambient viscosity, μ_0 $[Pa \cdot s]$	$1.79 \cdot 10^{-5}$	$1.79 \cdot 10^{-5}$
ambient speed of sound, c_0 $[m/s]$	340.3	340.3
rotational speed, RPM	2169	220.3
tip Mach number, M_T	0.661	0.661
tip Reynolds number, Re_T	$1.6 \cdot 10^6$	$1.6 \cdot 10^6$
tip velocity, V_T $[m/s]$	225.0	225.0
frequency of rotation, f_{rot} $[Hz]$	36.14	3.672
period of rotation, T $[ms]$	27.7	272

Tab. 4.0.1. S–S model rotor dimensions and operating conditions [150].

A comparison of the aerodynamic performance (c_t and c_q) predicted by both CFD (FLOWer/LEA $k - \Omega$) and by BEMT methods show that the basic variant of BEMT method ($c_{l\alpha} = 2\pi$ and $c_d = c_{d0} = 0.015$ [153]) applied in the acoustic research of Sargent and Schmitz [157], delivers only a crude approximation of the forces acting on the rotor blades. The resultant BEMT and CFD loadings are fed as input to the FW–H code to predict loading noise. Detailed description of the computational model and analysis is presented in Suresh et al. [150].

4.1 Thickness and loading noise prediction

A detailed comparison of the FW–H code predictions with the reference code solutions [157] is presented in the following sections. For the thickness noise radiation, spa-

tial and temporal discretization dependency studies are conducted using coarse (2016 elements), medium (6864 elements), and fine (25200 elements) grids, as well as coarse ($T/360$), medium ($T/720$), and fine ($T/1440$) time-steps. The fine grid (25200) and fine time-step ($T/1440$) is selected for all subsequent thickness noise predictions due to improved amplitude and phase of the resultant signal. However, because of the unknown experimental ambient conditions, the temperature is calibrated first and fixed at $T_0 = 286\,\mathrm{K}$ to match the phase of the main pressure pulse (dependence of speed of sound on temperature). Next, the pressure is set to $P_0 = 106500\,\mathrm{Pa}$ to improve the peak amplitude. The alteration of T_0 and P_0 only slightly affects the phase and peak amplitude, the basic shape of the pulse is retained [158]. The total thickness signal is depicted in Figure 4.1.1a along with its near- and far-field components. The resultant spanwise distribution of the aerodynamic forces from BEMT is imported to the FW–H code using the compact chord assumption (forces at $0.25c$ along the blade span). The total loading signal is presented along with its components in Figure 4.1.1b for both the FW–H and the reference code.

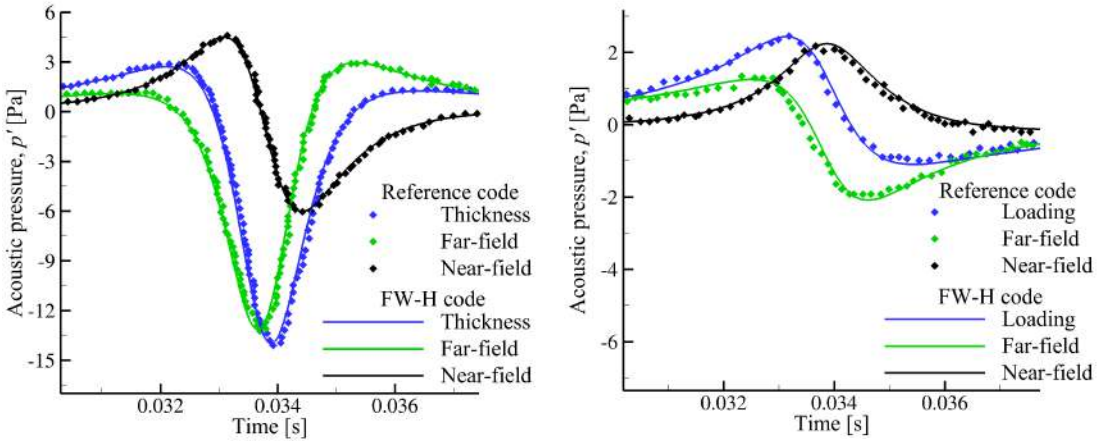

(a) Thickness noise (b) Loading noise

Fig. 4.1.1. Comparison of FW–H code acoustic signal components prediction with reference code [157].

The thickness noise is generated due to the chordwise distribution of elementary sources and sinks which emit pressure signals of opposite nature that are received by the observer at different times (as described in section 3.6). Due to this phase mismatch, a characteristic symmetrical large negative pressure pulse surrounded by two smaller positive humps is radiated [69]. The rotating blade spanwise distribution of the aerodynamic forces (mainly in-plane and out-of-plane components) generate loading noise. Due to the near-field observer location, the near- and far-field components are together significant for both, thickness and loading noise emission. However, the far-field one is predominant for the total acoustic signal shape. The contribution of loading noise to the total acoustic signal is small compared to the thickness noise for this particular microphone location (in-plane). The FW–H acoustic code predictions are in satisfactory agreement both qualitatively and quantitatively with the reference code solutions (near-/far-field/total and thickness/loading components).

4.2 Loading noise prediction

Further validation of the loading noise prediction by the code is presented against the analytical solutions (Figure 4.2.2). The analytical solution for the rotor blade is obtained from the distributed sources code for loading noise (explained in detail in section 3.2.3). The acoustic pressure is obtained by linear summation of all the distributed elementary dipole solutions (Equation 2.8.8) along the rotating blade radius at the quarter-chord (compact chord assumption) location. Aerodynamic forces (both out-of-plane and in-plane forces) are computed with the BEMT method (95 radial sections) and imported both to the FW–H and analytical codes for acoustic post-processing. Moreover, the FW–H solutions (near-field and far-field) are not only compared with the analytical solutions, but also with the reference signal [157]. For the near in-plane microphone M1 location, both in-plane (torque generation) and out-of-plane (thrust generation) forces contribute to the total loading noise signature. The radial (spanwise) forces are not considered here as they are of ternary importance in predicting LF-IPH noise.

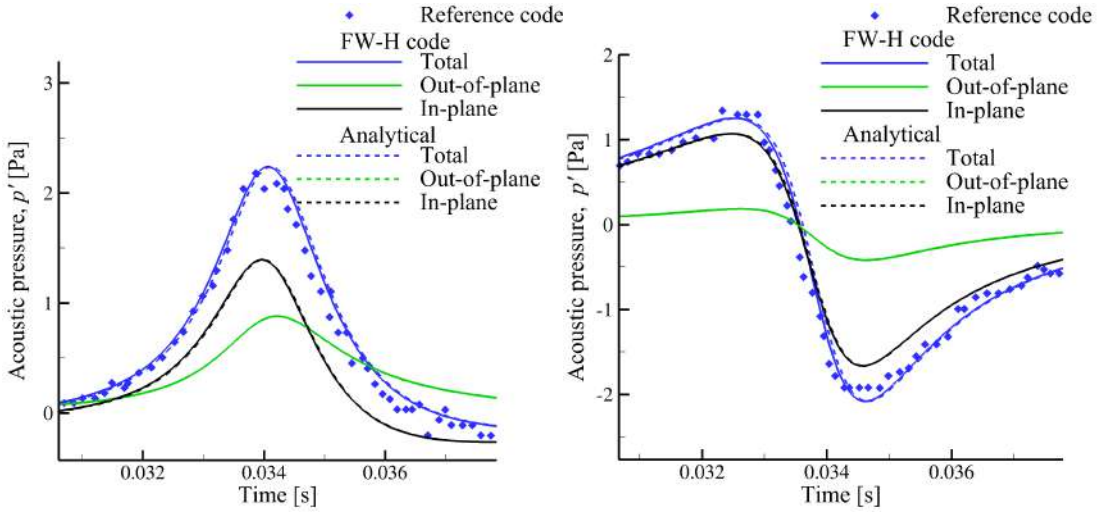

(a) Near-field (b) Far-field

Fig. 4.2.2. The FW–H and analytical code loading noise predictions against reference code [157].

For the near-field component (Figure 4.2.2a), both the in-plane and out-of-plane forces contribute similarly to the total acoustic signal. However, the in-plane force contribution is predominant over the out-of-plane force contribution (3 times higher amplitude) for the far-field component (Figure 4.2.2b). Since the acoustic pressures signals generated by both the forces are similar, their linear summation leads to a constructive effect (increase of amplitude) for near- and far-field noise components. It is important to note that the out-of-plane (thrust) force contribution to the loading noise is significant particularly because of the near-field observer location and may not be noticeable in the acoustic far-field. The FW–H code predictions are equivalent to the analytical solutions for both the components thus the resultant pressure signals (summation of in-plane and out-of-plane forces) are also in good agreement with the

reference data.

For the comparison of the total loading noise against experimental data, a 2-bladed CFD model is implemented. The impact of this choice is acoustically quantified in many details in Figure 4.2.3 against the reference code data. Such a detailed comparison of 1 blade v/s 2 blades is conducted through the loadings obtained from BEMT analysis since the CFD analysis was performed for only 2-bladed rotor. The analytical code results are in good agreement with the FW–H analysis at a fraction of the computational cost.

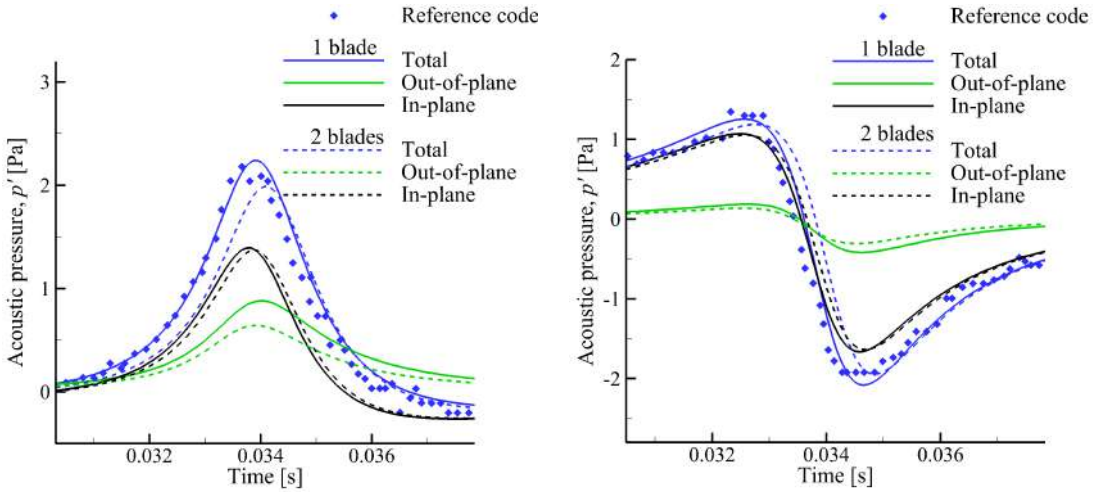

(a) Near-field (b) Far-field

Fig. 4.2.3. Analytical code predictions of loading noise components for 1- and 2-bladed rotors.

Both the 1- and 2-bladed rotors emit loading noise and its components that are similar in shape. Still, the 11% (near-field) and 6% (far-field) differences in peak amplitude are present that are accompanied by a slight phase shift between both solutions and the reference data. This deviation is attributed mainly to the variability in the acoustic emission due to the out-of-plane force. The 2-bladed rotor generates higher thrust compared to the 1-bladed design when operating conditions are fixed. It results in increased downwash (induced velocity) and therefore leads to the reduction of the effective angle of attack of each blade section. Hence, the reduced loading (per blade) and lower associated loading noise levels are observed. Since the c_d is almost constant for near-zero inflow angles, the blade sectional in-plane force distribution is not significantly affected by the number of blades and thus the related acoustic emission of both configurations is almost identical. The LF-IPH noise pulse consists primarily of the thickness noise with a secondary contribution of the steady loading noise (Figure 4.1.1). The rotor loading noise due to the in-plane force (torque generating) is not affected by the computational model choice (1- or 2-bladed). However, the quantified difference in out-of-plane (thrust generating) force distributions has only a ternary importance for in-plane acoustic emission and is neglected.

4.3 Total noise prediction

The total acoustic pressure signals obtained from linear summation of thickness noise (p_T) and loading noise (p_L) at correct observer time are compared against the reference solution (blue diamonds) and the experimental data (red triangles) in Figure 4.3.4a. The total signal is characterized by a large negative pressure pulse surrounded by two smaller positive humps (asymmetric), similar to the dominating thickness component shape (for subsonic tip speeds and near in-plane observer locations). The loading noise predictions of FW–H code based on both source generation methods BEMT (green line) and CFD (black line) are added together with thickness noise to obtain total signals (marked as BEMT + FW–H and CFD + FW–H). The loading noise not only slightly alters the positive humps (located before and after the main event), but also decreases the peak amplitude of the negative pulse.

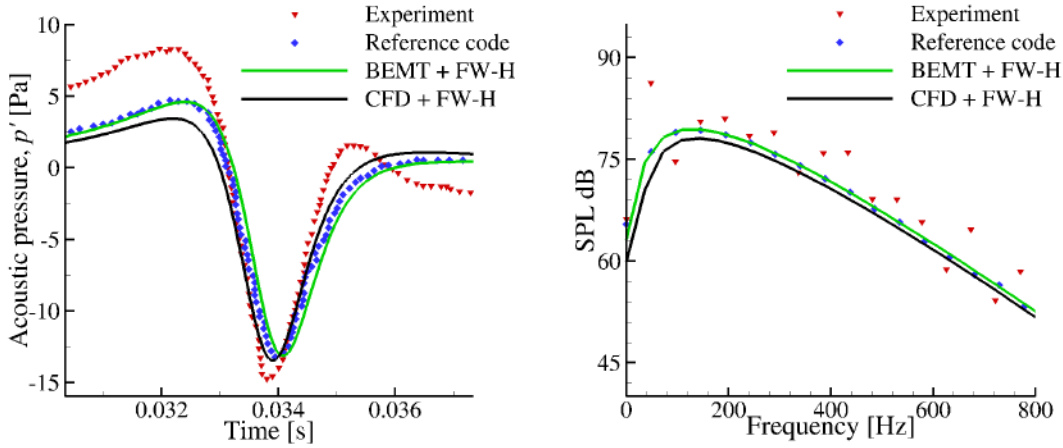

(a) Time domain (b) Frequency domain

Fig. 4.3.4. Total acoustic signal analysis for Sargent–Schmitz rotor.

In the time domain, the width and negative peak-amplitude of the BEMT + FW–H total acoustic signal is matching the reference code prediction well. However, there is a small phase shift between both solutions (approx. equal to 0.7% of the time period), possibly due to tiny misalignments of loading and thickness (near- and far-field) components and the reference data (noticeable in Figure 4.1.1). It is important to keep in mind that exactly the same methodology (BEMT, 95 radial sections) is used for both loading noise predictions (reference and BEMT + FW–H), but the presented thickness noise analysis is based on the CFD grid of much higher resolution compared to the surface discretization used in [157]. The calculated total acoustic signals based on BEMT (BEMT + FW–H) and CFD (CFD + FW–H) blade loadings are similar in terms of the negative peak-amplitude. However, apart from a different phase (by approx. 0.3 ms), the leading, rising edge positive peak is reduced (by approx. 1 Pa) between BEMT + FW–H and CFD + FW–H solutions. At the same time, the right hand side positive peak is increased by a similar value (approx. 1 Pa). The origin of this difference is primarily significant overprediction of the blade loading by basic BEMT method [150]. Moreover, the two-bladed CFD model exhibits lower out-of-plane

component of the aerodynamic force (and of the associated loading noise) compared to the single-bladed design (see Figure 4.2.3). In terms of the main negative LF-IPH pulse, the CFD + FW–H approach somewhat improves the peak amplitude and phase compared to the experimental data, while becoming slightly less consistent with the reference and BEMT + FW–H signals.

It is important to note that in contrast to the theoretical data of Figure 4.3.4 (reference and in-house FW–H code predictions), the experimental data is subjected to significant low-frequency acoustic reflections that affect the investigated noise signature. University of Maryland Acoustic Chamber (UMAC) is a small facility devoted to helicopter rotor acoustic investigations [157]. The testing space is covered by acoustic wedges with strategic placement of additional absorbing material at key reflection surfaces. Moreover, the choice of a single-bladed rotor and microphones placement are key features allowing for separation of the main pulse from the reflected signatures thus enabling quantitative LF-IPH noise measurements. Even though the waveform shape is highly affected before and after the negative peak, the time history reflections are separated from the main pulse of interest. Still, the peak amplitude of the negative pulse is slightly underpredicted by both BEMT + FW–H (10%) and CFD + FW–H (9%) analysis compared to the experimental points and in-line with the reference code result (9%).

The SPL spectra are presented in Figure 4.3.4b for the lowest 20 rotor harmonics (up to 800 Hz). All signals are dominated by low frequencies, with maxima present at approx. 150 Hz. Only low frequency range is presented here since the sound emitted at these frequencies travel long distances leading to rotor detection and public annoyance. Due to presence of acoustic reflections not only the experimental SPL curve (red triangles) reveals wavy character and is shifted upwards, but it also exhibits a dominating low-frequency component (2^{nd} harmonic) not present in the theoretical solutions. Still, the BEMT + FW–H (green line) and CFD + FW–H (black line) modelling results satisfactorily match the reference spectrum (blue diamonds).

The overall sound pressure levels calculated for all depicted cases are summarized in Table 4.3.1. The presented values (OASPL from P_{rms}) for the reference code and the experiment are derived based on time domain signals extracted from figures presented in [157] and may constitute only an approximation of the measured data. Due to presence of significant wall reflections in UMAC, the experimental OASPL (106.4 dB) is underpredicted by 2.6 dB–4.4 dB for the reference (103.8 dB), BEMT + FW–H (103.6 dB), and CFD + FW–H (102 dB) signals. However, the difference in OASPL between both theoretical approaches and the reference code is equal to 0.2 dB (BEMT + FW–H) and 1.7 dB (CFD + FW–H). The integration of the SPL spectra of Figure 4.3.4b results in OASPL values (OASPL from SPL) differing by less than 0.5 dB compared to the time-domain analysis (OASPL from P_{rms}).

Tab. 4.3.1. Overall sound pressure level (OASPL) comparison.

	OASPL from P_{rms} (dB)	OASPL from SPL (dB)
Experiment [157]	106.4	106.7
Reference code [157]	103.8	103.3
BEMT + FW–H	103.6	103.4
CFD + FW–H	102.1	102.1

4.4 Summary

The developed acoustic code is used to predict Low-Frequency In-Plane Harmonic (LF-IPH) noise of a model helicopter rotor of Sargent and Schmitz in low-thrust hover conditions that is compared with available experimental data and reference code solutions from University of Maryland. Two methods of blade surface loading estimation were utilized – BEMT and CFD. The BEMT + FW–H solution (compact chord assumption) proves to be equivalent to the reference code estimation in terms of near- and far-field terms. Moreover, the contribution of the in-plane (torque) and out-of-plane (thrust) forces to loading noise (near- and far-field terms) is quantified. For an almost in-plane microphone location, the signal's peak amplitude is dominated by the thickness component, with secondary contributions from the in-plane and out-of-plane forces. The CFD analysis is conducted using the available 2-bladed computational model (experimental rotor is 1-bladed). The difference in induced inflow velocity for both configurations affects slightly the lower, out-of-plane (thrust) component of the blade sectional force only and is noticeable mainly in the near-field term (reduced significance while moving towards the acoustic far-field). Therefore, for a near-zero blade pitch setting (low-thrust), the acoustic consequences of this assumption are of ternary importance. Finally, the BEMT + FW–H loading noise prediction is compared with analytical solutions (rotating spanwise distribution of point sources of momentum).

The computed (BEMT + FW–H) total noise signature (thickness and loading) is in satisfactory agreement with the reference code data both qualitatively and quantitatively (near- and far-field terms). However, lower blade loading predicted by CFD impacts the comparison with the reference signal (based on BEMT), therefore the CFD + FW–H acoustic solution is also affected. Analyzed total acoustic signals compare well in terms of the main pulse width and shape with the experimental data. The underprediction in the peak negative amplitude and in the OASPL is attributed to low-frequency reflections present in the acoustic chamber that are not modeled by FW–H analogy.

The relative ease of direct application of the code to existing CFD results and the flexibility in its use, allow it to be utilized for various rotating (open space) configurations particularly, the helicopter rotor is demonstrated successfully in this chapter. Although it is not presented in this work, one of the methods to decrease the LF-IPH noise of helicopter rotors is the intensive surface ventilation (suction and blowing of air) at the blade tip [159] known as the Thickness Noise Control (TNC). The validated FW–H code can be utilized to analyze the sound directivity and efficiency of the TNC noise mitigation method.

Chapter 5

Impact of RVGs on rotational noise of a wind turbine rotor

Acoustic investigation of thickness noise which is predominant in helicopters has been presented in the previous chapter. In the following chapters, investigation of loading noise which is dominant in wind turbine rotor blades/airfoil will be presented. Specifically, analysis of impact of a chosen flow control device (rod type vortex generators) on the rotational noise (current chapter) and broadband noise (next chapter) will be presented. Only steady rotational noise analysis can be performed due to the availability (within the Aerodynamics Department) of only steady pressure data (from CFD) for the wind turbine blades.

The acoustic investigation of the rod vortex generators implemented on the NREL Phase VI wind turbine is presented in this chapter. The impact of the RVGs - additional surfaces sticking out of the blades, on the thickness and steady loading noise for the wind energy application is analyzed. This particular wind turbine is chosen since a detailed aerodynamic analysis (numerical) has been presented by Suarez et al. [26, 27] and the surface pressure data is available within the research group. The same grid discretization and topology utilized in the numerical flow analysis along with the pressure distribution are given as input to the aeroacoustic code.

5.1 Wind turbine configuration

The validation of the numerical set-up is performed against the measurement data from the sequence S campaign of the Phase VI Unsteady Aerodynamics Experiment of NREL [160] by Suarez et al. [26]. Measurements on the rotor with two linearly tapered, non-linearly twisted blades of radius $R = 5.029\,\mathrm{m}$ were conducted inside the $24.4\,\mathrm{m}\times36.6\,\mathrm{m}$ wind tunnel at NASA Ames Research centre.

The numerical model employed has been validated by Suarez for the reference rotor blades (without RVGs) with the experimental data. The numerical set-up consists of a half-cylindrical computational domain of radius $3R$ for a single blade located at the centre of the domain. The structured grid for the reference rotor blade (without RVGs) consists of 8.8 million control volumes distributed into 76 blocks. The grid is of C-type in the chordwise and H-type in the spanwise and freestream directions. The blade surface is defined by 289×89 nodes in the wrap around and spanwise directions respectively. The nondimensional distance ($y+$) of the first mesh layer near the blade wall is of the order of 1. Reynolds-averaged Navier-Stokes (RANS) simulations were performed for both the reference rotor blades and the blades equipped with RVGs using

a finite volume, density based, block-structured Fine/Turbo solver from Numeca (now Cadence). Although various turbulent models were tested against the experiments, the results obtained from the 2-equation explicit algebraic Reynolds stress model (EARSM) have been utilized for the present acoustic analysis.

The validated model has been employed to study the effect of the flow control for the blades with wind speed of 10 m/s. A row of 10 RVGs are implemented at discrete spanwise locations (Figure 5.1.1), from r/R = 0.738 to 0.775, covering a 3.7% of blade radius and at mid-chord [26]. These rods are designed based on the mid-chord boundary layer thickness at reference section ($r/R = 0.75$). The boundary layer thickness at this location is approximately equal to $\delta_{ref} = 0.024\, c_{ref}$. Hence, the orientation and dimensions are: $\phi = 30^o$, $\theta = 45^o$, $D = 0.2\, \delta_{ref}$, $h = 0.5\, \delta_{ref}$ with ϕ being the pitch angle, θ is the skew angle, D and h are the diameter and height of the rods respectively.

The grid of the reference rotor blades is used with only the region close to the rods altered. The grid is refined in the proximities and downstream of the RVGs. A single RVG computational slice includes 19 blocks and is defined by 253 $\times$ 33 nodes in the chordwise and spanwise directions, respectively. The total mesh consists of 27.4×10^6 number of volume cells per blade distributed among 282 blocks. The grid topology around each rod is presented in the right side of Figure 5.1.1. The base of each rod consists of four blocks while the rod is characterised by a five block butterfly topology. This grid topology (along with its discretization) is provided as input to the aeroacoustic code.

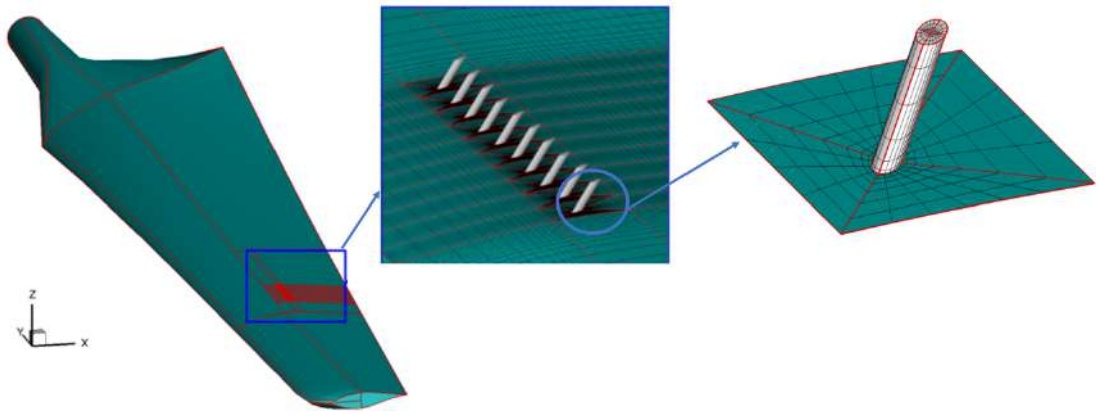

Fig. 5.1.1. NREL Phase VI rotor blade with surface discretization (coarse discretization for visual representation) around the RVGs [26].

The rotor at wind speed of 10 m/s is particularly chosen for the acoustic investigation because the turbulent separation exists on the suction side, nearly, along the entire span (until $r/R = 0.95$). Results show the reduction of the separation volume by the rods leading to a 0.54% increase in torque and a 0.67% increase in thrust. More detailed comparison on the aerodynamic performance is available in Suarez et al. [26].

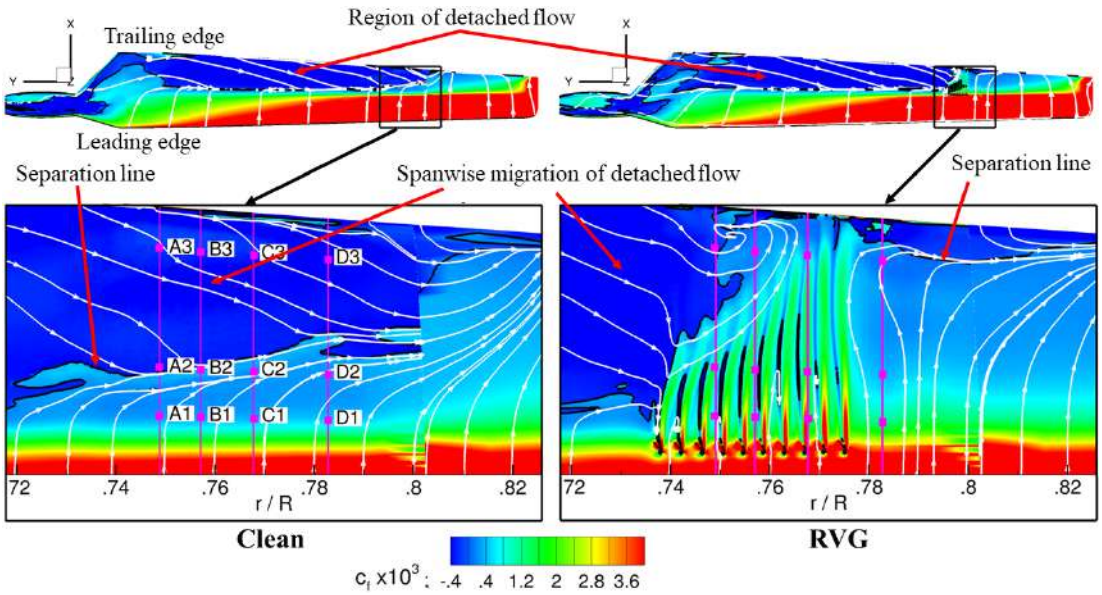

Fig. 5.1.2. Contour maps of skin friction coefficient and flow streamlines for NREL Phase VI wind turbine [26].

5.2 Acoustic analysis

The surface pressure distribution from the validated simulation data at wind speed of 10 m/s along with the blade discretization (mesh) and kinematics are provided as input to the FW–H acoustic code for analysis. Each mesh cell used for the RANS simulations acts as an acoustic source panel for which the aeroacoustic code computes the acoustic potential at emission time. The potential for all the source panels are then linearly added at appropriate listener time to obtain the final acoustic pressure signals. Steady RANS simulations were conducted and the resulting steady pressure distribution is utilized in the acoustic investigation. Thus, steady rotational noise comprising of thickness noise and loading noise is presented in the following sections. To include unsteady loading noise analysis, either pressure data from LES simulations where all the flow characteristics are resolved or from measurements is required for the rotor blades. Since such data is not available within the research group, an alternative approach to assess the impact of rods on the broadband noise is presented in the section 6.5.

To assess the acoustic directivity of RVGs, pressure signals at different microphone locations are analyzed and presented. The acoustic investigation is conducted for both the reference rotor blades and the blades with RVGs, at three observer locations including in-plane and out-of-plane microphones. Both time and frequency domain analysis are conducted. The pressure distribution obtained from the steady simulations along with the grid is re-scaled back from the numerical $c = 1$ m to the experimental chord of 0.482 m and fed as input to the aeroacoustic code. Convergence studies for the space discretization using coarse (2877 mesh cells), medium (9715 mesh cells) and fine (35716 mesh cells) grids are performed for the reference rotor blade. Similarly, discretization of time-step is conducted for $T/90$, $T/180$ and $T/360$ time-steps. The solutions are considered converged when the relative error (difference between the current solution

and the fine grid, fine time-step solution) is below 0.5% for the selected sound metrics. Only the fine grid and fine time-step solutions are utilized for further analysis. The three microphone locations utilized in the analysis are characterised by M1 (0, -H, 0), M2 (0, -R, H) and M3 (0, -H, H) where, H = 12.2 m (height of the wind turbine), R = 5.022 m and the ground at the in-plane location is given by (0, -H, 0), see Figure 5.2.3. A comparitive analysis between the reference and flow controlled rotor blades are presented in each of the following analysis. All the signals presented below are without the constant shift known as the DC shift by experimentalists (mean amplitude of the waveform) [126] and hence, vary around the ambient pressure (0 value in the figures). This is achieved by subtracting the mean values from each signal (see Appendix B).

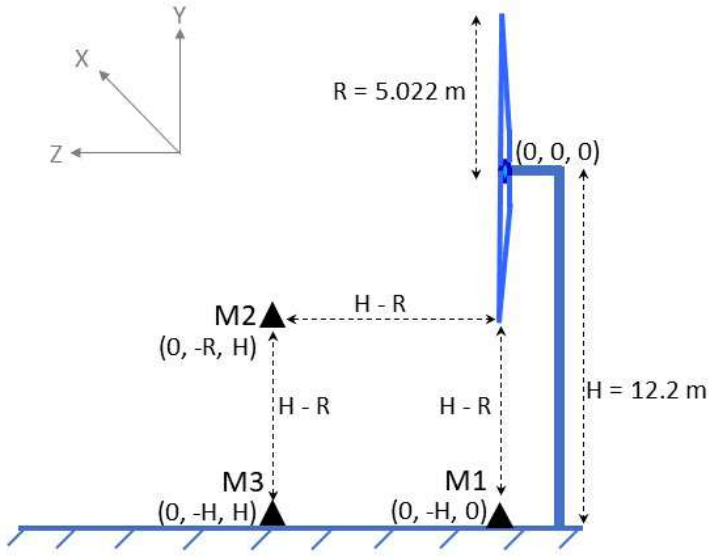

Fig. 5.2.3. Location of microphones.

5.2.1 Thickness and loading noise prediction

In this section the components of the acoustic pressure signal along with their near- and far-field terms (Equations 2.6.15 and 2.6.16) are presented in detail in the time domain. The signals for two microphones - one in-plane (M1) and one out-of-plane (M2), are analyzed. Firstly, the total thickness and loading noise for both the reference rotor blades and the blades with RVGs are presented in Figure 5.2.4. Results show that the loading noise is significantly higher than the thickness noise - $\sim$ 6.8 times higher for M1 and $\sim$ 11.7 times for M2, which is not surprising. Even for the in-plane microphone, the thickness noise is very low due to the low speed of the rotor blades. The signals from the blades with RVGs (green and teal coloured lines) overlap with the reference signals indicating almost no significant difference between them for both the microphone locations. The total magnitude of the signals for the in-plane microphone is one order of magnitude higher than that of the out-of-plane microphone.

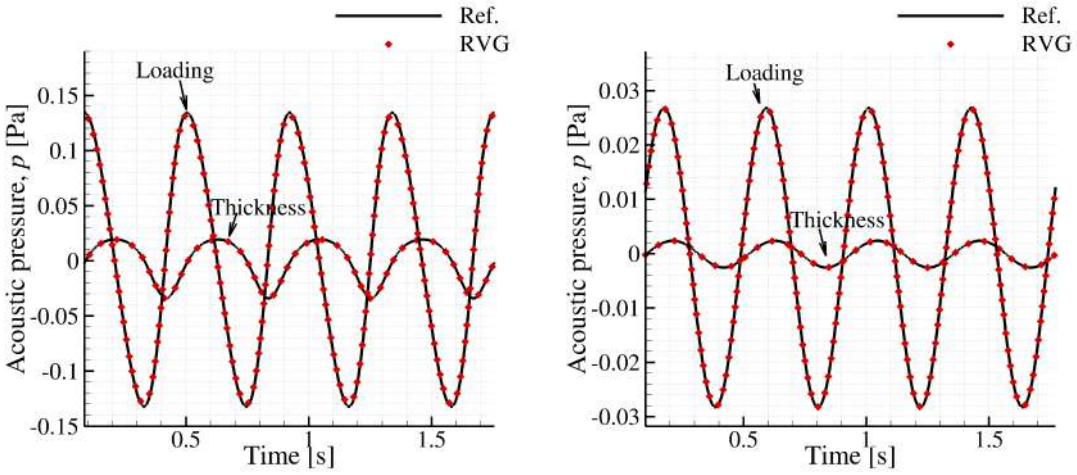

(a) In-plane microphone (M1) (b) Out-of-plane microphone (M2)

Fig. 5.2.4. Comparison of components of the acoustic pressure signal for selected microphones.

Further analysis into the contribution of the near- and far-field terms to both thickness and loading noise are presented in Figures 5.2.5 and 5.2.6 respectively. For both thickness and loading noise, the near-field terms are dominant over the far-field terms irrespective of the microphone locations. Additionally, the nature and shape of the components of the pressure signal for both the microphones are also similar. For almost all the components except for the loading near-field term of the in-plane microphone M1 (Figure 5.2.6(a)), the signals from the RVGs case match with the reference blade signals. There is a small difference in the loading near-field signals between the RVGs and the reference case (not visible to eye). The impact of this deviation will be discussed in the next section 5.2.2.

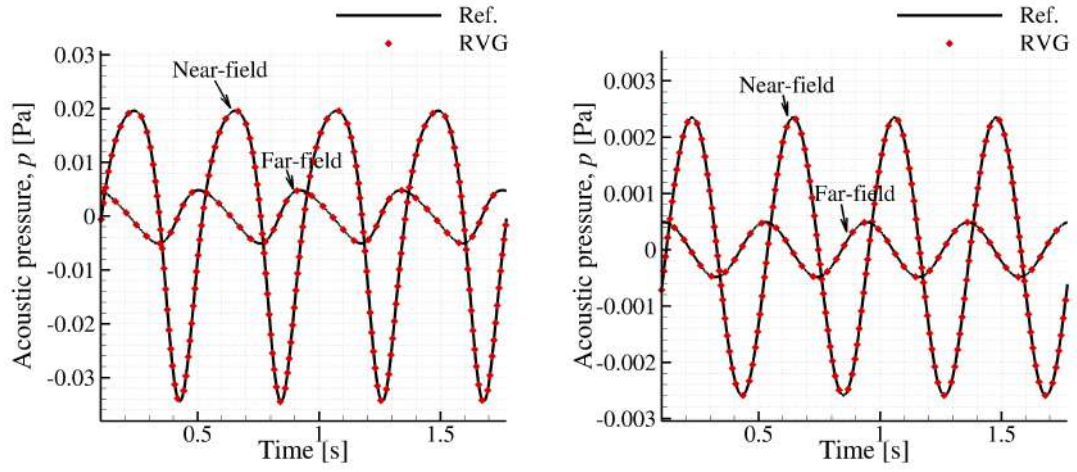

(a) In-plane microphone (M1) (b) Out-of-plane microphone (M2)

Fig. 5.2.5. Comparison of thickness noise components for selected microphones.

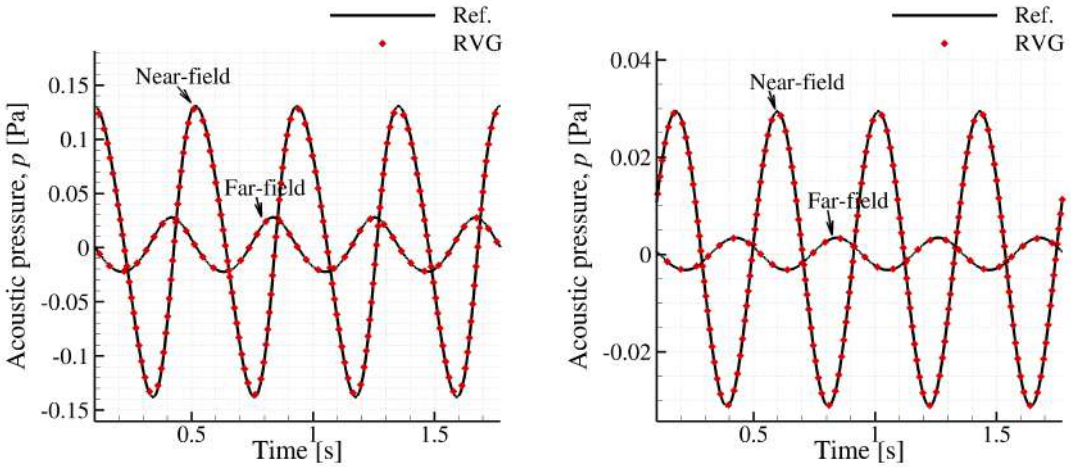

(a) In-plane microphone (M1) (b) Out-of-plane microphone (M2)

Fig. 5.2.6. Comparison of loading noise components for selected microphones.

5.2.2 Total noise prediction

The total acoustic pressure (thickness + loading) for in-plane (M1) and out-of-plane microphones (M2, M3) are presented in time and frequency domain in Figures 5.2.7 (a) and 5.2.8 (a) respectively. On the right hand side of these figures a comparison of the in-plane and out-of-plane microphones on the ground are presented (Figures 5.2.7 (b) and 5.2.8 (b)). The peak amplitude of the pressure signals is more for the in-plane microphone (M1) when compared to the out-of-plane microphones. The shape and trends of the signals are however similar. The overall sound pressure levels are also higher for the in-plane microphone.

The sound levels at the ground level (i.e. M1 v/s M3) are analyzed since it is of importance to residents living near wind turbines. The strength of the pressure signals heard by observers away from the wind turbine (M3) is much lower than the listener close to the tower (M1) $\sim$ 3.7 times lower peak amplitude. This is clearly visible in the pressure and SPL plots below.

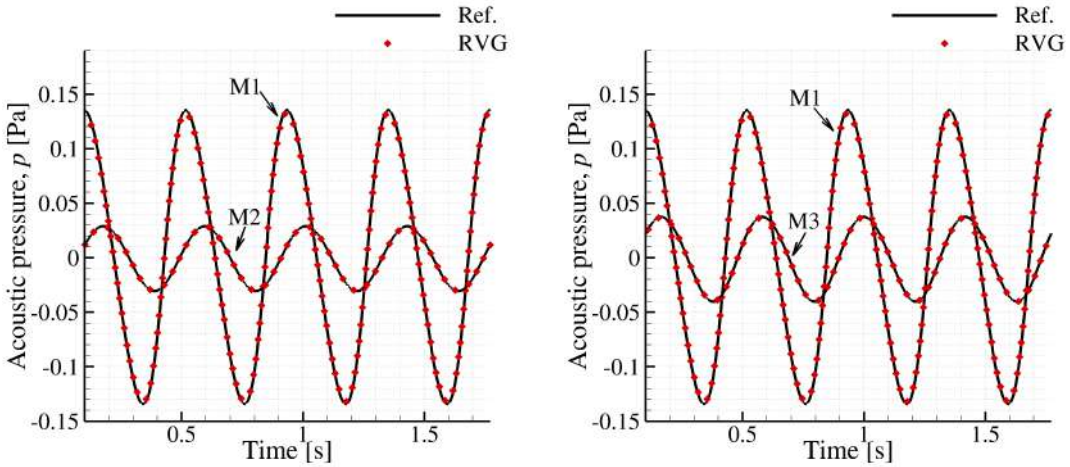

(a) M1 v/s M2 (b) M1 v/s M3

Fig. 5.2.7. Total acoustic pressure signal for selected microphones in time domain.

The influence of RVGs on the global/total acoustic pressure signals appears almost negligible from the current analysis. In these plots the curves for flow controlled case overlap with the reference rotor blades in both time and frequency domain as well as for all microphones. There is a very slight deviation (between Ref and RVGs) noticeable only in the observer M1 location in the time domain (Figure 5.2.8 (a)). RVGs decrease the sound levels slightly for the in-plane microphone. This reduction is quantified in the OASPL Table 5.2.1. The three resolved harmonics in case of M1 and and the two harmonics for M2 and M3, all occur at very low frequencies below 20 Hz, which is out of the human audible range. However, these low frequency sound waves travel longer distances and may affect some animals and hence is an important factor for wind farms.

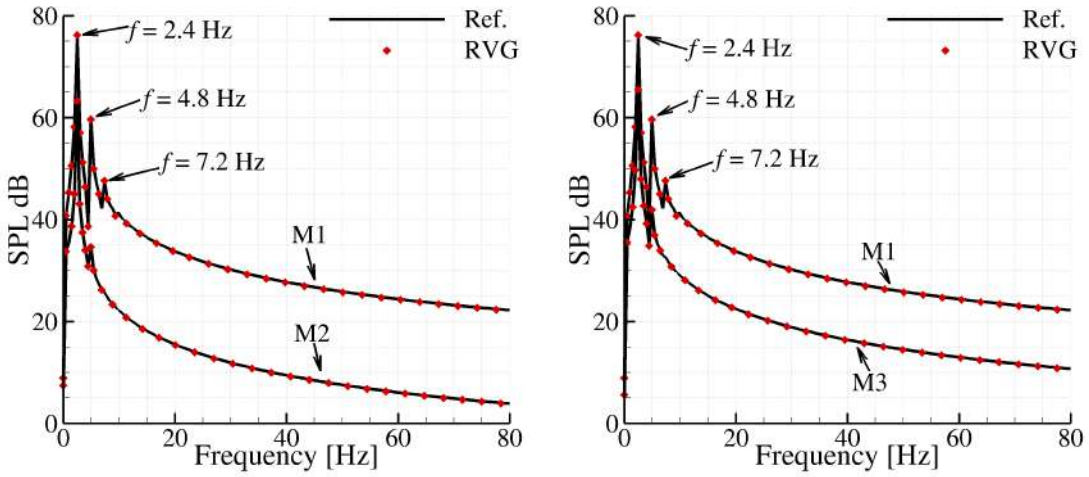

(a) M1 v/s M2 (b) M1 v/s M3

Fig. 5.2.8. Total acoustic pressure signal for selected microphones in frequency domain.

The quantification of the sound levels (OASPL) for different microphones obtained from both time (P_{rms}) and frequency domain (SPL) are presented in Table 5.2.1 along with their difference (Δ = OASPL$_{RVGs}$ - OASPL$_{Ref.}$). The in-plane observer emits the loudest sound level (73 dB) compared to the out-of-plane listeners. Even though the out-of-plane microphones are placed at the same distance from the rotor tower, the ground level observer (M3) emits higher sound ($\sim$ 2.36 dB) than the observer in front of the rotor hub. This is due to the directivity of the emitted sound by the rotor blades. There is no influence of the RVGs on the overall sound pressure levels for the out-of-plane microphones ($\Delta < 0.06$ dB). RVGs decrease the sound only slightly $\sim$ 0.16 dB, when compared to the reference case for the in-plane microphone. The sound levels predicted from both P_{rms} and SPL for all the microphones are comparable to each other.

Tab. 5.2.1. Overall sound pressure level (OASPL) predictions.

	OASPL from P_{rms}			OASPL from SPL		
Microphone	Ref. (dB)	RVGs (dB)	Δ (dB)	Ref. (dB)	RVGs (dB)	Δ (dB)
M1	73.52	73.36	-0.16	73.56	73.41	-0.15
M2	60.42	60.39	-0.03	60.41	60.38	-0.03
M3	62.76	62.71	-0.05	62.77	62.71	-0.06

5.2.3 Region wise comparison

Since influence of the RVGs on the acoustics is barely visible in the pressure signals of the complete rotor with two blades, local variations are analyzed by predicting the pressure signals emitted by certain sections of a single blade. Two of the most important sections - the tip region near the trailing edge (Region 1) from $r/R = 0.79$

to $r/R = 1$ and the region where the RVGs are implemented (Region 2) given by $r/R = 0.63$ to $r/R = 0.79$ (Figure 5.2.9) are presented in this section. These regions are chosen approximately from mid-span to the trailing edge. In order to analyze the maximum local differences between the reference and the flow controlled case, these specific small areas where the alteration in flow structures (due to streamwise vortices by the rods), observed from the aerodynamic analysis (Figure 5.1.2) are chosen. The thickness and loading noise components from these two regions for the reference rotor blade are compared with the blade with RVGs in the time domain (Figure 5.2.10). To emphasize, the below presented signals are local values and are not the total signals emitted by the blade.

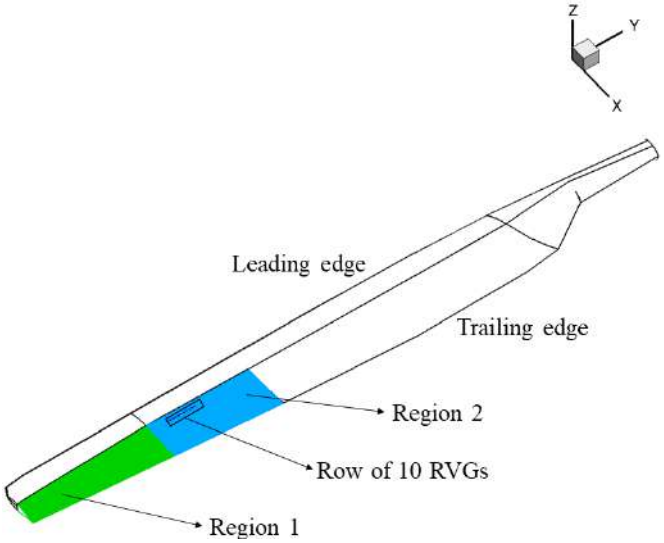

Fig. 5.2.9. Selected regions of analysis of the NREL Phase VI rotor with RVGs.

Analysis of the region-wise comparison of the pressure signal components is conducted below. There is a slight variation (equal to one line width in the plots) for the loading noise in region 1. RVGs reduce loading noise when compared to the reference blade near the trailing edge tip region. The contribution to thickness noise from both the regions are almost similar, whereas the region where the RVGs are located contribute slightly more than the tip area to loading noise. Also to note that in this comparison, the magnitude of the thickness noise is much higher than the loading noise which is the opposite nature to the total signals presented in Figures 5.2.5 and 5.2.6. This is because, globally, for the entire blade, the thickness noise gets cancelled out due to destructive interference caused by the other parts of the blade and hence the total signal exhibits a different nature than what is observed in this local small region prediction. The influence of a constructive interference can be noticed for the thickness noise presented by the curve obtained by adding the signals from regions 1 and 2 (Figure 5.2.10 (a)). Since the signals from both the regions have the same sign, they add up to have a large magnitude. On the contrary, for the loading noise the signals from the regions have opposite nature (sign), thus, leading to a destructive interference and a resulting signal with lower magnitude (Figure 5.2.10 (b)).

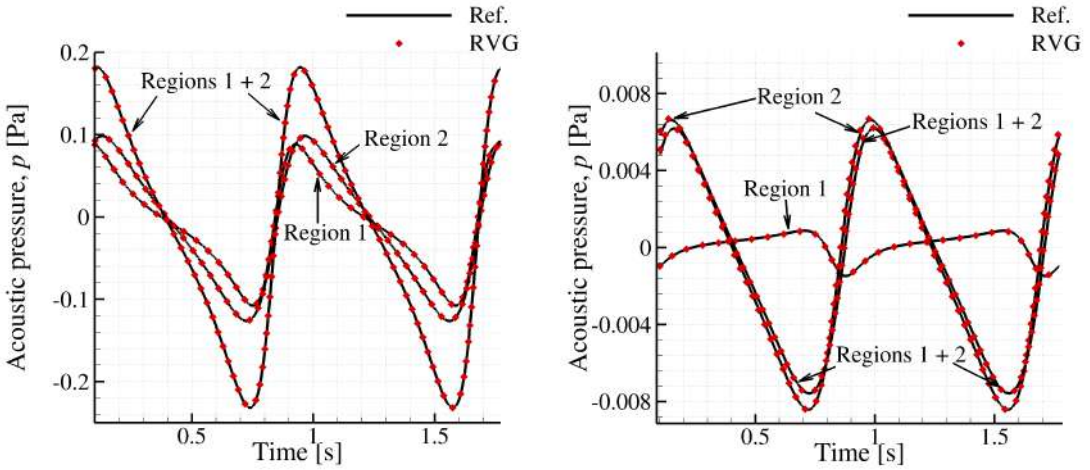

(a) Thickness (b) Loading

Fig. 5.2.10. Region-wise acoustic pressure signal components for M1 microphone.

The difference in the nature of sound emitted by the flow controlled and reference blades are quantified in Table 5.2.2 through the sound metrics from time domain. For the thickness noise, RVGs decrease the emitted noise by very small values. For both the regions there is no significant difference in the thickness noise metrics between the two cases. There is a small reduction ($\sim$ 0.1 dB) by the RVGs in the loading noise emitted by region 1 (tip) compared to an increase ($\sim$ 0.01 dB) at region 2 (RVGs). The influence of constructive/destructive interference is also noticeable in the overall sound levels. The thickness noise has a higher sound levels ($\sim$ 76 dB) for the signal from both the regions than the individual regions while the loading noise emitted from both the regions is lower ($\sim$ 47 dB) than the noise emitted by region 2 ($\sim$ 48 dB). There is no significant variation even in the local pressure signal predictions due to the RVGs. Even though the rods exert a positive influence on the flow by reducing turbulent boundary layer separation presented in the above Figure 5.1.2, there is no significant additional impact on the sound emitted by the rotor blades. Hence, the rods satisfy the dual requirements of reducing flow separation without adding any meaningful acoustic penalty.

Tab. 5.2.2. Comparison of sound metrics in time domain for M1 microphone.

		OASPL		
Noise	Region	Reference (dB)	RVGs (dB)	Δ(RVGs - Ref.) (dB)
Thickness	Reg 1	69.29	69.20	-0.09
	Reg 2	71.41	71.39	-0.02
	Regs 1 + 2	76.18	76.17	-0.01
Loading	Reg 1	30.49	30.39	-0.1
	Reg 2	48.13	48.14	0.01
	Regs 1 + 2	47.22	47.22	0

5.3 Summary

The acoustic analysis performed on both the reference blades and the blades with RVGs exhibit similar behaviour and similar peak values. Both the time and frequency domain analysis presents no significant difference between the sound pressure levels (steady rotational noise) emitted by the rotor with/without the RVGs. The relative difference ($SPL_{RVGs} - SPL_{Ref.}$) in the overall sound pressure levels emitted by the rotor blades is negligible for this particular configuration i.e. $\Delta < 0.1$ dB. Thus, there is no negative acoustic impact of the rods for this particular NREL Phase VI rotor blades equipped with 10 RVGs in terms of rotational noise, while it improves aerodynamic performance by reducing separation. These findings are in alignment with another study in literature, where, vane type vortex generators were analyzed for the NREL wind turbine [161], which also found that the vortex generators have trivial effect on the overall sound emission and directivity while improving aerodynamic performance. It is important to note that the RVGs are implemented only at a fraction of the span (3.7%) and not all the sources of sound are included. In order to supplement to these findings and to simplify the various complex noise sources, the impact of RVGs focussed on the separation noise and the broadband trailing edge noise emitted by a wind turbine airfoil is presented in the next chapter.

Chapter 6

Impact of RVGs on broadband noise of a wind turbine airfoil

The impact of the flow control devices on the steady rotational noise has been analyzed utilizing the validated aeroacoustic FW–H code in the previous chapter. To investigate the influence of the RVGs specifically on the broadband noise, measurements for a wind turbine airfoil is conducted. An experimental campaign to study the impact of Rod Vortex Generators (RVGs) on the flow and acoustic characteristics of a wind turbine airfoil (DU96-W-180) is conducted at the A-tunnel (Figure 6.0.1) in the Low Speed Laboratories of Delft University of Technology (TUD). Measurements are performed for the airfoil at a flow velocity of 30 m/s and a range of inflow angles ($-4°$ to $20°$). Turbulent flow separation close to the trailing edge is observed at higher inflow angles. To mitigate this separation, RVGs are implemented. Measurements are conducted in the anechoic, vertical, open-jet wind tunnel in the Low Speed Laboratories at TUD. The set-up consists of a rectangular test section of dimensions 0.4 m × 0.7 m and contraction ratio of 15:1 and inlet turbulence intensity of 0.1 %. The airfoil is held between two sideplates of 1.2 m length and is at a distance of 0.5 m from the nozzle exit. The airfoil has a fixed span $s = 0.4$ m.

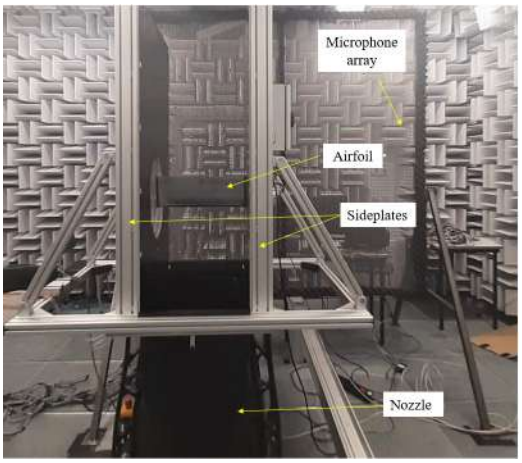

Fig. 6.0.1. Anechoic, vertical open-jet test section at TUD with DU96-W-180 airfoil.

Before manufacturing the airfoil and the RVGs for the measurements (at TUD), their geometric dimensions are determined using numerical simulations. The computational model used in the design process is firstly validated against an existing

experimental campaign that was conducted by Suryadi et al. [162] at the open test section of the acoustic wind tunnel (AWB) at the German Aerospace Centre (DLR), Braunschweig. This particular data is chosen from literature due to the similar open-jet test section configuration and the same DU96-W-180 airfoil. The design methodology utilized is described in detail in the following section. The validated numerical model for the reference airfoil is then extended to include the test section constraints of the TUD A-tunnel where the experimental campaign is conducted. Utilizing the upstream boundary layer characteristics obtained from these numerical simulations, the RVGs are designed and manufactured. The impact of the streamwise vortices generated by the rods on the separation zone, analyzed through various flow measurement techniques such as wall pressure measurement, surface oil flow visualization and particle image velocimetry (PIV) is presented next. Finally, the effect of the rods on noise sources is analyzed through beamforming technique performed on the acoustic measurements obtained from a microphone array.

6.1 Design of the airfoil model for measurements

Measurement data from Suryadi et al. [162] is available for the airfoil (span = 0.8 m, chord = 0.3 m) for a range of angles of attack $-0.8° \leq \alpha \leq 10.3°$ and at three Reynolds numbers (0.8, 1.0 and 1.2 million). Only pressure measurements at Reynolds number of 1.2 million are compared against the numerical data. The boundary layer of the airfoil was tripped using a zig-zag tape (0.205 mm high) at 5% chord from the leading edge on the suction side and another one (0.4 mm high) at 10% chord on the pressure side. Further details of the experimental campaign can be found in Suryadi et al. [162].

The numerical model consists of the airfoil in a structured C-grid (2D freestream configuration) as presented in Figure 6.1.2. The dimensions of the domain are as follows: $9c$ downstream of the foil, $5c$ upstream, top and bottom. The mesh is designed to resolve the turbulent boundary layer down to the wall surface ($y^+ < 1$), uniform distribution of cells around the airfoil with maximum skewness of 0.4.

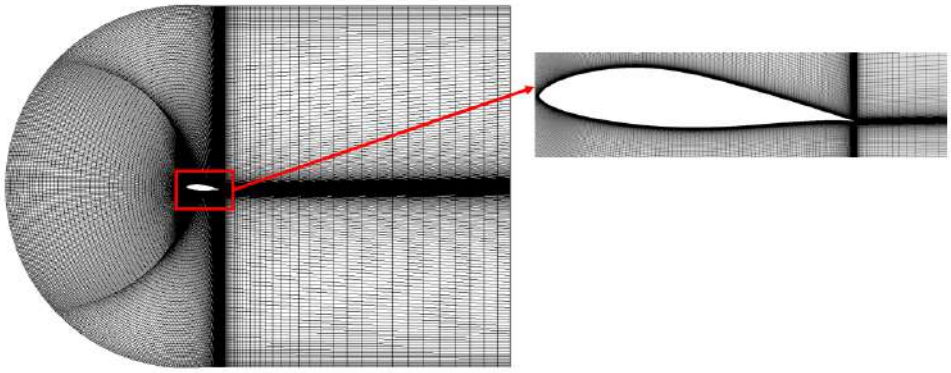

Fig. 6.1.2. Structured C-grid (5 blocks) around DU96-W-180 airfoil.

RANS simulations employing the one-equation Spalart-Allmaras model (SA) [163] model and the Explicit Algebraic Reynolds Stress Model (EARSM) [164] were conducted in Numeca (now Cadence). A velocity inlet of 65 m/s, outlet pressure of 101 325 Pa and the airfoil surface as adiabatic wall (no-slip) boundary conditions are

imposed. A perfect gas model with Sutherland's viscosity law is implemented. Second order numerical schemes with Merkle preconditioning is imposed.

To estimate the numerical uncertainty of the mesh discretization, three grids are created. Refinement of these grids is achieved by uniformly increasing the cell distribution around the airfoil surface. The mesh dependency is conducted using the Grid Convergence Index method (GCI) [165]. Three grids - coarse grid (9240 cells), medium grid (37400 cells) and fine grid (150040 cells) are created. The output lift coefficient (C_l) is monitored. Using GCI method, the approximate relative error (e_a), the extrapolated relative error (e_{ext}) and the GCI are computed for the three grids and presented in table 6.1.1. The GCI value for the fine grid is $< 0.1\%$ indicating that no further refinement from the finest grid is necessary as the fine grid solution is mesh independent.

Tab. 6.1.1. Grid Convergence Index results (U = 65 m/s, $\alpha = 4.6°$)

p_{GCI}	Coarse to Medium	Medium to Fine
$e_a 1$	2.41%	0.34%
e_{ext}	0.40%	0.05%
GCI	0.5%	0.07%

Results obtained from the fine mesh are then analyzed for validating the numerical model. The EARSM turbulent model is employed to obtain pressure distribution at two inflow angles. The pressure coefficient (C_p) distribution at the midspan location is compared with the measured data at inflow angle of $\alpha = 4.6°$ in Figure 6.1.3a. The pressure predicted by the numerical model fits with the experimental data satisfactorily. Further verification at higher inflow angle of $\alpha = 9.4°$ is conducted (Figure 6.1.3b). There is a good prediction on the suction and pressure sides in the region $0.1 < x/c < 0.85$. The disagreements are observed close to the leading edge on the suction side ($0 < x/c < 0.1$), where the flow starts to accelerate and at the trailing edge ($0.9 < x/c < 1$). It is suspected that the flow at this angle of attack is already in the non-linear region experiencing turbulent flow separation. This is verified by plotting the lift coefficient curve.

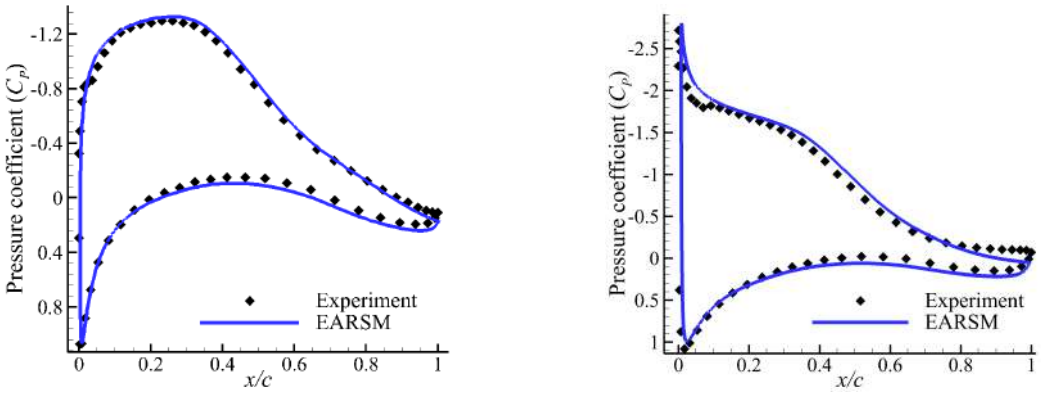

(a) AoA = 4.6° (b) AoA = 9.4°

Fig. 6.1.3. Pressure coefficient (C_p) comparison against measurement data [162] for U = 65 m/s.

The lift coefficient obtained from two turbulent models are compared against measured data as seen in Figure 6.1.4. EARSM model exhibits the closest agreeement with the measurement data at lower angles. It starts to deviate in the non-linear region of the lift curve where separation occurs. This investigation is focussed on the mitigation of the separation zone and the relative difference in the boundary layer characteristics due to the application of the rods. For designing the rods, the upstream boundary layer parameters before the onset of separation, are of primary importance. The prediction of onset of separation is required for designing the geometric parameters of the flow control device while the flow characteristics inside the separation zone (separation size) is of less importance. Hence, the accurate prediction of flow characteristics at higher inflow angles with separation (non-linear region) is not conducted.

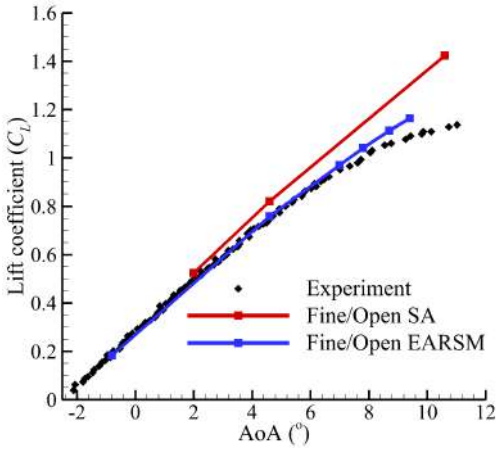

Fig. 6.1.4. Lift coefficient (C_l) comparison against measurement data [162].

This validated numerical model is utilized to design the airfoil with RVGs for the experimental campaign at TUD by further extending the domain to include the test section constraints (Figure 6.0.1). For this particular investigation, aspect ratio of the airfoil to confine with the test section restrictions, the geometric dimensions of the RVGs and the trip-tape (to induce turbulent boundary layer on the airfoil) are to be designed.

The jet nozzle and the side plates that are used for the airfoil installation are included in the computational domain. RANS simulations (EARSM) are conducted for this extended domain (3D) for a range of angles of attack. These 3D simulations (along with the fixed aspect ratio) are required in order to design the rods to investigate turbulent flow separation. Corner vortices at the airfoil mounting on the side plate are observed. With increasing inflow angles, both, the boundary layer flow separation close to the trailing edge and the secondary flow also further develops. The development of the corner vortices at three inflow angles of $10°, 13°$ and $15°$ obtained from the RANS simulations are presented in Figure 6.1.5. These growing corner vortices are strong enough to affect the size of separation at mid-span location. This is unconducive to investigate the impact of RVGs on separation.

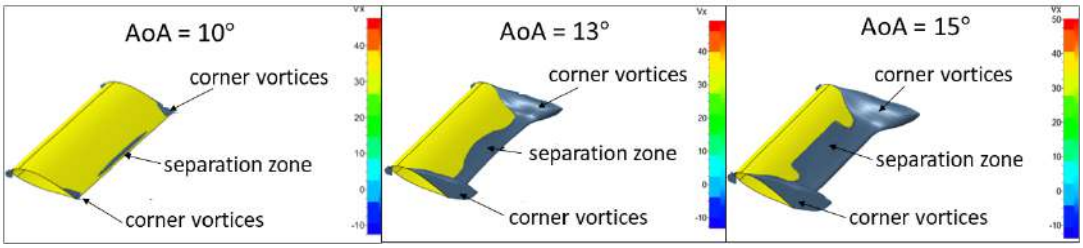

Fig. 6.1.5. Corner vortices on DU96-W-180 airfoil (U = 30 m/s).

To allow for sufficient turbulent separation zone to develop and to mitigate the effect of corner vortices on this zone at midspan, either the aspect ratio has to be increased or the installation of the airfoil on to the sideplates have to be modified (introduce a gap between the sidewall and the airfoil [166]). The fixed test section setup imposes constraints on altering the airfoil mounting. It also imposes a maximum span size limit of 0.4 m. Hence, the chord was varied to achieve a suitable aspect ratio that allows for the flow to develop at the mid-chord without any significant influence by the secondary corner vortices. Collaborative simulations performed within the Aerodynamics Department showed that an aspect ratio of 2.67 ($c = 0.15$ m) allows for the flow development (without significant interference by secondary flows) and also conforms to the test section size limitations. Further investigation into the impact of shear layers (due to installation plates) on the flow characteristics and the effective angle of attack in the test section is presented by Tiwari et. al [167].

6.2 Design of RVGs for measurements

Measurements are conducted for airfoils with natural transition (reference and flow controlled) and airfoils with a zig-zag trip (reference and flow controlled) of 12 mm width and 0.6 mm height placed at 5 % chord from the leading edge on the suction side and at 10 % chord on the pressure side [162]. The airfoil is equipped with an interchangeable insert for RVGs presented in Figure 6.2.6.

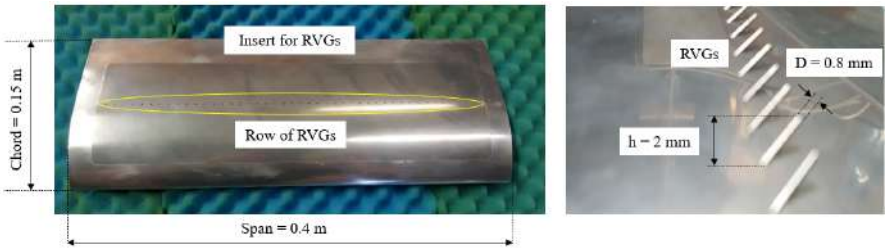

Fig. 6.2.6. DU96-W-180 airfoil with interchangeable insert for RVGs.

The dimensions of the rods are defined using the boundary layer characteristics that are estimated from the flow development on the suction side of the airfoil (RANS simulations). For efficient flow control, the geometric parameters should be proportional to the developed boundary layer thickness (δ) [27]. RVGs are characterised by four parameters: diameter (D), height (h), pitch angle (ϕ) and skew angle (θ) as seen in Figure 6.2.7. Their implementation depends on the spanwise distance between the rods

(W) and the relative chordwise location (x_{RVG}/c) with c being the chord. Implementing the optimal parameters of $h/\delta = 0.36$, $D/\delta = 0.20$ and $W/D = 10$ obtained from the detailed parametric design analysis conducted by Suarez et al. [27], the geometric characteristics of the rods are as presented in Table 6.2.1.

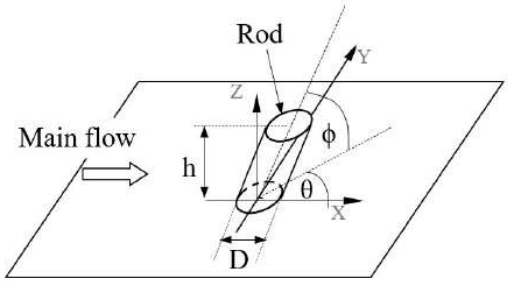

Fig. 6.2.7. A single RVG [27].

Height (h)	2 mm
Diameter (D)	0.8 mm
Skew angle (θ)	30°
Pitch angle (ϕ)	45°
Number of rods	44
Chordwise location (x_{RVG}/c)	0.5
Distance between the rods (W)	8 mm

Tab. 6.2.1. RVG design parameters

6.3 Measurement techniques

All the various measurements conducted within this research work are described below. The suction side wall pressure distribution on the airfoil is estimated through static pressure measurements. Pressure taps are located in the midspan of the airfoil at a distance of 10 mm from each other on the suction side. The first pressure tap is located at $x/c = 0.16$ and the last tap at $x/c = 0.9$ with ten taps placed inbetween. Surface pressure measurements were obtained for a range of angles of attack from $-4°$ to 20° (steps of 2°) using Honeywell TruStability transducers (range: -6 kPa – 6 kPa, uncertainty: 12.5 Pa). Differential pressure obtained from the transducers is used to compute the pressure coefficient (C_p) using Equation 6.3.1 where Δp is the measured differential pressure, ρ is the measured density and U_∞ is the flow velocity.

$$C_p = \frac{\Delta p}{0.5\rho U_\infty^2} \tag{6.3.1}$$

Surface oil flow visualization is conducted by painting the suction side of the airfoil surface using a fluorescent mixture obtained from 50 mL liquid-paraffin wax and 15-25 drops of fluorescent oil additive A-680. The flow over the airfoil is set to the operating conditions and allowed to develop for a few minutes, so the paraffin is scattered over the entire airfoil surface. The airfoil is then illuminated by an ultraviolet lamp with a wide aperture, positioned perpendicular to the model and then the resulting images are obtained.

Two dimensional PIV measurements are conducted at the mid-chord of the airfoil, both with/without RVGs to investigate the effect of generated streamwise vortices on velocity profiles in a boundary layer. The velocity measurements are obtained at three planes in the X-Z direction, located at the base (plane 1), middle (plane 2) and top (plane 3) of a single rod (Figure 6.3.8). Each plane is separated by a distance of 5 mm. Laser beam is obtained from a Quantel EverGreen EVG00200 system with wavelength of 532 nm and energy of 20 mJ/pulse. Seeding is provided by a SAFEX Twin-Fog double Power fog generator using glycol based solution. Two cameras: LaVision VC-Imager Pro LX (4870 × 3246 pixel^2, 12 bits, 7.4 micron/px) are located at a distance

of 0.16 m from the measurement planes. Both cameras are equipped with Nikon AF Micro Nikkor 200 mm focal distance lenses. To offset bias errors due to peak-locking, the images are slightly defocused resulting in a particle image larger than 2 pixels [168]. LaVision high speed controller is utilized for the laser beam illumination and image aquisition. The sampling frequency for the data is 1 Hz. The field of view is $0.28c \times 0.19c$ (42×29 mm^2) with a digital resolution of 0.1 px/mm. The post processing of the data is conducted in LaVision DaVis 8.4 software using a multipass cross-correlation algorithm with window deformation [169]. The final interrogation window size is 16×16 pixel^2 with an overlap factor of 50% resulting in a spatial resolution of 0.14 mm and a vector spacing of 0.2 mm.

Measurement errors due to sources of uncertainty, calibration and lens distortion are mitigated with a self-calibration process within the DaVis software. The uncertainties in the measurement is evaluated using the Wieneke method [170]. The uncertainty on the mean freestream velocity and on the root-mean-square velocity with a 95% confidence level are $0.02U_\infty$ and $0.04\sqrt{\overline{u^2}}$ respectively computed using the method described in Rubio Carpio et al. [171].

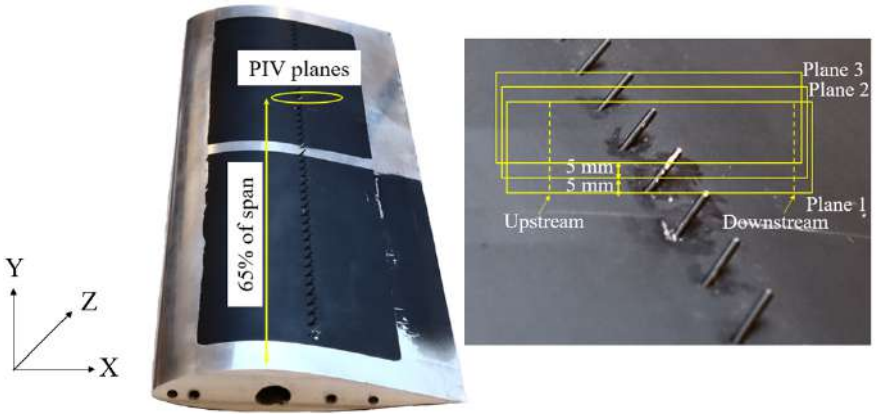

Fig. 6.3.8. PIV field of view details.

Acoustic measurements are conducted using a phased array of 64 free-field microphones (G. R. A. S. 40 PH) with a frequency range of 10 Hz - 20 kHz ($\pm$ 1 dB), maximum output of 135 dB (reference pressure of 2×10^{-5} Pa), with integrated CCP pre-amplifiers is implemented. The microphones are arranged in an adapted Underbrink design [172, 173] with 7 spiral arms of 9 microphones each as seen in Figure 6.3.9 with one microphone at the center of the array. The diameter of the array is 2 m and the distance from the centre of the array to the airfoil at AoA = 0° is 1 m. The trailing edge of the airfoil is 15 cm below the centre microphone. Microphone array has a sampling frequency of 51 kHz and a recording time of 20 s.

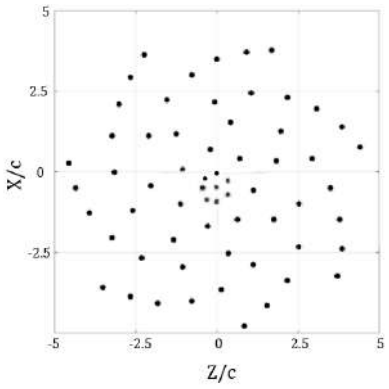

Fig. 6.3.9. Adapted Underbrink design [171].

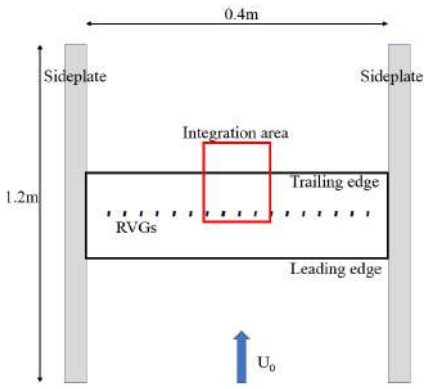

Fig. 6.3.10. Region of interest (ROI).

Conventional frequency domain beamforming described in detail in section 2.9.1 is applied to the measured acoustic data to identify noise sources. The phase difference in the measured signals from spatially separated microphones of the array is utilized [174]. The airfoil acts as the scan plane defined by grid points which are each assumed to be potential sound sources whose power is to be computed [140]. Applying Fourier transform and windowing using a Hanning weighting function with 50 % data overlap [141] the cross-spectral matric (CSM) is obtained. Using steering vectors, the source power at every grid point on the scan plane is obtained with an accuracy of 1 dB [175]. The scan grid plane is of the range $-0.35 < x < 0.35$ and $-0.25 < y < 0.25$ where x-coordinate denotes the spanwise direction and y-coordinate denotes the chordwise direction. The minimum distance between the two sources ($\triangle l$) that can be resolved is governed by the Rayleigh criterion [176] (Equation 6.3.2)

$$\triangle l \approx 1.22h\frac{c_o}{fD} = 1.22h\frac{\lambda}{D}. \tag{6.3.2}$$

With distance to the scan plane (h) being 1 m, c_o as speed of sound in m/s, λ as acoustic wavelength in m, arrray aperture (D) of 2 m, this microphone array has a Rayleigh resolution range of 2.12 m – 0.01 m for the corresponding frequency (f) range of 100 Hz – 20 000 Hz. Due to the tunnel cutoff, measurements are conducted from 300 Hz – 4000 Hz. However, the rods self-noise is observed only at contour maps of much higher frequencies (∼5000 Hz – 7000 Hz). Additionally, only the difference in SPL between the flow controlled and reference case is plotted to reduce the impact of background noise at higher frequencies. For analyzing the impact of RVGs, the sound pressure levels are obtained by integrating the specific region of interest (ROI) [177], $0.38 < x/s < 0.63$ and $0.47 < y/c < 1.4$ presented in Figure 6.3.10. All presented spectra are in one-third-octave bands.

To identify some of the weak secondary sources such as the rods, the High Resolution CleanSC deconvolution method described in detail in section 2.9.2 is applied. This method removes the sidelobes due to the dominant noise sources, from the CSM matrix, in an iterative process to clean up the source map. During measurements, the acoustic array is placed outside the jet nozzle flow in a stationary medium and the acoustic source (airfoil) is placed in the jet flow (moving medium). The acoustic waves travel

through both the moving and the stationary medium before they are recorded by the microphones. This necessitates a correction in the steering vector. One of the easiest method is to apply this correction to the source map in the opposite direction to the flow for low speed applications [178]. Sound waves from the airfoil travel up to the shear layers after which they are propagating in a stationary medium to the microphone array. The shear layers start developing from the nozzle jet exit and along the side plates of the test section set-up and are a result of the jet flow interacting with the walls (boundary layer). This region on the shear layer appears more downstream than the true source location thus showing sources on the SPL contour maps to be shifted downstream. This is corrected using the Equation 6.3.3 [178]:

$$y = Mw_f \tag{6.3.3}$$

where, y is the approximate distance of the downstream shift of the source location in metres, M is the Mach number of the flow and w_f is the the distance of the source from the shear layers in metres. Computing the Mach number from flow velocity of 30 m/s and speed of sound of 347 m/s gives $M = 0.086$. Using recommendations from Luesutthiviboon et al. [149], a value of $w_f = 0.5$ gives a downstream shift of $y = 0.05$ m.

The impact of the streamwise vortices generated by the RVGs on the overall sound generated by the airfoil is analyzed through a comparitive spectral analysis (SPL, OASPL), conducted for a range of frequencies. The broadband trailing edge noise observed on the contour maps (of SPL values) for the flow controlled airfoil is compared against the reference airfoil to analyze the impact of the streamwise vortices (RVGs) on the trailing edge noise. Measurements are conducted for the airfoils with both natural and forced transition. All the various measurements that were conducted are listed in the Table 6.3.1. Only representative results are presented in the following sections.

Tab. 6.3.1. Wind tunnel test matrix

Measurement technique	Natural transition AoA (^{0})	Forced transition AoA (^{0})
Wall pressure	-4, -2, -1, 0, 2, 4, 6, 8, 10, 11, 12, 13, 14, 15, 16, 17, 18, 19, 20, 22, 24, 26	-4, -2, -1, 0, 2, 4, 6, 8, 10, 12, 14, 15, 16, 18, 20
Oil flow visualization	15, 16, 17	6, 8, 10, 12, 14
Particle image velocimetry	–	8, 10
Acoustic microphone array	4, 6, 8, 10, 12, 14, 15	4, 6, 8, 10, 12, 14

6.4 Flow analysis

The measured pressure for the reference airfoil is presented in Figure 6.4.11, for the installation angle of 4°. The presence of a laminar separation bubble in the untripped configuration is clearly visible in Figure 6.4.11a. Application of a trip-tape induces the transition to the turbulent flow thus eliminating laminar separation, observed from the pressure curves. Airfoils with natural transition presented a laminar separation bubble occuring close to the leading edge. Laminar separation is undesirable specifically in the analysis of the flow and acoustic impact of RVGs on turbulent flow separation -

which is the central objective of this research. With the implementation of a trip-tape, the boundary layer is forced to undergo a transition to turbulent nature thus avoiding laminar separation. Additionally, to correlate to practical operating conditions of wind turbines that have turbulent nature of flow over their blades due to roughness etc., forced transition in ensured.

The measured pressure is compared with the XFOIL code prediction to evaluate the effective angle of attack. There is an acceptable agreeement between the measured data at geometric angle 4° with the XFOIL prediction at $\alpha = 0°$. Hence 4° is applied as the correction to all geometric angles. The angles mentioned henceforth are all effective inflow angles with this correction.

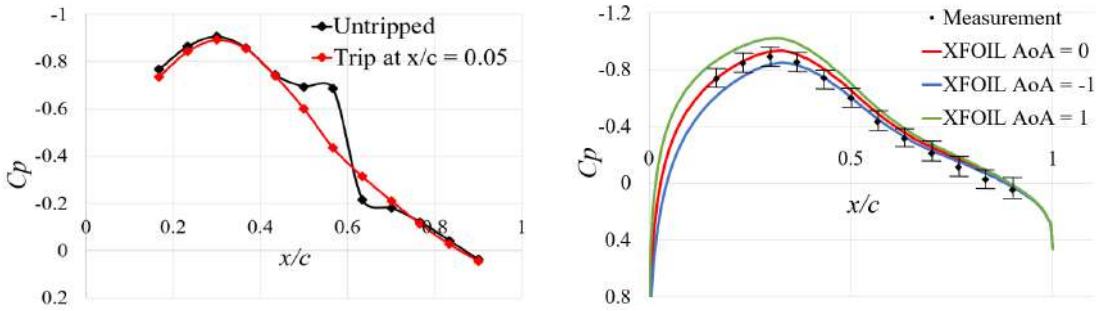

(a) Influence of tripping

(b) Open-jet correction.

Fig. 6.4.11. Pressure coefficient (C_p) for DU96-W-180 airfoil at AoA = 0°.

Oil flow visualization of the flow separation characteristics for the untripped airfoil at AoA = 11° is presented in Figure 6.4.12a. This particular angle is chosen here since both the laminar separation bubble (close to leading edge) and turbulent separation at trailing edge are clearly visible. The direction of inlet flow velocity (from the jet nozzle exit) is denoted as "A" in the figures. Corner vortices that are generated due to the interaction of the flow with the boundary layers at the region where the airfoil is mounted on the side plates, are denoted as "B". The turbulent separation line is denoted by "C" and the RVGs by "D". Natural transition of the flow leads to a laminar separation bubble that is visible close to the leading edge denoted by "F". Oil accumulates in this region. Inside the separation zone, there is a wash out of the oil. Shortly downstream of this bubble, flow then reattaches to the surface. Streaks of oil denoting flow of strong shear stresses continue to move downstream until it encounters turbulent flow separation. Turbulent flow separation starts upstream of the trailing edge and does not reattach. In the zone where the shear stresses have become weaker, droplets of oil begin to accumulate and form clusters. This is a region of flow unsteadiness and low/negative skin friction coefficient [179]. Further downstream, the flow is completely separated.

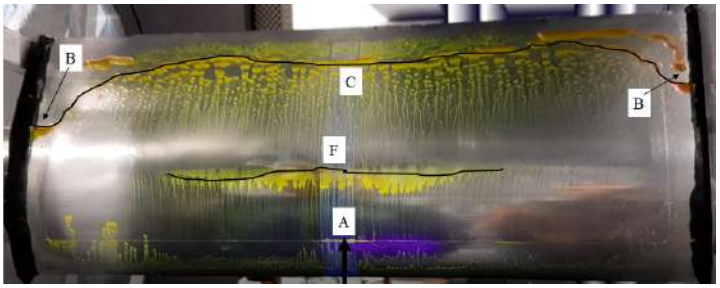

(a) Reference

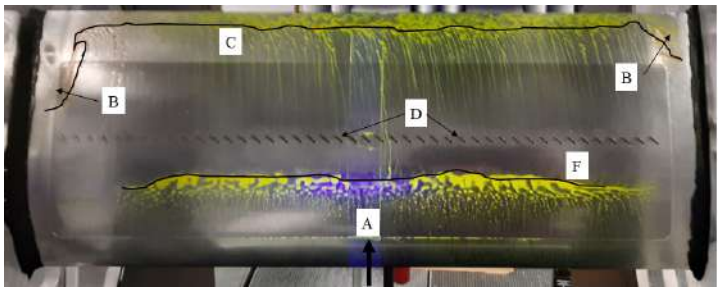

(b) RVG

Fig. 6.4.12. Oil flow visualization for DU96-W-180 airfoil with natural transition at AoA = 11°.

Visualization for the airfoil (natural transition) equipped with RVGs at AoA = 11° is observed in Figure 6.4.12b. RVGs (denoted by "D") which are located at mid-chord, generate streamwise vortices [27] that can be observed from the streaks of oil that are visible downstream of the rods. These vortices increase the shear stress and keep the flow attached to the surface. The oil streaks due to the vortices are visible up to the trailing edge. The turbulent separation zone is reduced by $\sim$ 63% reduction (Table 6.4.1).

The development of the flow structures for the airfoil with natural transition at AoA = 13° is observed in Figure 6.4.13. With increasing inflow angles, turbulent separation zone (which starts at the trailing edge) also develops and moves towards the leading edge. Such a large separation zone that extends almost up to mid-chord ("C") is visible at AoA = 13° and thus this particular angle is chosen to be shown here. This zone is reduced ($\sim$ 45%) by the installation of RVGs (D) presented in Figure 6.4.13b. The streamwise vortices energize the flow, keeping them attached to the surface longer, thus shifting the separation line towards the trailing edge (see Table 6.4.1).

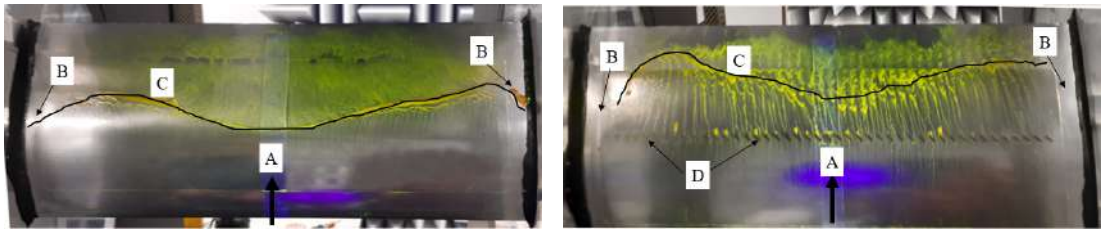

(a) Reference (b) RVG

Fig. 6.4.13. Oil flow visualization for the DU96-W-180 airfoil with natural transition at AoA = 13°

The characteristics of the flow for the airfoil with the forced transition at an effective AoA = 6° is presented in Figure 6.4.14. Numerous tiny streaks of oil moving from the leading edge towards the mid-chord represent the vortices that are generated by the trip-tape (E). A large zone of turbulent flow separation extending from the trailing edge almost up to the mid-chord is observed. The two corner vortices at each sideplate appear non uniform in size and strength which is noted in all configurations. Due to the turbulent boundary layer that is enforced by the transition, the separation zone develops in similar small increments with increasing angle for the tripped foils. This is due to the inherent stability of the turbulent boundary layer when compared to the free transition configurations [179]. It is important to note that the separation zone is not evenly formed across the airfoil span, but, is more uniform than the untripped airfoils.

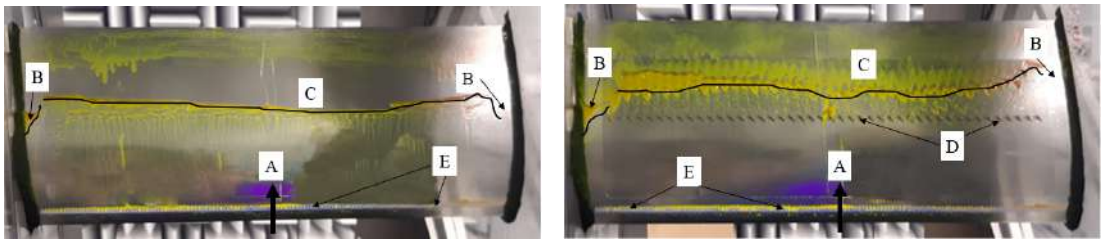

(a) Reference (b) RVG

Fig. 6.4.14. Oil flow visualization for DU96-W-180 airfoil with forced transition at AoA = 6°

Tab. 6.4.1. Normalized turbulent separation zone size comparison

Configuration	Reference	RVG	Reduction (%)
Natural transition AoA = 11°	0.11	0.04	63.6
Natural transition AoA = 13°	0.33	0.18	45.5
Fixed transition AoA = 6°	0.26	0.20	23.1

The effectiveness of the rods in reducing the separation zone is quantified in Table 6.4.1. It consists of the ratio of the turbulent separation area normalized with the suction side area. The reduction in the turbulent separation zone by RVGs is more effective in the airfoils with natural transition compared to the forced transition airfoils. This

is because the trip-tape alters the boundary layer characteristics (induces laminar to turbulent boundary layer transition) which in turn affects the efficiency of the rods. To improve the reduction of separation zone, stronger streamwise vortices must be generated. The strength of the streamwise vortices depends on the geometric characteristics of the RVGs such as the diameter and height of the rods [27]. These parameters are obtained from boundary layer thickness estimated through CFD simulations.

The evolution of the boundary layer velocities is analyzed through the measured PIV data. The mean streamwise velocity profile at the upstream location ($x/c = 0.43$) for the reference airfoil with forced transition is plotted in Figure 6.4.15. The profile is scaled using the friction velocity $u_\tau = \sqrt{\tau_w/\rho}$ to fit the theoretical boundary layer in the buffer and the logarithmic region. The value of u_τ is obtained through an iterative fitting of the measured data with the log law equation characterised by the universal constants $\kappa = 0.41$ and B = 5.1 [180]. The measured data (red diamonds) is compared with the theoretical curve. Only those measurements fitting with the law as shown in Figure 6.4.15 are utilized for further analysis of velocity components.

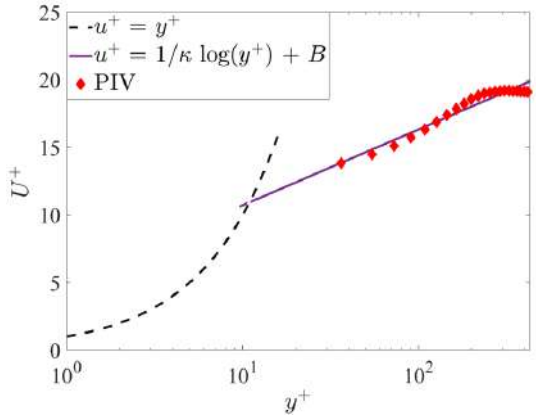

Fig. 6.4.15. Mean streamwise velocity profile with viscous scaling for reference airfoil at $x/c = 0.43$ (upstream) location.

Velocity components for both the reference and flow controlled airfoils (with forced transition) at AoA = 6° are analyzed below. Tangential and perpendicular velocity components at two streamwise locations - one before the onset of the separation at $x/c = 0.43$ (denoted as upstream) and one inside the separation zone at $x/c = 0.63$ (downstream) are plotted. Comparison of the reference and the flow controlled velocity curves is conducted to observe the impact of the rods on the evolution of the boundary layer. The velocity is normalized by the freestream velocity (U_∞) and the wall normal distance by the boundary layer thickness (δ_{99}).

The mean streamwise velocity component for the reference airfoil upstream of the rods ($x/c = 0.43$) is presented in Figure 6.4.16. Here, the data from only one plane is presented because the velocity curves at all the other planes are similar. This is due to the flow being uniform in the spanwise direction at this location. The mean streamwise velocity profiles for the RVG case are compared with the reference, far downstream of the rods (Figure 6.4.16). The variations in the velocity due to the vortical structures generated by the rods are visible in the plane 2 (red line) and plane 3 (green line). The difference in the streamwise velocity distribution is dependent on the location of the

velocity traverse in the zone of the vortex, in the spanwise direction. Similar effect has been presented for the streamwise vortices generated by jets in high speed flow by [181]. The spanwise modulation of the streamwise velocity component is observed at planes 2 and 3. At plane 2, the velocity is higher than in plane 1 up to $y/\delta_{99} = 0.3$. Above this location, lower values than at plane 1 is observed. Furthermore, in the outer part of the boundary layer, the flow becomes uniform again. More significant effect is observed at plane 3, where the velocity is even higher close to the wall (up to $y/\delta_{99} = 0.1$), then decreases and finally reaches the same value as in plane 1 and 2, close to the limit of the boundary layer. The non-uniformity of the velocity components downstream of the rods is the effect of generated vortices and their existence in the boundary layer affects the structure of the separation line. This is a typical structure for the interaction of the streamwise vortices with the reversed flow downstream of the separation line. Although the velocity components at the downstream location are in the separation zone, it is not visible in the plots presented below. This is because the height of the separation zone is quite small and the measurements in this region (close to the wall surface) are not available as observed in Figure 6.4.15.

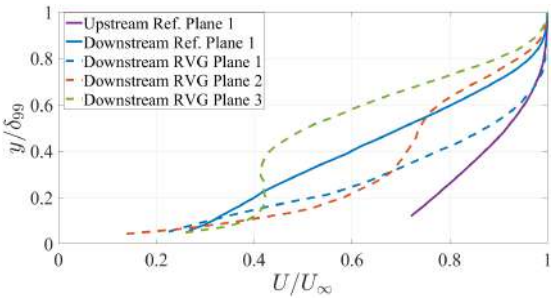

Fig. 6.4.16. Mean streamwise velocity component U/U_∞ at streamwise locations: $x/c = 0.43$ (upstream) and $x/c = 0.63$ (downstream).

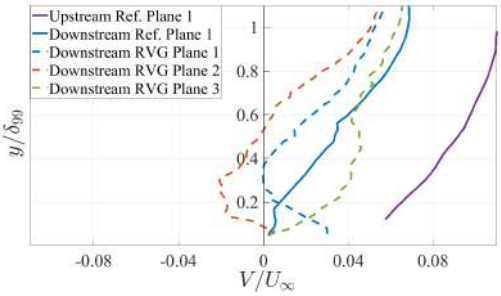

Fig. 6.4.17. Mean wall-normal velocity component V/U_∞ at streamwise locations: $x/c = 0.43$ (upstream) and $x/c = 0.63$ (downstream).

The mean wall-normal velocity components at selected traverses upstream and downstream of the RVG are presented in Figure 6.4.17. In case of the reference airfoil, without RGVs, both curves (solid lines) show the same trend. The only difference is a lower magnitude of this velocity component farther downstream. A different distribution of the velocity components are observed for the airfoil equipped with the rods due to the generated vortices operating in the boundary layer downstream of each rod [26]. Curves representing neighbouring traverses (planes 1-3) show spanwise non-uniformity of the velocity downstream of the RVGs. The negative velocity values indicate that the flow is directed towards the wall while the positive values indicates that the flow is moving away from the wall, an effect of the local rotation enforced by the vortex. Thus the streamwise vortex transports momentum from the outer region of the flow to the boundary layer, energizing it.

The boundary layer characteristics for the flow controlled airfoil are compared against the reference foil at both upstream and downstream locations in Table 6.4.2. The boundary layer thickness δ_{99} and the velocity $U_\infty = U(\delta_{99})$ are obtained from the velocity profiles. The boundary layer displacement thickness δ^*, momentum thickness

θ^* (from Equation 6.4.1) and the shape factor H (δ^*/θ^*) are also computed [182].

$$\delta^* = \int_0^{\delta_{99}} \left(1 - \frac{u}{u_\infty}\right) dy \qquad (6.4.1)$$

$$\theta^* = \int_0^{\delta_{99}} \frac{u}{u_\infty}\left(1 - \frac{u}{u_\infty}\right) dy \ . \qquad (6.4.2)$$

Tab. 6.4.2. Boundary layer parameters at streamwise locations: $x/c = 0.43$ (upstream) and $x/c = 0.63$ (downstream).

	Upstream	Downstream			
	Plane 1	Plane 1		Plane 2	Plane 3
Parameters	Reference	Reference	RVG	RVG	RVG
U_∞ (m/s)	39.3	33.6	34	34.1	33.9
δ_{99} (mm)	2.4	5.1	5.4	6.5	5.9
δ^* (mm)	0.3	1.6	1.2	1.8	2.4
θ^* (mm)	0.2	0.8	0.6	0.9	1.1
H	1.3	2.1	2.0	1.9	2.3

The boundary layer thickness δ_{99} is higher for the RVGs when compared to the reference airfoil. Rods energize the flow within the boundary layer indicated by the increased velocity values at the three planes. The boundary layer thickness is higher at plane 2 compared to the other planes indicating a strong streamwise vortex. The values of the boundary layer parameters for the three planes are different because of the strong vortex generated by the rod.

The turbulent flow field at both the upstream and downstream locations for the wall-parallel velocity and the wall-normal velocity components are represented in Figures 6.4.18 and 6.4.19 respectively.

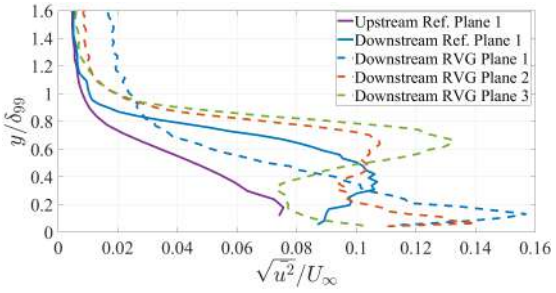

Fig. 6.4.18. R.m.s of tangential velocity $\sqrt{\overline{u^2}}/U_\infty$ at streamwise locations: $x/c = 0.43$ (upstream) and $x/c = 0.63$ (downstream).

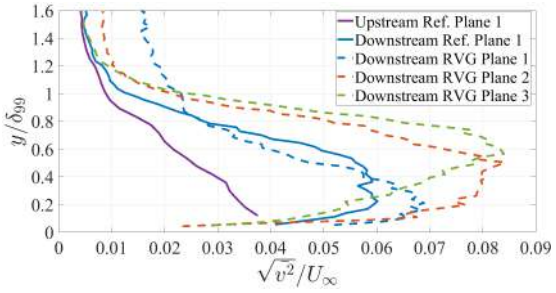

Fig. 6.4.19. R.m.s of normal velocity $\sqrt{\overline{v^2}}/U_\infty$ at streamwise locations: $x/c = 0.43$ (upstream) and $x/c = 0.63$ (downstream).

Similar to the trends of the mean velocities discussed in the previous section, the fluctuations of the r.m.s velocity components increases at the downstream location compared to the upstream location. For the RVG case, there is an increase in the velocity fluctuations close to the wall indicating that the vortex (generated by the rods) energizes the flow.

6.5 Acoustic analysis

6.5.1 Influence of angle of attack

To assess the influence of increasing inflow angles on the sound levels generated by the airfoils, SPL curves are plotted for a few chosen angles (0°, 4°, 8° and 11°) in the Region of Interest - ROI (Figure 6.3.10) for the reference airfoil with both natural and forced transition (Figure 6.5.20). Airfoils with natural transition present spikes in the mid-frequency ranges (∼500 Hz – 2500 Hz) (Figure 6.5.20a). These spikes indicate tonal noise components due to the presence of the laminar separation bubble [183] that was observed close to the leading edge during oil flow visualization (Figure 6.4.12a). For inflow angles up to 8°, there is a presence of tonal noise in the frequency range 1600 Hz – 2500 Hz and from AoA = 8° onwards (small turbulent separation zone begins to form close to the trailing edge), the tonal components appear at lower frequencies (∼400 Hz – 2000 Hz). For frequencies below and above this range, sound emitted is of broadband nature. With increasing inflow angles, the emitted sound levels increase and the peak values emitted also shifts to lower frequencies at almost all frequencies.

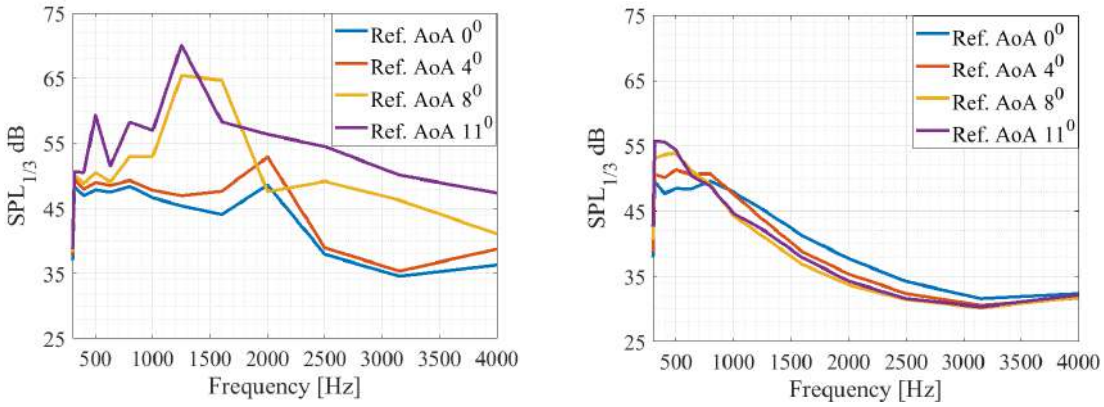

(a) Natural transition

(b) Forced transition

Fig. 6.5.20. SPL for reference airfoil at AoA = 0°, 4°, 8° and 11°.

SPL curves for the airfoil with forced transition depict an increase in the sound emitted with increasing inflow angles at low frequencies (<550 Hz). The peak values are also emitted at lower frequencies with increasing inflow angles. The sound pressure levels then continually decrease for the medium frequencies up to ∼3150 Hz and then increase slightly. The sound emission at mid and high frequencies (⩾750 Hz) is more for airfoils at low AoA (0° and 4°) than for airfoils at higher angles (8° and 11°).

The overall SPL values emitted by the reference airfoils for the range of inflow angles are presented in Table 6.5.1. At low inflow angles (no turbulent separation) up to 4° both configurations have comparable OASPL values. At higher inflow angles (turbulent separation), the untripped configuration exhibits higher sound levels compared to tripped airfoils. Airfoils with natural transition have laminar separation close to the leading edge and turbulent separation close to trailing edge causing much stronger sound pressure levels. Airfoils with forced transition exhibit a small increase in OASPL values with increasing inflow angles. At higher inflow angles, the turbulent separation zone also grows (gradually). Thus the separation noise sources also increase thereby

leading to increase in sound levels.

Tab. 6.5.1. Overall Sound Pressure Level (OASPL) for reference airfoils

Configuration	Natural transition	Forced transition
AoA = 0°	56.9 dB	57.0 dB
AoA = 4°	58.9 dB	58.4 dB
AoA = 8°	68.7 dB	59.8 dB
AoA = 11°	71.5 dB	61.0 dB

6.5.2 Spectral analysis for airfoils with natural transition

For a clear perspective on the acoustic effect of RVGs, the sound levels over a broad range of frequency spectrum must be analyzed. The contour maps of SPL (one-third octave bands) for the airfoils with natural transition at AoA = 11° at various frequencies are presented below. This particular angle is chosen as both the laminar separation (close to the leading edge) and turbulent separation (close to the trailing edge) was observed during the oil flow visualizations (Figure 6.4.12a).

A typical contour map for the reference and flow controlled airfoil at frequency of 1600 Hz is presented in Figure 6.5.21. A decrease in the trailing edge noise is noted for the airfoil equipped with RVGs. Furthermore, to assess the sound sources particularly affected by the rods, contour map of ΔSPL (difference in SPL between the reference and RVGs airfoils) is plotted in Figure 6.5.22. This particular frequency is chosen because the maximum difference in the SPL values is observed. A large decrease (∼9 dB) in the sound levels at 1600 Hz is noted. With the implementation of the rods the separation zone is reduced and consequently a reduction in separation noise is expected. However, the rods induce the pressure fluctuations within a vortical structure generated downstream thereby an increase in the noise at certain frequencies is anticipated. In this particular configuration, the decrease in the noise due to reduced turbulent separation is predominant over an increase in noise due to increased loading. A shift in the sound sources towards one side can be observed in almost all the contour maps. The position of these asymmetries also changes with varying frequencies for both the reference and RVG cases.

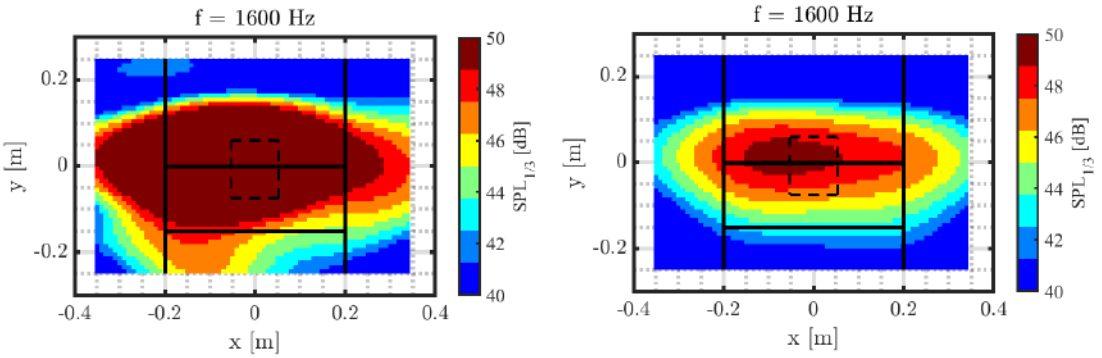

(a) Clean (b) RVG

Fig. 6.5.21. Contour maps of SPL for airfoils (natural transition) with AoA = 11° at 1600 Hz frequency.

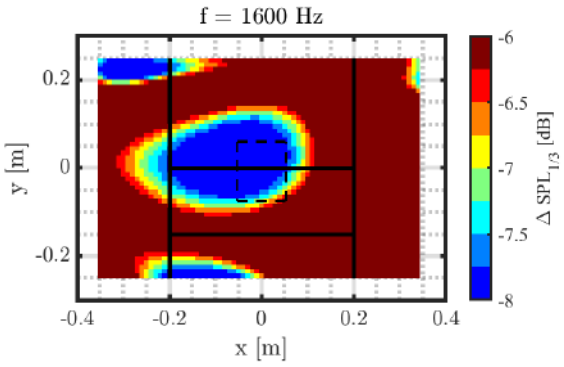

Fig. 6.5.22. Contour map of ΔSPL for airfoil (natural transition) with AoA = 11° at 1600 Hz frequency.

To quantitatively assess the impact of the rods on the trailing edge noise over a range of frequencies, the sound pressure levels integrated in the ROI (Figure 6.3.10) are presented in the following sections. The ΔSPL ($SPL_{RVGs} - SPL_{Reference}$) curves at two angles - low inflow angle with no turbulent separation and at higher inflow angle with a large turbulent separation zone for airfoils with natural transition (Figures 6.5.23 and 6.5.24) are analyzed below.

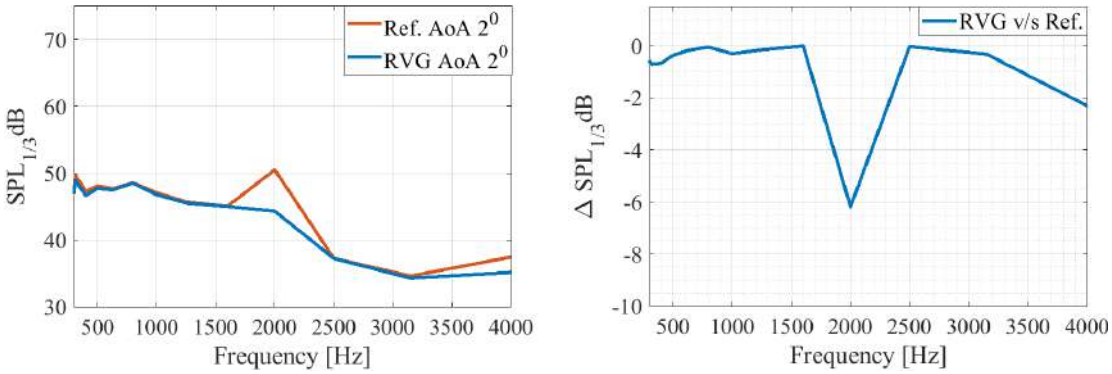

Fig. 6.5.23. Comparitive SPL analysis for DU96-W-180 airfoil (natural transition) at AoA = 2°.

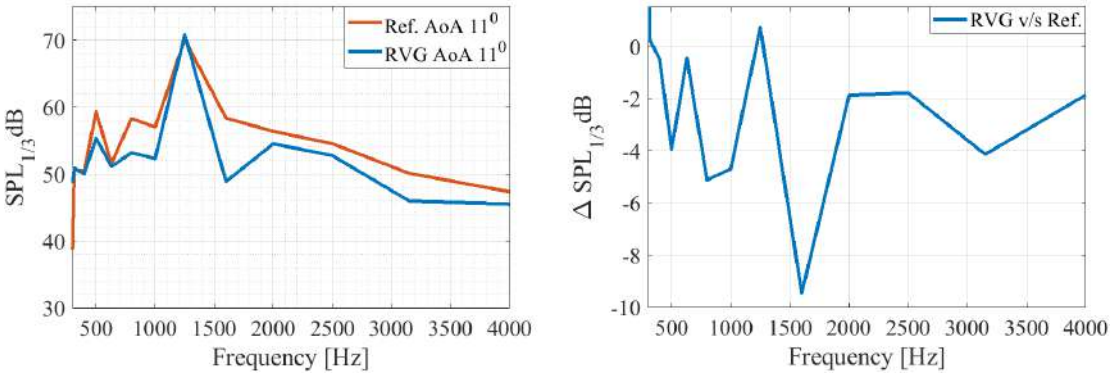

Fig. 6.5.24. Comparitive SPL analysis for DU96-W-180 airfoil (natural transition) at AoA = 11°.

Airfoils at higher inflow angle (Figure 6.5.24) exhibit higher sound levels when compared to the airfoils at lower angle of attack (Figure 6.5.23). With increasing inflow angles, the tonal components grow stronger. This is expected as the size of the laminar separation bubble also increases at higher angles. The difference in the sound pressure levels between the reference and the RVG cases also increases with increasing inflow angles. A decrease in the trailing edge noise is obtained for the airfoil with RVGs at all the frequencies for the inflow angle of 2°. A maximum reduction of 6 dB is achieved at a frequency of 2000 Hz (Figure 6.5.23). Even though there is no turbulent separation at this angle, the RVGs reduce the emitted noise. This is counterintuitive and further research into this is required.

The difference in SPL curves between the reference and RVG case at AoA = 11° (turbulent separation) is presented in Figure 6.5.24. A decrease in the tonal components at low and mid frequencies are observed. The airfoil with flow control device decreases trailing edge noise at almost all the frequencies. There is a slight increase in the sound levels at 1200 Hz. However this increase is within the error margins (±1 dB) of the microphone array. The overall sound pressure levels are presented in Table 6.5.2.

6.5.3 Spectral analysis for airfoils with forced transition

The SPL contour maps for airfoils (forced transition) at AoA = 6° are analyzed for a range of frequencies from 300 Hz – 4000 Hz. This particular angle is chosen since a large turbulent separation zone extending almost up to mid-chord is observed in Figure 6.4.14. To present the various sources, one sample frequency of 3150 Hz is chosen and the original contour maps for the reference and the RVGs airfoil are presented in Figure 6.5.25. Contour maps of another frequency – 1600 Hz are also presented in Figure 6.5.26. Additionally, the contour maps of ΔSPL are plotted at frequencies - 3150 Hz (Figure 6.5.27) and 1600 Hz (Figure 6.5.28). These two frequencies are specifically chosen because the various noise sources are visible at 3150 Hz and the maximum difference, negatively, i.e increase in noise levels between the flow controlled and reference airfoils at 1600 Hz (Figure 6.5.28).

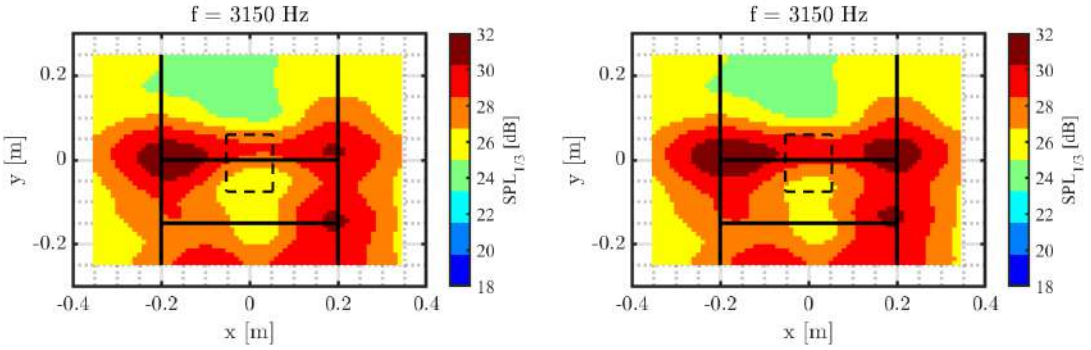

(a) Reference (b) RVG

Fig. 6.5.25. Contour maps of SPL for airfoils with AoA = 6° at high frequency (3150 Hz).

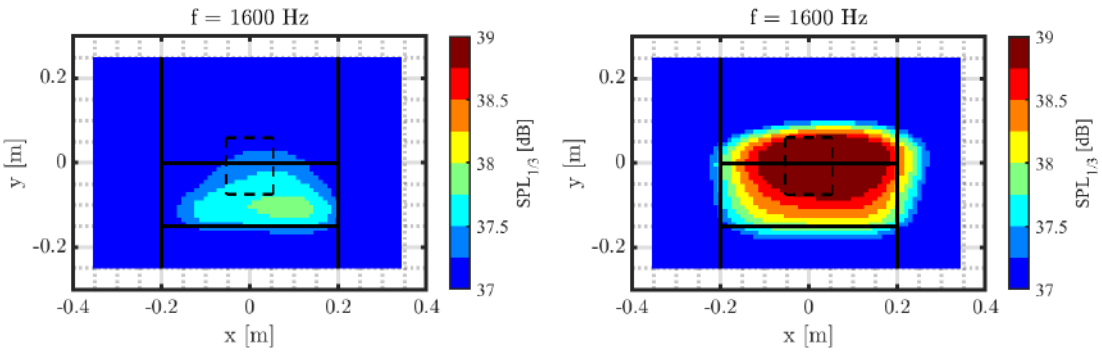

(a) Reference (b) RVG

Fig. 6.5.26. Contour maps of SPL for airfoils with AoA = 6° at medium frequency (1600 Hz).

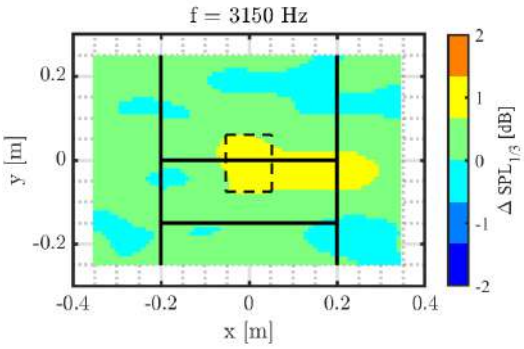

Fig. 6.5.27. Contour map of ΔSPL for AoA = 6° at mid frequency (3150 Hz).

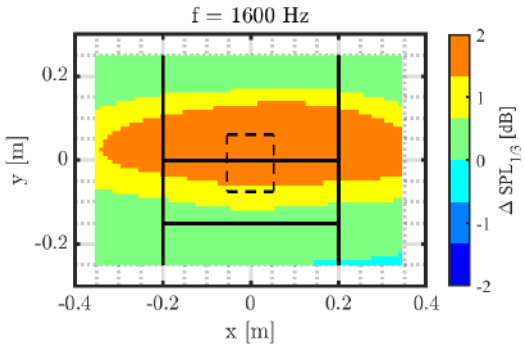

Fig. 6.5.28. Contour map of ΔSPL for AoA = 6° at high frequency (1600 Hz).

The presence of different sound sources can be observed at different frequencies. Noise sources due to the sideplate installation are observed in the maps at mid and high frequencies (eg. Figure 6.5.25). Presence of asymmetry of the sources at almost all frequencies is noted even in airfoils with forced transition. Some of the possible explanations for this - firstly, the strength of the two corner vortices that are formed are not equal as was observed in the oil flow visualizations (Figure 6.4.14). RVGs generate streamwise vortices which are unidirectional that could lead to non-uniform reduction in corner vortices. The unequal size and strength of the corner vortices could lead to different dominant frequencies for each of them. Secondly, the array uncertainty is 1 dB and the variation in the sound levels of the different sources are quite low $\simeq$ 0.1 - 2.5 dB. Thirdly, the sources have to be at sufficiently larger distances from each other i.e atleast at distances larger than the Rayleigh resolution limit to be distinguishable on the contour maps. Further research into this is required.

The rods generate more trailing edge noise at mid and high frequencies. The streamwise vortices generated by the RVGs (Figure 6.4.16) energize the boundary layer flow by bringing in high momentum fluid closer to the airfoil surface. This leads to increased pressure fluctuations thereby increasing the trailing edge noise. For instance, a maximum increase of ∼2 dB by the rods is observed at 1600 Hz (Figure 6.5.28).

The OASPL trends are similar at both, low inflow angle of 2° (no turbulent separation) and at high inflow angle of 6° (turbulent separation). For the airfoils with forced transition, due to the stable turbulent boundary layer that is developed, the tonal components are absent in Figures 6.5.29 and 6.5.30. For AoA = 2°, frequencies up to 1200 Hz, the rods decrease the emitted sound levels and above 1200 Hz, airfoil with RVGs begin to emit louder sound than the reference airfoils (Figure 6.5.29). SPL values increases until ∼2000 Hz and then for higher frequencies the values remain almost the same. For AoA = 6°, frequencies up to 700 Hz, airfoil with RVGs emit lower sound levels than the reference case, from 700 Hz – 1000 Hz, airfoil with RVGs emit linearly increasing sound levels. Above 1000 Hz, airfoil with RVGs generate more noise than reference airfoils however, the SPL difference decreases (Figure 6.5.30). It is important to note that the increase of noise levels by the rods are all within ∼2 dB and occurs at total sound pressure levels which are significantly lower than the peak amplitudes generated at low frequencies, thus making it negligible.

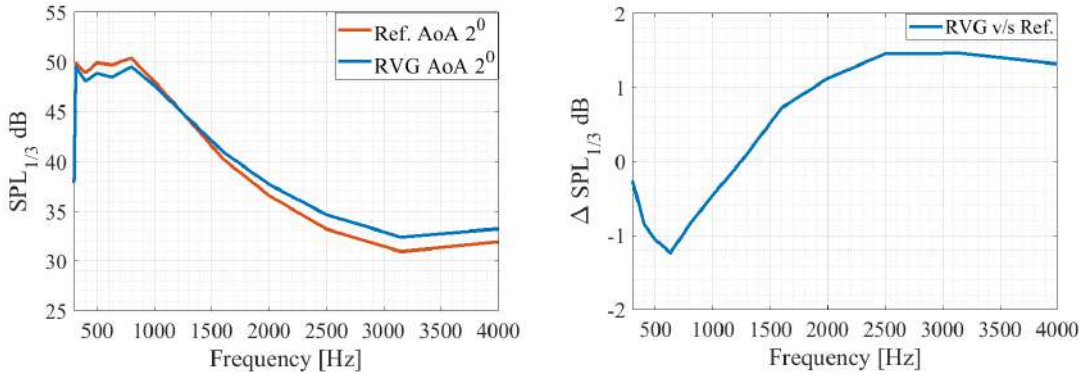

Fig. 6.5.29. Comparitive SPL analysis for DU96-W-180 airfoil (forced transition) at AoA = 2°.

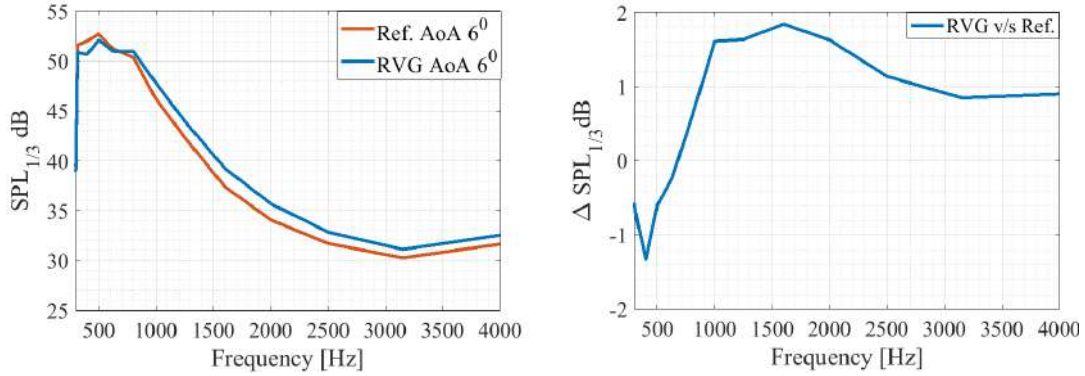

Fig. 6.5.30. Comparitive SPL analysis for DU96-W-180 airfoil (forced transition) at AoA = 6°.

The overall sound pressure levels are presented in Table 6.5.2 along with their difference. The difference ΔOASPL is computed using $\text{OASPL}_{RVGs} - \text{OASPL}_{Reference}$.

Tab. 6.5.2. Overall sound pressure level

Configuration	AoA	Reference	RVG	ΔOASPL
Natural transition	2°	57.6 dB	56.5 dB	−1.1 dB
Natural transition	11°	71.5 dB	71.4 dB	−0.1 dB
Forced transition	2°	57.7 dB	57.1 dB	−0.67 dB
Forced transition	6°	59.1 dB	58.8 dB	−0.26 dB

From the table, the overall sound levels are comparable for the reference and the flow controlled cases. There is a drastic increase in the overall sound levels with increasing inflow angles for airfoils with natural transition when compared to the airfoils with forced transition. The impact of the rods on the OASPL values is negligible for human hearing and perception. Thus the rods do not affect the overall sound emitted by the airfoil.

RVG (embedded in the boundary layer) effect can be observed on the contour maps

at certain frequencies, estimated by their acoustic wavelength λ [65]. Sound is emitted due to the scattering of the pressure waves by the eddies generated by the rods [65,125]. For an efficient sound scattering mechanism, the acoustic wavelength and the eddies created by the RVGs have to be proportional in size. The dominant frequency (f) at which they can be observed is determined using Strouhal number (St). This is calculated using $St = fD/U$, with rod diameter (D) of 0.8 mm, St $\approx$ 0.2 [184] and approximate flow velocity (velocity inside the boundary layer is non-uniform) between the range of 15 m/s – 30 m/s ($U/2$ to U_{max}). This yields a dominant frequency range of 3750 Hz – 7500 Hz. The acoustic wavelength (λ) can be estimated using Equation 6.5.1 [65]:

$$f = U_o/\lambda. \tag{6.5.1}$$

With a flow velocity of $U_o = 30$ m/s, for selected frequencies, for example the dominant frequency $f = 7500$ Hz estimates $\lambda = 4$ mm. The characteristic dimension of RVGs (h) computed from RVG height (H) of 2 mm and RVG skew angle (α) of 30° is $h = 4$ mm. With the assumption that the biggest eddies in the turbulent boundary layer are dominant [65], at frequencies lower than the dominant frequency (for example $f = 1000$ Hz predicts $\lambda = 30$ mm), the acoustic wavelength is larger than the eddies from RVGs ($h << \lambda$), thus no scattering of acoustic waves takes place. At very high frequencies compared to the dominant frequency (for example $f = 12\,000$ Hz predicts $\lambda = 2.5$ mm), the acoustic wavelength is much smaller than the eddy size ($h >> \lambda$) and there is no effective distortion of the sound waves. At the dominant frequency, the acoustic wavelength ($\lambda = 4$ mm) is proportional to the eddies from RVGs ($h = 4$ mm) and hence an efficient scattering of sound waves takes place.

The contour maps for a frequency range around the dominant frequency i.e 5623 Hz – 7079 Hz is plotted. The maps from the CBF method depict many sources including the dominant sound sources due to the side plate installation, masking the sources due to the rods. To clean up the secondary lobes and to decrease the background noise, only the contour map of the difference in SPL (between the reference and RVGs airfoil), from the CleanSC method is presented in Figure 6.5.31.

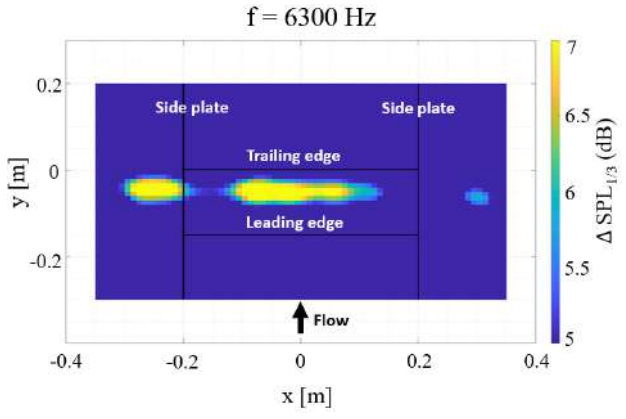

Fig. 6.5.31. Contour map of ΔSPL for airfoil with AoA = 6° at dominant frequency (6300 Hz) from CleanSC.

The contour map exhibits the presence of rods at mid-chord. The rods generate dominant sources of self noise only at very high frequencies. They generate higher

sound levels of ∼2 dB when compared to the reference airfoil. However, the overall sound levels are quite low (26 dB).

6.6 Summary

The impact of specific type of vortex generators - rod type (RVGs) on the separation zone reduction and on the trailing edge noise emitted by a wind turbine airfoil (DU96-W-180) is evaluated. Turbulent flow separation close to the trailing edge occurs on airfoils as the inflow angles are increased and a large separation zone extending up to mid-chord is observed after certain inflow angles. A 23% reduction in the separation zone due to the mixing of the streamwise vortices (generated by the rods) within the boundary layer is observed through oil flow visualization. The re-energizing of the boundary layer by the rods was characterised through PIV analysis. The turbulent boundary layer has been analyzed upstream and downstream of the RVGs, both qualitatively and quantitatively. The mean and instantaneous components of both wall-parallel and wall-normal velocity across the three planes in the spanwise direction indicate the presence of a streamwise vortex. Thus, the impact of the RVGs on the boundary layer characteristics is estimated.

Similar to other classical VG types, the strength of the streamwise vortices generated by the rods is determined by their geometric dimensions and their installation location. This in turn impacts both their effectiveness in the reduction of boundary layer separation and sound emission. The impact on trailing edge noise varies with the frequency subjected to incoming flow characateristics (boundary layer thickness) influenced by the inflow velocities and angles.

The effect of RVGs on the broadband trailing edge noise is analyzed through the spectral analysis for a range of frequencies. The relative differences in the SPL and the OASPL between the reference airfoil and the airfoil equipped with the RVGs have been investigated. An increase in the overall sound pressure levels is noted for the airfoils with the flow control device if inflow angle increases for airfoils with both natural and forced transition. This is anticipated since the boundary layer thickness and flow separation increases with increasing angles of attack.

For airfoils with natural transition, the rods decrease the trailing edge noise at all frequency ranges and also at all angles – low (no turbulent flow separation) or high angles (with turbulent flow separation). On the contrary, for airfoils with forced transition, the RVGs decrease noise at low frequencies while increasing the levels slightly at mid and high frequency ranges, also, at all inflow angles (with/without turbulent flow separation). The reduction in sound levels at low frequencies is possibly due to the reduction of the turbulent flow separation zone by the rods thereby reducing separation noise. For airfoils with natural transition, the streamwise vortices generated by the rods interact with the vortices in the boundary layer leading to less correlated vortices at the trailing edge thus reducing the turbulent boundary layer trailing edge noise at all frequencies. However, for airfoils with forced transition, the interaction of the vortices from the rods and the turbulent boundary layer leads to stronger vortical structures reaching the trailing edge and thus increasing broadband noise at mid and high frequencies. Further research into this hypothesis using detailed flow analysis (for example LES) is required.

Similar to the triangular vane type VGs [65], the RVGs also increase trailing edge

noise at higher frequencies. However they depict a decrease in the separation noise at low frequencies - particularly up to 1200 Hz at angles where there is no separation and up to 700 Hz at angles where there is a large separation for airfoils with forced transition. Additionally, it is important to note that the relative increase in values at higher frequencies is < 2 dB which is small (array uncertainty is ± 1 dB) compared to the overall sound pressure levels. The RVG self-noise of ~ 2 dB is emitted only at certain dominant frequencies estimated through the acoustic wavelength which is dependent on the boundary layer thickness. This self-noise is influenced by the characteristic dimension of the RVGs. The decrease in sound levels at low frequency by the RVGs is promising especially for wind turbine applications since it is the low frequency sounds that propagates to long distances, causing harm to residents near wind farms.

Chapter 7

Conclusions and future work

7.1 Conclusions

A fundamental understanding of the physics and mechanisms of sound generation and propagation through the acoustic analogies and the elementary acoustic sources is the main objective of this research work. This was accomplished by developing, validating and verifying an in-house aeroacoustic tool for investigating sound predictions of rotating bodies in subsonic motion. It is based on the integral solution to the exact FW–H acoustic analogy derived by Farassat in time domain (described in Chapter 2). This numerical aeroacoustic code predicts acoustic pressure signal in detail – thickness noise, loading noise, near and far-field contributions for rotating bodies. The required input for the code can be provided from existing data obtained from different commercial/non-commercial CFD solvers (post-processing) as well as during the design phase of new projects.

A thorough validation of the developed code was conducted for four main cases, both, simple and rotating elementary sources. The acoustic pressure predicted by the FW–H code was successfully compared against the analytical solutions to the elementary sources (Chapter 3), both, qualitatively and quantitatively. The total pressure signal along with its components (near- and the far-field terms) also have a good comparison. Spatial, temporal and size discretization studies were conducted for each of the four validation cases in both time and frequency domains (amplitude, P_{rms}, frequency, SPL spectra and OASPL) until the relative error (difference between the analytical solution and the FW–H code prediction) was less than 0.5% (accuracy measure). Significant amount of time was spent in the validation and verification part of the code development. This was because many of the variables used in the acoustic analogy are not straightforward and a thorough understanding of them was achieved only after rigourous testing (using several models and observer configurations). The functionality and flexibility of the code in handling various mechanisms and configurations has been successfully demonstrated.

Additionally, to obtain the analytical solutions, codes for both stationary/moving monopole and dipole were developed (described in Chapter 3). Apart from implementing analytical solutions to elementary sources, these codes were further extended to distributed point sources mimicking thickness and loading noise of real life applications. The extended elementary source codes can also be used for quick preliminary acoustic analysis during the design phase of rotor blades.

The validated code was utilized for the investigation of low frequency in-plane harmonic noise (LF-IPH) of the Sargent and Schmitz helicopter rotor in a low-thrust

hover in Chapter 4. A thorough, successful comparison of the total signal and its various components (near and far-field terms of both thickness and loading noise) has been conducted against reference code [157]. The total signals were also verified against the measurement data of University of Maryland [157]. The effect of acoustic panel density and distribution (computational grid), time-step size on the acoustic pressure signals were quantified. A good comparison of the predicted thickness noise with the reference noise was obtained.

An in-depth loading noise analysis was conducted through both RANS simulations and quick BEMT methods. The quantitative and qualitative contribution of different forces (in-plane and out-of-plane) to the loading noise prediction were presented. The prediction of the loading noise from the BEMT + FW–H code solution is in very good agreement with the reference code solutions (also BEMT). The difference in the OASPL values predicted by the code is 0.2 dB when compared to the reference solution. However, the comparison of the loading signal from the CFD + FW–H with the reference solution presents an underprediction of the peak positive amplitude ($\sim$ 1 Pa) even though the main pulse shape is captured well. This can be explained due to the lower blade loading obtained from CFD. Comparison of the total acoustic pressure by the in-house FW–H code as well as the reference code with the experimental signal shows an underprediction of the peak negative by 10% (BEMT + FW–H), 9% (CFD + FW–H) and 9% (reference code) respectively. This is due to the presence of low-frequency reflections in the measurement chamber.

Acoustic investigation of the impact of implementing RVGs on a wind turbine rotor is presented in Chapter 5. Utilizing the steady pressure data for the NREL Phase VI rotor as input to the verified aeroacoustic code, detailed analysis on the sound heard by different observers was conducted. Comparison of the various components of sound - thickness and loading noise along with their far-field and near-field contributions was performed for in-plane and out-of-plane microphones. The main focus of this investigation was the relative difference in the sound emitted by the rotor blades when RVGs are implemented. RVGs are implemented close to the tip region and only at a fraction (3.7%) of blade span. Results show no difference in the sound due to the RVGs in any of the sound metrics analyzed in both time and frequency domain. Furthermore, local analysis of the different components of sound were conducted in the important regions - tip region and the region where the rods are located to further understand the influence of the control devices. Neither global nor local analysis depict any significant change in the overall sound pressure levels. This acoustic information will aid in designing better flow control devices (RVGs) that can improve aerodynamic performance by reducing turbulent boundary layer separation without any significant noise penalty arising from the additional devices. Only steady rotational noise for the wind turbine is presented in the current work due to the availability of only steady pressure data in the research group. The code is capable of predicting the total loading noise including unsteady noise as this functionality is validated through the various elementary cases (section 3.5).

To assess the impact of the RVGs on the flow characteristics and the trailing edge noise emission of a wind turbine airfoil (DU96-W-180), measurements were conducted at the Low Speed Laboratories at Delft University of Technology (in Chapter 6). The design of the airfoil model with RVGs for the specific test section was conducted through numerical simulations. This numerical model was firstly validated against an existing

data from an experimental campaign that was conducted by Suryadi et al. [162]. A satisfactory agreement with the measurements were obtained for inflow angles in the linear part of the lift curve i.e. non-separation cases. This numerical model was then extended to include the test section sideplates and constraints to design RVGs for the experimental campaign.

Measurements such as surface pressure, oil flow visualization, Particle Image Velocimetry and acoustic measurements using an array were conducted for airfoils with both natural and forced transition with the same RVGs. To capture the impact of the RVGs on the size of separation for a wind turbine airfoil, oil flow visualization has been conducted. The generation of the streamwise vortices by the rods along with their suppression of the separation zone has been captured in the oil flow visualization technique. Analysis showed a satisfactory reduction of separation zone by the RVGs for airfoils with natural transition ($\sim$45% – 63%). Although the rods decrease the separation zone in airfoils with forced transition ($\sim$23%), their effectiveness could be improved by altering the dimensions of the rods. This is because the geometric size of the RVGs are dependent on the boundary layer characteristics and any modification to the boundary layer such as forced transition (trip-tape) necessitates the alteration of the rod dimensions.

The re-energizing of the boundary layer by the streamwise vortices generated by the rods was assessed through Particle Image Velocimetry measurements. Both the mean and fluctuating components of velocity tangential and normal to the wall were compared for the airfoil equipped with RVGs to the reference airfoil. Furthermore, the boundary layer characteristics were quantified both upstream and downstream of the rods in Chapter 6.

The impact of the rods on the separation noise and the broadband trailing edge noise along with the rod self-noise have been analyzed through the acoustic measurements conducted using microphone array and post-processed through beamforming technique described in section 2.9.1. These analyses have been presented for both the airfoils (with/without RVGs) with natural and forced transition in section 6.5. A comparitive spectral analysis (SPL and OASPL) has been conducted for a range of frequencies. Different sound sources (such as jet nozzle noise, side plate noise, leading edge noise, trailing edge noise etc.) were observed at different frequencies in the contour maps. SPL curves of the reference airfoil were analyzed to observe the impact of increasing inflow angles on the noise emission. They depicted an increase in the overall sound levels emitted due to both, growing boundary layer thickness and turbulent boundary layer separation. The peak values were also found to be shifted to lower frequencies at higher angles.

With the implementation of the rods the separation zone was reduced and consequently a reduction in separation noise is expected. The variation of emitted noise over the frequencies specifically influenced by the rods is case dependent. For instance, a decrease in the emitted noise at low frequencies - particularly up to 1200 Hz at angles where there is no separation and up to 700 Hz at angles where there is a large separation was observed for airfoils with forced transition. However, the rods generate more trailing edge noise at frequencies above these ranges. The streamwise vortices generated by the RVGs energize the boundary layer flow by bringing in high momentum fluid closer to the airfoil surface. The rods impact the vortices in the wake thereby influencing trailing edge noise at certain frequencies. Depending on the strength of the vortices

generated which is a direct consequence of the geometric parameters of the rods, the dominance of the trailing edge noise over the separation noise varies differently as a function of the frequencies. Further research into this hypothesis using detailed analysis (maybe Large Eddy Simulations – LES) is required. The RVGs generate an additional self-noise only at higher frequencies. This self-noise generation is achieved when the acoustic wavelength and the eddies generated by the rods are of comparable size. It is important to note that the increase of noise levels by the rods are all within $\sim$2 dB and occurs at total sound pressure levels which are significantly lower than the peak values generated at low frequencies, thus, making it difficult for human perception specifically for wind turbine applications.

7.2 Future work

The flexibility, capability and generality of the developed aeroacoustic code in terms of analyzing different applications and flow control devices has been successfully demonstrated. The FW–H code is developed in such a way to allow for an easy extension to implement the porous surface formulation of Farassat. This extension would expand the capabilities of the acoustic code furthermore by allowing for investigation of acoustic pressure at higher Mach numbers. Additionally, inclusion of the volumetric source terms will also be possible with the porous surface implementation. This will enable investigation of far-field sound levels using measurement data of stationary airfoils/blades etc. Conversion of the code from Tecplot scripting language to python is another possibility to speed up the computational process thereby reducing computational costs.

List of Figures

List of Tables

Bibliography

[1] B. T. Chu and L. S. G. Kovasznay. Non-linear interactions in a viscous heat-conducting compressible gas. *Journal of Fluid Mechanics*, 3(5):494–514, 1958.

[2] H. S. Ribner. The generation of sound by turbulent jets. *Advances in applied mechanics*, 8:103–182, 1964.

[3] T. Munzel, T. Gori, W. Babisch, and M. Basner. Cardiovascular Effects of Environmental Noise Exposure. *European heart journal*, 35, 03 2014.

[4] M. Basner, M. Brink, Y. de Kluizenaar, Y. Hong, S. Janssen, R. Klaeboe, T. Leroux, A. Liebl, T. Matsui, M. Sliwinska-Kowalska, and P. Sorqvist. Icben review of research on the biological effects of noise 2011-2014. *Noise and Health*, 17, 01 2015.

[5] R.H. Bakker, J. Bouma, Pedersen, Berg, and F. van den Berg. Project WINDFARMperception Visual and acoustic impact of wind turbine farms on residents. *Final Report, University of Groningen*, 01 2008.

[6] H. Davies, Y. Gagnon, T. Guidotti, C. Giguère, S. Grace, B. Howe, D. Johnson, K. Persson Waye, R. Harrison, and J. Roberts. *Understanding the Evidence: Wind Turbine Noise: The Expert Panel on Wind Turbine Noise and Human Health.* 03 2015.

[7] S. Moreau. The Third Age of Aeroacoustics. *Physics of Fluids*, 34(3):031301, 2022.

[8] M. V. Lowson. Applications of aero-acoustic analysis to wind turbine noise control. *Wind Engineering*, pages 126–140, 1992.

[9] C. R. Cox. Aerodynamic sources of rotor noise. *Journal of the American Helicopter Society*, 18(1):3–9, 1973.

[10] M. V. Lowson and J. B. Ollerhead. A theoretical study of helicopter rotor noise. *Journal of Sound and Vibration*, 9(2):197–222, 1969.

[11] M. J. Lighthill and M. H. A. Newman. On sound generated aerodynamically I. General theory. *Proceedings of the Royal Society of London. Series A. Mathematical and Physical Sciences*, 211(1107):564–587, 1952.

[12] S. K. Lele and J. W. Nichols. A second golden age of aeroacoustics? *Philosophical transactions of the Royal Society*, A 372(20130321), 2014.

[13] P. B. Andersen, L. Henriksen, M. Gaunaa, C. Bak, and T. Buhl. Deformable trailing edge flaps for modern megawatt wind turbine controllers using strain gauge sensors. *Wind Energy*, 13(2-3):193–206, 2010.

[14] J. M. Prospathopoulos, V. A. Riziotis, E. Schwarz, T. Barlas, M. Aparicio-Sanchez, G. Papadakis, D. Manolas, G. Pirrung, and T. Lutz. Simulation of oscillating trailing edge flaps on wind turbine blades using ranging fidelity tools. *Wind Energy*, 24(4):357–378, 2021.

[15] M. Hocevar, E. Potocar, B. Sirok, and M. Eberlinc. Control of Separation Flow over a Wind Turbine Blade with Plasma Actuators. *Journal of Mechanical Engineering*, 58:37–45, 01 2012.

[16] L. Guoqiang, Z. Weiguo, J. Yubiao, and Y. Pengyu. Experimental investigation of dynamic stall flow control for wind turbine airfoils using a plasma actuator. *Energy*, 185:90–101, 2019.

[17] S. Y. Lin, Y. Y. Lin, C. J. Bai, and W. C. Wang. Performance analysis of vertical-axis-wind-turbine blade with modified trailing edge through computational fluid dynamics. *Renewable Energy*, 99:654–662, 2016.

[18] D. B. Zadorozhna, O. Benavides, J. S. Grajeda, S. F. Ramirez, and L. C. May. A parametric study of the effect of leading edge spherical tubercle amplitudes on the aerodynamic performance of a 2D wind turbine airfoil at low Reynolds numbers using computational fluid dynamics. *Energy Reports*, 7:4184–4196, 2021.

[19] Z. Zhao, R. Jiang, J. Feng, H. Liu, T. Wang, W. Shen, M. Chen, D. Wang, and Y. Liu. Researches on vortex generators applied to wind turbines: A review. *Ocean Engineering*, 253:111266, 2022.

[20] M. Hansen, C. Velte, S. Oye, R. Hansen, N. Sorensen, J. Madsen, and R. Mikkelsen. Aerodynamically shaped vortex generators. *Wind Energy*, 19, 03 2015.

[21] D. De Tavernier, C. Ferreira, A. Vire, B. LeBlanc, and S. Bernardy. Controlling dynamic stall using vortex generators on a wind turbine airfoil. *Renewable Energy*, 172:1194–1211, 2021.

[22] H. Müller-Vahl, G. Pechlivanoglou, C. Nayeri, and C. Paschereit. Vortex Generators for Wind Turbine Blades: A Combined Wind Tunnel and Wind Turbine Parametric Study. *Proceedings of the ASME Turbo Expo*, 6, 06 2012.

[23] H. Im, S. Kim, and B. Kim. Numerical analysis of the effect of vortex generator on inboard region of wind turbine blade. *Journal of Renewable and Sustainable Energy*, 13(6):063306, 2021.

[24] S. A. Prince, C. Badalamenti, and C. Regas. The application of passive air jet vortex-generators to stall suppression on wind turbine blades. *Wind Energy*, 20(1):109–123, 2017.

[25] S. Shun and N. Ahmed. Utilizing Vortex Acceleration to Improve the Efficiency of Air Jet Vortex Generators. *6th AIAA Flow Control Conference, Louisiana*, 2012.

[26] J. M. Suarez, P. Flaszynski, and P. Doerffer. Application of rod vortex generators for flow separation reduction on wind turbine rotor. *Wind Energy*, 21(11):1202–1215, 2018.

[27] J. M. Suarez, P. Flaszynski, and P. Doerffer. Streamwise vortex generator for separation reduction on wind turbine rotors. *International Journal of Numerical Methods for Heat and Fluid Flow*, 28:1047–1060, 2018.

[28] F. De Gregorio. Helicopter fuselage model drag reduction by active flow control systems. *Journal of the American Helicopter Society*, 64(2):1–15, 2019.

[29] R. P. Patterson, Y. Tan, P. P. Friedmann, and A. Glezer. A Combined Computational and Experimental Study of Active Flow Control for Vibration Reduction on Helicopter Rotors. *AIAA SCITECH 2022 Forum*, page 0325, 2022.

[30] T. Corke and M. Post. Overview of plasma flow control: concepts, optimization, and applications. *43rd AIAA aerospace sciences meeting and exhibit*, page 563, 2005.

[31] W. Stalewski. Flow control on helicopter rotor blades via Active Gurney Flap. *Prace Instytutu Lotnictwa*, 2018.

[32] A. L. Pape, C. Lienard, C. Verbeke, M. Pruvost, and J. L. De Coninck. Helicopter fuselage drag reduction using active flow control: A comprehensive experimental investigation. *Journal of the American Helicopter Society*, 60(3):1–12, 2015.

[33] E. F. Tejero, P. Doerffer, and O. Szulc. Application of a passive flow control device on helicopter rotor blades. *Journal of the American Helicopter Society*, 61(1):1–13, 2016.

[34] Y. Shi, T. Li, X. He, L. Dong, and G. Xu. Helicopter rotor thickness noise control using unsteady force excitation. *Applied Sciences*, 9(7):1351, 2019.

[35] B. W. Sim, R. D. JanakiRam, and B. H. Lau. Reduced in-plane, low-frequency noise of an active flap rotor. *Journal of the American Helicopter Society*, 59(2):1–17, 2014.

[36] P. Flaszynski, R. Szwaba, and P. Doerffer. Comparison of vortex generators effect on shock wave induced separation. *8th AIAA Flow Control Conference*, Washington D. C, 2016.

[37] H. D. Taylor and Hoadley H. H. Application of vortex-generator mixing principle to diffusers. *United Aircraft Corporation, East Hartford*, (R-15064-5), 1948.

[38] R. Wallis and C. Stuart. On the control of shock induced boundary layer separation with discrete jets. *Technical report*, 1958.

[39] John C. Lin. Review of research on low-profile vortex generators to control boundary-layer separation. 38(Issues 4-5):389–420, 2002.

[40] G. Godard and M. Stanislas. Control of a decelerating boundary layer. Part 1: Optimization of passive vortex generators. *Aerospace Science and Technology*, 10:181–191, 04 2006.

[41] C. M. Velte, C. Braud, S. Coudert, and J. M. Foucaut. Vortex Generator Induced Flow in a High Re Boundary Layer. *Journal of Physics: Conference Series*, 555:012102, Dec 2014.

[42] R. Szwaba, P. Flaszynski, and P. Doerffer. Streamwise vortex generation by the rod. *Chinese Journal of Aeronautics*, 32(8):1903–1911, 2019.

[43] T. Lewandowski. *Retractable Rod Vortex Generator*, pages 175–200. Springer International Publishing, 2017.

[44] S. Oerlemans, M. Fisher, T. Maeder, and K. Kogler. Reduction of wind turbine noise using optimized airfoils and trailing-edge serrations. *AIAA journal*, 47(6):1470–1481, 2009.

[45] S. Oerlemans. Reduction of wind turbine noise using blade trailing edge devices. page 3018, 2016.

[46] B. Lyu, M. Azarpeyvand, and S. Sinayoko. Prediction of noise from serrated trailing edges. *Journal of Fluid Mechanics*, 793:556–588, 2016.

[47] S. Oerlemans and P. Fuglsang. Low-noise wind turbine design. *EWEA Workshop, Wind turbine noise: From source to receiver, Said Business School, Oxford, UK*, pages 11–12, 2012.

[48] G. Leventhall and D. Bowdler. Wind Turbine Noise: how it is produced, propagated measured and received. 2011.

[49] K. Hughes. Solar Power vs. Wind Power. `https://www.letsgosolar.com/consumer-education/solar-power-wind-power/`. Accessed: 02.06.2022.

[50] S. Wagner, R. Bareiss, and G. Guidati. *Wind turbine noise*. Springer Science & Business Media, 2012.

[51] M. Roger, C. Schram, and L. De Santana. Reduction of airfoil turbulence-impingement noise by means of leading-edge serrations and/or porous material. *19th AIAA/CEAS aeroacoustics conference*, page 2108, 2013.

[52] W. K. Blake. *Mechanics of flow-induced sound and vibration, Volume 2: Complex flow-structure interactions*. 2017.

[53] S. Buck, S. Oerlemans, and S. Palo. Experimental characterization of turbulent inflow noise on a full-scale wind turbine. *Journal of Sound and Vibration*, 385:219–238, 2016.

[54] T. F. Brooks and M. A. Marcolini. Airfoil tip vortex formation noise. *AIAA journal*, 24(2):246–252, 1986.

[55] S. Oerlemans, P. Sijtsma, and B. M. Lopez. Location and quantification of noise sources on a wind turbine. *Journal of sound and vibration*, 299(4-5):869–883, 2007.

[56] T. F. Brooks, D. S. Pope, and M. A. Marcolini. Airfoil self-noise and prediction. *NASA Technical Report*, (L-16528), 1989.

[57] E. J. G. Arcondoulis, C. J. Doolan, A. C. Zander, and L. A. Brooks. A review of trailing edge noise generated by airfoils at low to moderate Reynolds number. *Acoustics Australia*, 38(3), 2010.

[58] D. J. Moreau, L. A. Brooks, and C. J. Doolan. On the aeroacoustic tonal noise generation mechanism of a sharp-edged plate. *The Journal of the Acoustical Society of America*, 129(4):EL154–EL160, 2011.

[59] S. Wagner, R. Bareiss, and G. Guidati. *Noise mechanisms of wind turbines*. Springer, 1996.

[60] M. J. Lighthill. On sound generated aerodynamically II. Turbulence as a source of sound. *Proceedings of the Royal Society of London. Series A. Mathematical and Physical Sciences*, 222(1148):1–32, 1954.

[61] J. E. F. Williams and L. H. Hall. Aerodynamic sound generation by turbulent flow in the vicinity of a scattering half plane. *Journal of fluid mechanics*, 40(4):657–670, 1970.

[62] L. J. Ayton. Analytic solution for aerodynamic noise generated by plates with spanwise-varying trailing edges. *Journal of Fluid Mechanics*, 849:448–466, 2018.

[63] S. Buck. Measurement of flow separation noise on a full-scale wind turbine. *2018 AIAA/CEAS Aeroacoustics Conference*, page 3462, 2018.

[64] S. Oerlemans. Effect of wind shear on amplitude modulation of wind turbine noise. *International Journal of Aeroacoustics*, 14(5-6):715–728, 2015.

[65] D. Kolkman, L. D. Santana, M. P. J. Sanders, A. V. Garrel, C. H. Venner, and C. Arc. Experimental characterization of vortex generators induced noise of wind turbines. *2018 AIAA/CEAS Aeroacoustics Conference*, 2018.

[66] Y. Suzuki. Analysis of aerodynamic sound source in a stalled airfoil flow. *Proceedings of Inter-Noise 2006*, 2006.

[67] S. Moreau, M. Roger, and J. Christophe. Flow features and self-noise of airfoils near stall or in stall. *15th AIAA/CEAS Aeroacoustics Conference (30th AIAA Aeroacoustics Conference)*, page 3198, 2009.

[68] J. P. Cohen and C. C. Coughlin. Spatial hedonic models of airport noise, proximity and housing prices. *Journal of Regional Science*, 48(5):859–878, 2008.

[69] F. H. Schmitz. The Challenges and Possibilities of a Truly Quiet Helicopter 29th Alexander A. Nikolsky Honorary Lecture. *Journal of the American Helicopter Society*, 61(4):1–33, 2016.

[70] C. R. Cox and R. R. Lynn. A study of the origin and means of reducing helicopter noise. *Technical report, Bell helicopter Textron Inc., Fortworth TX*, (AD0295090), 1962.

[71] H. R. Henderson, R. J. Peegg, and D. A. Hilton. Results of the noise measurement program on a standard and modified OH-6A helicopter. *NASA Technical Report*, (19730021299), 1973.

[72] H. H. Hubbard and D. J. Maglieri. Noise characteristics of helicopter rotors at tip speeds up to 900 feet per second. *The Journal of the Acoustical Society of America*, 32(9):1105–1107, 1960.

[73] T. J. Stuckey and J. O. Goddard. Investigation and prediction of helicopter rotor noise part I. Wessex whirl tower results. *Journal of Sound and Vibration*, 5(1):50–80, 1967.

[74] J. W. Leverton and F. W. Taylor. Helicopter blade slap. *Journal of Sound and Vibration*, 4(3):IN8–357, 1966.

[75] M. V. Lowson. *Some observations on the noise from helicopters*. Institute of Sound and Vibration Research, University of Southampton, 1964.

[76] F. H. Schmitz and D. A. Boxwell. In-Flight Far-Field Measurement of Helicopter Impulsive Noise. *Journal of the American Helicopter Society*, 21(4):2–16, 1976.

[77] D. A. Boxwell and F. H. Schmitz. Full-Scale Measurements of Blade-Vortex Interaction Noise. *Journal of The American Helicopter Society*, 27:11–27, 1982.

[78] D. A. Boxwell and F. H. Schmitz. In-Flight Acoustic Comparison of the 540 and K747 Main Rotors for the AH-1S Helicopter. *Appendix, US Army Aviation Engineering Flight Activity Report 77*, 38, 1979.

[79] R. G. Loewy and L. R. Sutton. A theory for predicting the rotational noise of lifting rotors in forward flight, including a comparison with experiment. *Journal of Sound and Vibration*, 4(3):305–344, 1966.

[80] L. Gutin. On the sound field of a rotating propeller. *NACA Technical Memorandum*, 9(NACA-TM-1195), 1948.

[81] R. Schlegel, R. King, and H. Mull. Helicopter rotor noise generation and propagation. *Technical Report, United Technologies Corp. Stratford CT, Sikorsky Aircraft Div.*, (AD0645884), 1966.

[82] H. H. Hubbard. *Aeroacoustics of flight vehicles: theory and practice*, volume 1258. NASA Office of Management, Scientific and Technical Information Program, 1991.

[83] A. Gessow and G. C. Myers. *Aerodynamics of the Helicopter*. Burns & Oates, 1952.

[84] K. S. Brentner and F. Farassat. Modeling aerodynamically generated sound of helicopter rotors. *Progress in aerospace sciences*, 39(2-3):83–120, 2003.

[85] S. A. Jacklin, A. Blaas, D. Teves, R. Kube, and W. Warmbrodt. Reduction of helicopter BVI noise, vibration, and power consumption through individual blade control. *AHS 51st Annual Forum and Technology Display*, 1994.

[86] P. Beaumier, B. Van Der Wall, K. Pengel, C. Kessler, M. Gervais, Y. Delrieux, J. F. Hirsch, and P. Crozier. From ERATO Basic Research to the Blue EdgeTM Rotor Blade: an Example of Virtual Engineering. *Rotorcraft Virtual Engineering Conference*, (hal-01413109), 2016.

[87] M. Roger, C. Schram, and S. Moreau. On Open-Rotor Blade-Vortex Interaction Noise. In *18th AIAA/CEAS Aeroacoustics Conference (33rd AIAA Aeroacoustics Conference)*, page 2216, 2012.

[88] A. R. George and S. T. Chou. A comparative study of tail rotor noise mechanisms. *Journal of the American Helicopter Society*, 31(4):36–42, 1986.

[89] E. Greenwood and F. H. Schmitz. Separation of main and tail rotor noise from ground-based acoustic measurements. *Journal of Aircraft*, 51(2):464–472, 2014.

[90] J. E. F. Williams. Sound sources in aerodynamics-Fact and fiction. *AIAA Journal*, 20(3):307–315, 1982.

[91] C. Schram and G. J. Bennett. Aeroacoustics research in Europe: The CEAS-ASC report on 2022 highlights. *Journal of Sound and Vibration*, 568:117895, 2024.

[92] C. K. W. Tam. Computational aeroacoustics: an overview of computational challenges and applications. *International Journal of Computational Fluid Dynamics*, 18(6):547–567, 2004.

[93] T. Colonius and S. K. Lele. Computational aeroacoustics: progress on nonlinear problems of sound generation. *Progress in Aerospace sciences*, 40(6):345–416, 2004.

[94] W. De Roeck, W. Desmet, M. Baelmans, and P. Sas. On the prediction of near-field cavity flow noise using different CAA techniques. *Aeroacoustics and Flow Noise Proceedings of ISMA*, pages 369–386, 2004.

[95] B. Vanelderen, W. De Roeck, and W. Desmet. Flow noise prediction of confined flows using synthetic turbulence and linearized Euler equations in a hybrid methodology. page 2267, 2013.

[96] B. Knaepen, O. Debliquy, and D. Carati. Subgrid-scale energy and pseudo pressure in large-eddy simulation. *Physics of fluids*, 14(12):4235–4241, 2002.

[97] C. Bailly, C. Bogey, and O. Marsden. Progress in direct noise computation. *International Journal of Aeroacoustics*, 9(1-2):123–143, 2010.

[98] L. Quartapelle and V. Selmin. High-order Taylor-Galerkin methods for nonlinear multidimensional problems. *Finite Elements in Fluids*, 76(90):46, 1993.

[99] A. Fosso Pouangue, M. Sanjose, S. Moreau, G. Daviller, and H. Deniau. Subsonic jet noise simulations using both structured and unstructured grids. *Aiaa Journal*, 53(1):55–69, 2015.

[100] J. Utzmann, T. Schwartzkopff, M. Dumbser, and C. D. Munz. Heterogeneous domain decomposition for computational aeroacoustics. *AIAA journal*, 44(10):2231–2250, 2006.

[101] D. Flad, A. D. Beck, G. Gassner, and C. D. Munz. A discontinuous Galerkin spectral element method for the direct numerical simulation of aeroacoustics. page 2740, 2014.

[102] R. Leger, C. Peyret, and S. Piperno. Coupled discontinuous Galerkin/finite difference solver on hybrid meshes for computational aeroacoustics. *AIAA journal*, 50(2):338–349, 2012.

[103] S. Moreau. Direct noise computation of low-speed ring fans. *Acta Acustica united with Acustica*, 105(1):30–42, 2019.

[104] S. Marie, D. Ricot, and P. Sagaut. Comparison between lattice Boltzmann method and Navier–Stokes high order schemes for computational aeroacoustics. *Journal of Computational Physics*, 228(4):1056–1070, 2009.

[105] T. Colonius. Modeling artificial boundary conditions for compressible flow. *Annual review of fluid mechanics*, 36:315–345, 2004.

[106] T. J. Poinsot and S. K. Lelef. Boundary conditions for direct simulations of compressible viscous flows. *Journal of computational physics*, 101(1):104–129, 1992.

[107] X. Gloerfelt and J. C. Robinet. Silent inflow condition for turbulent boundary layers. *Physical Review Fluids*, 2(12):124603, 2017.

[108] C. K. W. Tam and Z. Dong. Radiation and outflow boundary conditions for direct computation of acoustic and flow disturbances in a nonuniform mean flow. *Journal of computational acoustics*, 4(02):175–201, 1996.

[109] H. Si, W. Shen, and W. Zhu. Effect of non-uniform mean flow field on acoustic propagation problems in computational aeroacoustics. *Aerospace Science and Technology*, 28(1):145–153, 2013.

[110] C. Bailly and D. Juve. Numerical solution of acoustic propagation problems using linearized Euler equations. *AIAA journal*, 38(1):22–29, 2000.

[111] P. Davies and K. R. Holland. The measurement and prediction of sound waves of arbitrary amplitude in practical flow ducts. *Journal of sound and vibration*, 271(3-5):849–861, 2004.

[112] R. Ewert and W. Schroder. Acoustic perturbation equations based on flow decomposition via source filtering. *Journal of Computational Physics*, 188(2):365–398, 2003.

[113] J. H. Seo and Y. J. Moon. Perturbed compressible equations for aeroacoustic noise prediction at low mach numbers. *AIAA journal*, 43(8):1716–1724, 2005.

[114] P. E. Doak. Analysis of internally generated sound in continuous materials: 2. A critical review of the conceptual adequacy and physical scope of existing theories of aerodynamic noise, with special reference to supersonic jet noise. *Journal of Sound and Vibration*, 25(2):263–335, 1972.

[115] J. W. S. B. Rayleigh. *The theory of sound*, volume 2. Macmillan & Company, 1896.

[116] I. E. Garrick and C. E. Watkins. A theoretical study of the effect of forward speed on the free-space sound-pressure field around propellers. *Nasa Technical Report*, 1953.

[117] A. F. Deming. Noise from propellers with symmetrical sections at zero blade angle, II. *Nasa Technical Report*, 1938.

[118] F. Farassat and M. K. Myers. Extension of Kirchhoff's formula to radiation from moving surfaces. *Journal of Sound and Vibration*, 123(3):451–460, 1988.

[119] F. Farassat and M. K. Myers. The Kirchhoff formula for a supersonically moving surface. (95-062), 1996.

[120] P. Di Francescantonio. A new boundary integral formulation for the prediction of sound radiation. *Journal of Sound and Vibration*, 202(4):491–509, 1997.

[121] K. S. Brentner and F. Farassat. Analytical comparison of the acoustic analogy and Kirchhoff formulation for moving surfaces. *AIAA journal*, 36(8):1379–1386, 1998.

[122] F. Farassat. The Kirchhoff formulas for moving surfaces in aeroacoustics-the subsonic and supersonic cases. *Journal of Sound and Vibration*, 230(2):460–462, 2000.

[123] J. E. Ffowcs-Williams and D. L. Hawkings. Sound generation by turbulence and surfaces in arbitrary motion. *Philosophical transactions of the Royal Society of London A: Mathematical, Physical and Engineering Sciences*, 264:321–342, 1969.

[124] N. Curle. The influence of solid boundaries upon aerodynamic sound. *Proceedings of the Royal Society of London. Series A. Mathematical and Physical Sciences*, 231(1187):505–514, 1955.

[125] S. W. Rienstra and A. Hirschberg. An introduction to Acoustics. *Technische Universiteit Eindhoven*, 0103, 2001.

[126] F. Farassat. Derivation of Formulations 1 and 1A of Farassat. *NASA Technical Report*, 214853(TM-2007-214853):1–25, 2007.

[127] D. S. Jones. *The theory of generalised functions*, volume 539. Cambridge University Press Cambridge, 1982.

[128] R. P. Kanwal. *Generalized functions theory and technique: Theory and technique.* Springer Science & Business Media, 1998.

[129] F. Farassat. *Introduction to generalized functions with applications in aerodynamics and aeroacoustics*, volume 3428. National Aeronautics and Space Administration, Langley Research Center, 1994.

[130] R. Aris. *Vectors, tensors and the basic equations of fluid mechanics.* Courier Corporation, 2012.

[131] F. Farassat. Theory of noise generation from moving bodies with an application to helicopter rotors. *NASA Technical Report*, 1975.

[132] F. Farassat and G. P. Succi. A review of propeller discrete frequency noise prediction technology with emphasis on two current methods for time domain calculations. *Journal of Sound and Vibration*, 71(3):399–419, 1980.

[133] F. Farassat and K. S. Brentner. The uses and abuses of the acoustic analogy in helicopter rotor noise prediction. *Journal of the American Helicopter Society*, 33(1):29–36, 1988.

[134] F. Farassat. Linear acoustic formulas for calculation of rotating blade noise. *AIAA journal*, 19(9):1122–1130, 1981.

[135] C. Hansen. Fundamentals of acoustics. *American Journal of Physics*, 19, 1951.

[136] M. V. Lowson. The sound field for singularities in motion. *Proceedings of the Royal Society of London. Series A. Mathematical and Physical Sciences*, 286(1407):559–572, 1965.

[137] G. Herold and E. Sarradj. Performance analysis of microphone array methods. *Journal of Sound and Vibration*, 401:152–168, 2017.

[138] C. S. Allen, W. K. Blake, R. P. Dougherty, D. Lynch, P. T. Soderman, and J. R. Underbrink. *Aeroacoustic measurements*. Springer Science & Business Media, 2002.

[139] S. Oerlemans. *Detection of aeroacoustic sound sources on aircraft and wind turbines*. PhD thesis, University of Twente, Netherlands, September 2009.

[140] L. de Santana. Fundamentals of acoustic beamforming. *Design and Operation of Aeroacoustic Wind Tunnel Tests for Group and Air Transport*, 2017.

[141] P. Welch. The use of fast Fourier transform for the estimation of power spectra: a method based on time averaging over short, modified periodograms. *IEEE Transactions on audio and electroacoustics*, 15(2):70–73, 1967.

[142] T. F. Brooks and W. M. Humphreys. A deconvolution approach for the mapping of acoustic sources (DAMAS) determined from phased microphone arrays. *Journal of sound and vibration*, 294(4-5):856–879, 2006.

[143] R. P. Dougherty, R. C. Ramachandran, and G. Raman. Deconvolution of sources in aeroacoustic images from phased microphone arrays using linear programming. *International Journal of Aeroacoustics*, 12(7-8):699–717, 2013.

[144] A. M. N. Malgoezar, M. Snellen, R. Merino-Martinez, D. G. Simons, and P. Sijtsma. On the use of global optimization methods for acoustic source mapping. *The Journal of the Acoustical Society of America*, 141(1):453–465, 2017.

[145] P. Sijtsma. CLEAN based on spatial source coherence. *International journal of aeroacoustics*, 6(4):357–374, 2007.

[146] S. T. Funke, R. P. Dougherty, and U. Michel. SODIX in comparison with various deconvolution methods. *5th Berlin beamforming conference*, 2014.

[147] E. Sarradj. A fast signal subspace approach for the determination of absolute levels from phased microphone array measurements. *Journal of Sound and Vibration*, 329(9):1553–1569, 2010.

[148] P. Sijtsma, R. Merino-Martinez, A. Malgoezar, and M. Snellen. High-resolution CLEAN-SC: Theory and experimental validation. *International Journal of Aeroacoustics*, 16:274–298, 2017.

[149] S. Luesutthiviboon, A. M. N. Malgoezar, R. Merino-Martinez, M. Snellen, P. Sijtsma, and D. G. Simons. Enhanced HR-CLEAN-SC for resolving multiple closely spaced sound sources. *International Journal of Aeroacoustics*, 18(4-5):392–413, 2019.

[150] T. Suresh, O. Szulc, and P. Flaszynski. Aeroacoustic analysis based on fw–h analogy to predict low-frequency in-plane harmonic noise of a helicopter rotor in hover. *Archives of Mechanics*, 74(2-3):201–246, 2022.

[151] Tecplot Inc. Tecplot 360 EX 2022 Release 1 - User Manual. `https://tecplot.azureedge.net/products/360/current/360_users_manual.pdf`. Accessed: 02.06.2022.

[152] T. Suresh, O. Szulc, P. Flaszynski, and P. Doerffer. Prediction of helicopter rotor noise in hover using FW-H analogy. In *Journal of physics: Conference series*, volume 1101, page 012041. IOP Publishing, 2018.

[153] J. G. Leishman. Principles of Helicopter Aerodynamics, Chapter 3: Blade Element Analysis. *Cambridge University Press*, pages 115–170, 2006.

[154] A. Jirasek. Vortex-generator model and its application to flow control. *Journal of Aircraft*, 42(6):1486–1491, 2005.

[155] F. H. Schmitz and Y. H. Yu. Helicopter impulsive noise: Theoretical and experimental status. *Journal of Sound and Vibration*, 109(3):361–422, 1986.

[156] G. Gopalan and F. H. Schmitz. Understanding Far Field Near-In-Plane High Speed Harmonic Helicopter Rotor Noise in Hover and Forward Flight: Governing Parameters and Design Trends. *American Helicopter Society Technical Specialists' Conference*, 2008.

[157] D. Sargent and F. H. Schmitz. Fundamental Experimental studies supporting Active-Jet Acoustic Control of In-plane Rotor Harmonic noise. *Journal of Aircraft*, 51(2):434–446, 2014.

[158] E. Greenwood and F. H. Schmitz. The Effects of Ambient Conditions on Helicopter Rotor Source Noise Modeling. *American Helicopter Society 67th Annual Forum*, 05 2011.

[159] O. Szulc. Rotorcraft thickness noise control. *Archives of Mechanics*, 73(4):391–417, 2021.

[160] M. M. Hand, D. A. Simms, L. J. Fingersh, D. W. Jager, J. R. Cotrell, S. Schreck, and S. M. Larwood. Unsteady aerodynamics experiment phase VI: wind tunnel test configurations and available data campaigns. Technical report, 2001.

[161] Q. Ye, F. Avallone, W. Van Der Velden, and D. Casalino. Effect of vortex generators on NREL wind turbine: aerodynamic performance and far-field noise. In *Journal of Physics: Conference Series*, volume 1618, page 052077. IOP Publishing, 2020.

[162] A. Suryadi and M. Herr. Wall pressure spectra on a DU96-W-180 profile from low to pre-stall angles of attack. *21st AIAA/CEAS Aeroacoustic conference*, Texas, 2015.

[163] P. Spalart and S. Allmaras. A One-Equation Turbulence Model for Aerodynamic Flows. *AIAA*, 439, 1992.

[164] F. R. Menter, A. V. Garbaruk, and Y. Egorov. Explicit algebraic reynolds stress models for anisotropic wall-bounded flows. *EUCASS Proceedings Series - Advances in AeroSpace Sciences*, 3:89–104, 2012.

[165] B. I. Celik, U. Ghia, P. J. Roache, and F. J. Christopher. Procedure for estimation and reporting of uncertainty due to discretization in CFD applications. *Journal of fluids Engineering-Transactions of the ASME*, 130(7), 2008.

[166] A. Gardner and K. Richter. Effect of the Model-Sidewall Connection for a Static Airfoil Experiment. *Journal of Aircraft*, 50:677–680, 2013.

[167] N. Tiwari, P. Flaszynski, T. Suresh, and O. Szulc. Comparison of flow structures for vane and rod type vortex generators on a wind turbine airfoil. *International Journal of Numerical Methods for Heat & Fluid Flow*, 33(4), 2023.

[168] J. Westerweel. Fundamentals of digital particle image velocimetry. *Measurement science and technology*, 8(12):1379, 1997.

[169] F. Scarano. Iterative image deformation methods in PIV. *Measurement science and technology*, 13(1):R1, 2001.

[170] B. Wieneke. PIV uncertainty quantification from correlation statistics. *Measurement Science and Technology*, 26(7):074002, 2015.

[171] A. R. Carpio, R. M. Martinez, F. Avallone, D. Ragni, M. Snellen, and S. van der Zwaag. Experimental characterization of the turbulent boundary layer over a porous trailing edge for noise abatement. *Journal of Sound and Vibration*, 443:537–558, 2019.

[172] J. R. Underbrink. Circularly symmetric, zero redundancy, planar array having broad frequency range applications, US6205224B1, March 2001.

[173] Z. Prime and C. Doolan. A comparison of popular beamforming arrays. *Proceedings of Acoustics*, 2013.

[174] E. Sarradj. Three-Dimensional Acoustic Source Mapping with Different Beamforming Steering Vector Formulations. *Advances in Acoustics and Vibration*, 2012.

[175] R. M. Martinez, S. Luesutthiviboon, R. Zamponi, A. R. Carpio, D. Ragni, P. Sijtsma, M. Snellen, and C. Schram. Assessment of the accuracy of microphone array methods for aeroacoustic measurements. *Journal of Sound and Vibration*, 470:115176, 2020.

[176] F. R. S. Lord Rayleigh. XXXI. Investigations in optics, with special reference to the spectroscope. *The London, Edinburgh, and Dublin Philosophical Magazine and Journal of Science*, 8(49):261–274, 1879.

[177] T. Brooks and W. Humphreys. Effect of Directional Array Size On The Measurement of Airframe Noise Components. *5th AIAA/CEAS Aeroacoustics Conference and Exhibit*, 1999.

[178] T. Padois, C. Prax, and V. Valeau. Numerical validation of shear flow corrections for beamforming acoustic source localisation in open wind-tunnels. *Applied Acoustics*, 74(4):591–601, 2013.

[179] P. Doerffer and J. Amecke. Secondary Flow Control and Streamwise Vortices Formation. *ASME 1994 International Gas Turbine and Aeroengine Congress and Exposition*, 1, 1994.

[180] F. H. Clauser. The turbulent boundary layer. *Advances in applied mechanics*, 4:1–51, 1956.

[181] L. J. Souverein and J. F. Debiève. Effect of air jet vortex generators on a shock wave boundary layer interaction. *Experiments in Fluids*, 49(5):1053–1064, 2010.

[182] R. Puzyrewski and J. Sawicki. *Podstawy mechaniki plynow i hydrauliki.* Wydawnictwo Naukowe PWN, 1987.

[183] G. Desquesnes, M. Terracol, and P. Sagaut. Numerical investigation of the tone noise mechanism over laminar airfoils. *Journal of Fluid Mechanics*, 591:155–182, 2007.

[184] C. W. Knisely. Strouhal numbers of rectangular cylinders at incidence: A review and new data. *Journal of Fluids and Structures*, 4(4):371–393, 1990.

Appendix A

Validation of the developed FW–H code

A.1 Data range required for frequency analysis

To conduct analysis of all the noise metrics (amplitude, P_{rms}, frequency, SPL and OASPL), especially in the frequency domain, the predicted signals have to contain a certain number of periods of revolution to ensure sufficient, repeatable data is available for the frequency analysis. To determine the number of revolutions required, a convergence study for the analytical solution is conducted for the most sensitive parameter - frequency presented in the following table.

Tab. A.1.1. Time domain analysis

No. of periods	Frequency (Hz)	Error (%)
Theoretical	100	–
$1T$	102.29	2.29
$2T$	100.00	0.0000022
$1000T$	100.00	0.0000003

From the table, atleast two periods of revolution is necessary to ensure there is no significant influence on the noise metrics. Although data with even more revolutions present less error, they are computationally expensive and not really necessary. Hence, the signals presented in the thesis are all computed for two full periods of revolution.

A.2 Convergence studies for stationary monopole

Grid, time-step resolution and radius dependencies for a stationary source (section 3.4) are presented in the Table A.2.1. The sound characteristics (P_{rms}, OASPL and the frequency of the first harmonic) are presented below. The error percentages are computed against the analytical solution.

Tab. A.2.1. Convergence studies (time-step, grid and radius) for a stationary monopole.

		P_{rms}	OASPL	Frequency
Analytical	-	0.195 Pa	86.887 dB	100.006 Hz

	Resolution	P_{rms} Error (%)	OASPL Error (dB)	Frequency Error (%)
FW–H code Time-step dependency (Fine grid and radius)	Coarse	-0.67	-0.04	0.25
	Medium	-0.53	-0.03	0.08
	Fine∗	-0.47	-0.02	0.05
FW–H code Grid dependency (Fine time-step and radius)	Coarse	-6.53	-0.32	0.68
	Medium	-1.72	-0.08	0.12
	Fine∗	-0.47	-0.02	0.05
FW–H code Radius dependency (Fine time-step and grid)	Coarse	-0.54	-0.04	0.25
	Medium	-0.52	-0.03	0.18
	Fine∗	-0.47	-0.02	0.05

∗ indicates identical case.

A.3 Acoustic components for various stationary dipoles

The FW–H code prediction of the components of the acoustic pressure signal for the out-of-disc-plane (OD) observer described in section 3.5 are presented below.

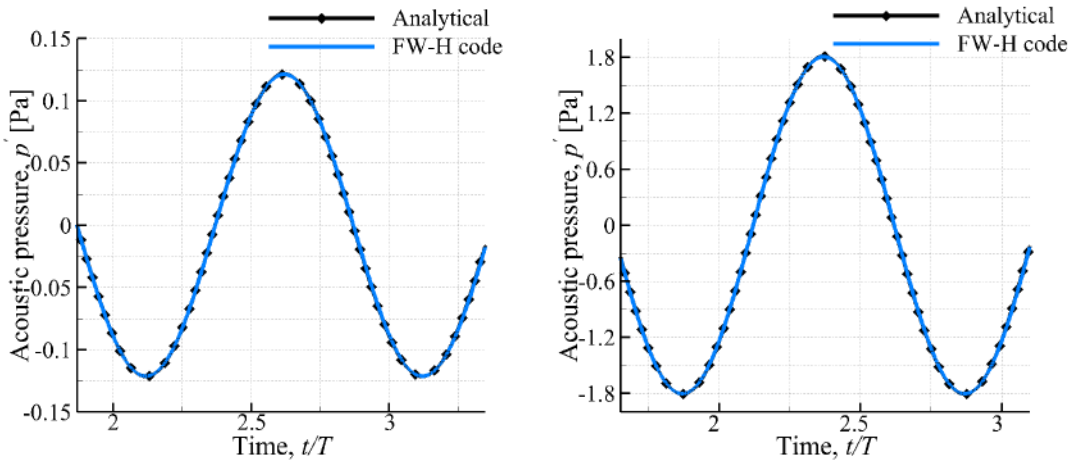

(a) Near-field (b) Far-field

Fig. A.3.1. Acoustic signal components for disc of radius 0.006 25 m, 1280 source cells, $\triangle t$ = T/720 for OD.

Both the near- and far-field components are in good agreement with the analytical solution. For this particular observer position, the far-field component is predominant over the near-field signal.

The FW–H code prediction of the components of the acoustic pressure signal for the in-disc-plane (ID) and on-axis (RD) forces described in section 3.5 are presented in Figures A.3.2 and A.3.3. All the signals are in good agreement with the analytical

solution. For both these dipoles, the far-field component contributes significantly to the total acoustic pressure.

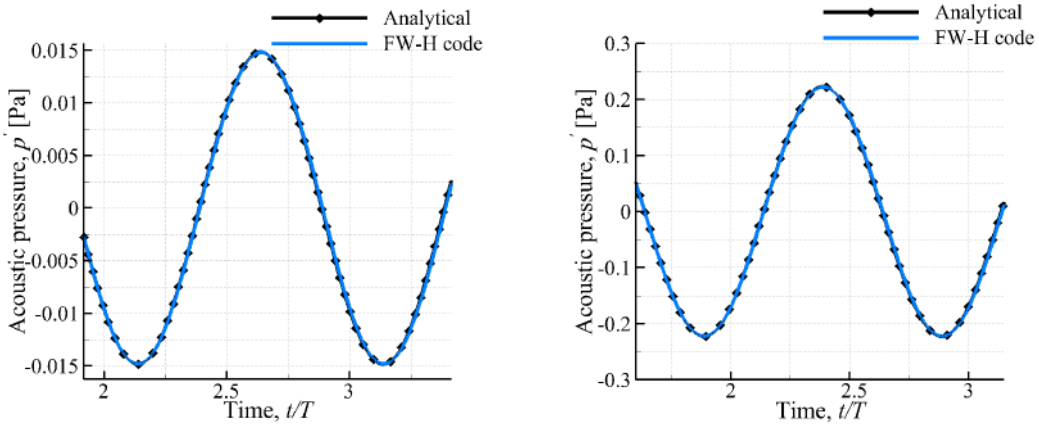

(a) Near-field (b) Far-field

Fig. A.3.2. Acoustic signal components for disc of radius 0.006 25 m, 1445 source cells, $\triangle t$ = T/720 for ID.

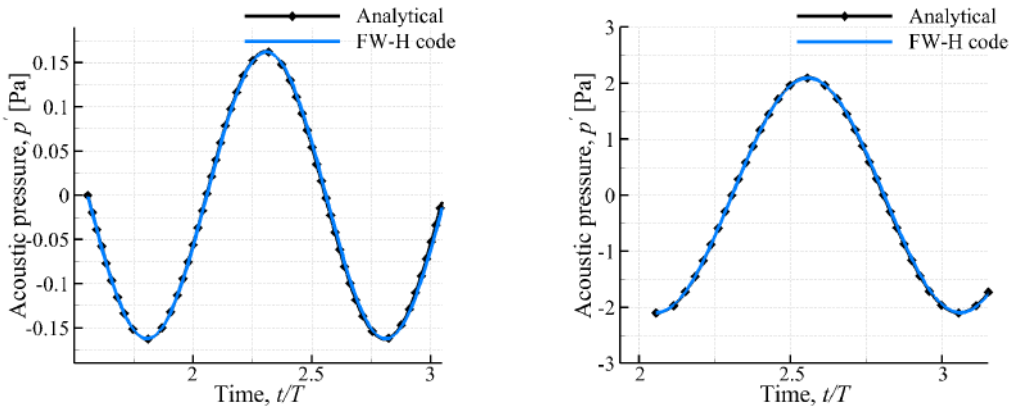

(a) Near-field (b) Far-field

Fig. A.3.3. Acoustic signal components for disc of radius 0.006 25 m, 1445 source cells, $\triangle t$ = T/720 for RD.

A.4 Convergence studies for rotating source

Grid and time-step resolution dependencies along with the execution time for a rotating source (section 3.6) are presented in the Tables A.4.1. The characteristics of sound such as the P_{rms}, OASPL and the frequency of the first harmonic are presented below. The error percentages are computed against the analytical solution.

Tab. A.4.1. Convergence studies (grid and time-step) for a rotating source.

		P_{rms}	OASPL	Frequency
Analytical	-	0.313 Pa	83.879 dB	36.082 Hz

	Resolution	P_{rms} Error (%)	OASPL Error (dB)	Frequency Error (%)
FW–H code Grid dependency (Fine time-step)	Coarse	3.3	0.3	0.5
	Medium	0.9	0.1	0.5
	Fine∗	0.3	<0.1	0.4
FW–H code Time-step dependency (Fine grid)	Coarse	0.6	0.1	0.6
	Medium	0.5	<0.1	0.5
	Fine∗	0.3	<0.1	0.4

∗ indicates identical case.

From the data analysis of the tables, we can infer that for all elementary cases, an insufficient spatial resolution affects the peak amplitude of the signal thus impacting P_{rms} and OASPL values. Time-step resolution predominantly affects the frequency and the phase of the signal. The error in phase difference is not an issue in case of individual sources but becomes very significant when distributed source addition is required. For instance, a tiny phase shift error in individual source/sink leads to non trivial errors while adding source-sink pair that mimics thickness noise generation. Hence, even though fine time-step (T/720) satisfies the criterion of error <0.5%, to better fit the SPL curves and phase of the added signal, very fine time-step (T/5760) solutions are presented in section 3.6.

The dependencies (grid and time-step) are presented for the rotating source case only as the source and sink grids (sphere) are identical (Figure 3.6.10). The total signal emitted by the source-sink pair is obtained by adding the converged solution from individual source and sink (Figure 3.6.13). The phase of the signal is the most important characteristic for addition thus necessitating very fine time-steps (T/5760). It can also be noted that the computation time is a function mainly of the time-step thus increasing the resolution in time increases the run time.

A.5 Acoustic components and convergence studies for various rotating dipoles

The FW–H code prediction of the components of the acoustic pressure signal for the various rotating forces described in section 3.7 are presented below.

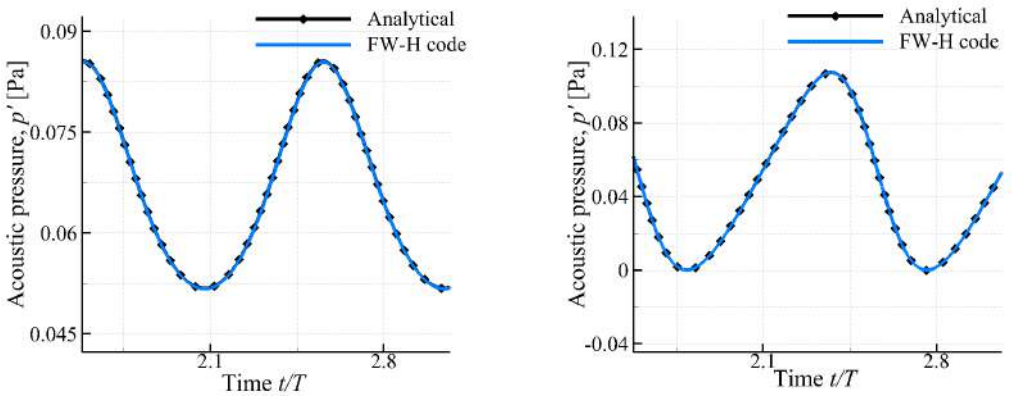

(a) Near-field (b) Far-field

Fig. A.5.4. Acoustic pressure (p') signal components for a rotating out-of-plane force.

For the out-of-plane dipole, both the near- and far-field components of the acoustic pressure pulse are of similar nature (almost harmonic), only slightly delayed in relation to each other (nearly in-phase) – see Figures 3.7.15a, 3.7.15b. For the chosen out-of-plane and radial observer locations, the far-field component of the signal is predominant over the near-field one (Figures A.5.5 and A.5.6).

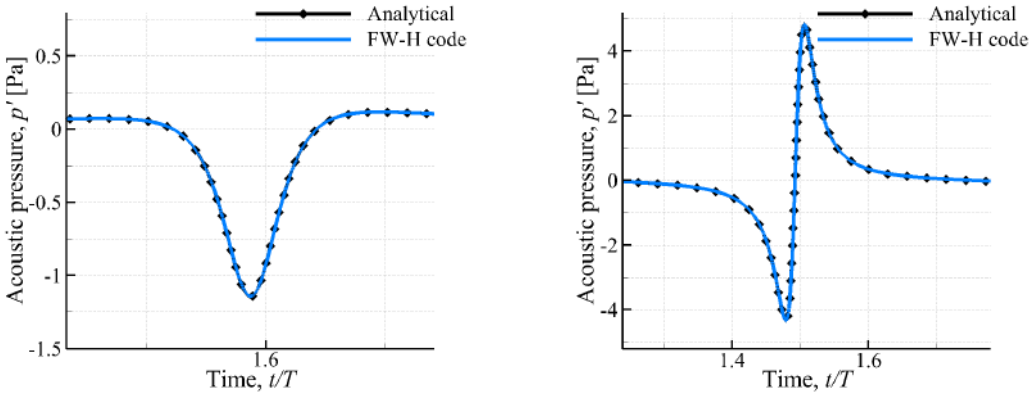

(a) Near-field (b) Far-field

Fig. A.5.5. Acoustic pressure (p') signal components for a rotating in-plane force.

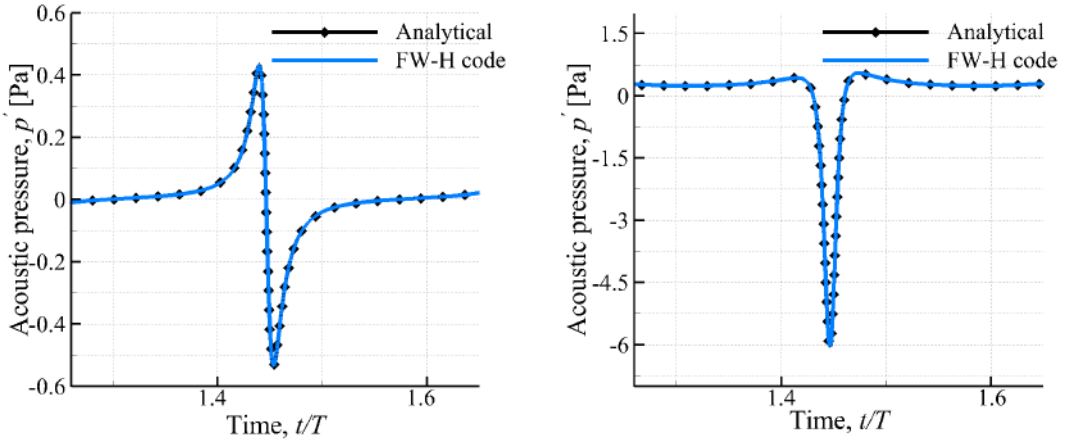

(a) Near-field (b) Far-field

Fig. A.5.6. Acoustic pressure (p') signal components for a rotating radial force.

Grid and time-step resolution dependencies along with the execution time for a rotating in-plane force (section 3.7) are presented in the Table A.5.1. The characteristics of sound such as the P_{rms}, OASPL and the frequency of the first harmonic are presented below. The error percentages are computed against the analytical solution.

Tab. A.5.1. Convergence studies (grid and time-step) for a rotating in-plane force.

		P_{rms}	OASPL	Frequency	Run-time
Analytical	-	1.414 Pa	96.99 dB	36.367 Hz	33 s

	Resolution	P_{rms} Error (%)	OASPL Error (dB)	Frequency Error (%)	Run time (min)
FW–H code Grid dependency (Fine time-step)	Coarse	1.04	0.1	<0.1	3
	Medium	0.66	<0.1	<0.1	9
	Fine∗	0.15	<0.1	<0.1	34
FW–H code Time-step dependency (Fine grid)	Coarse	0.29	<0.1	0.7	3
	Medium	0.17	<0.1	0.1	11
	Fine∗	0.15	<0.1	<0.1	34

∗ indicates identical case.

Only one of the forces - the rotating in-plane force dependencies are presented here since the grid used for all of the forces are identical (Figure 3.7.14). Similar trends in the characteristics are observed for the three cases. Although the fine time-step solution (∗) satisfies the <0.5% error criterion, but, to improve the phase of the signal and to be compatible with the previous case (section 3.6), solutions of very fine time-step (T/5760) are presented in Figures 3.7.17 and 3.7.16. The acoustic computation time for the converged in-plane force (34 min) is lesser than the run time for the converged rotating source prediction (44 min). This is because the rotating source of mass grid has more surface panels (1536 cells) than the rotating in-plane force grid (1280 cells), previously described in Chapter 3.

Appendix B

DC shift of signals

The acoustic signals predicted by the aeroacoustic code based on the FW–H analogy for out-of-plane microphone locations have a large constant term. This constant term is a result of the Fourier transformation of the pressure signal, a technique utilized in the derivation of the integral solution (Farassat Formulations) to the exact FW–H equation (see section 2.6). For example, the total acoustic pressure for the out-of-plane M2 microphone for the reference rotor blades is presented in Figure B.0.1. In this plot, the red curve represents the original signal predicted by the code while the black line is obtained from removing the constant term from the original signal (red line). The signal with the DC shift is varying about a certain mean value (0.74) which is not equal to the ambient pressure. This non-zero constant term is removed from the signal to obtain the variation of the pressure about the ambient conditions denoted by 0 (black curve). This DC shift removal is performed for all signals presented in Chapter 5, otherwise the resulting SPL amplitudes values will be exaggerated.

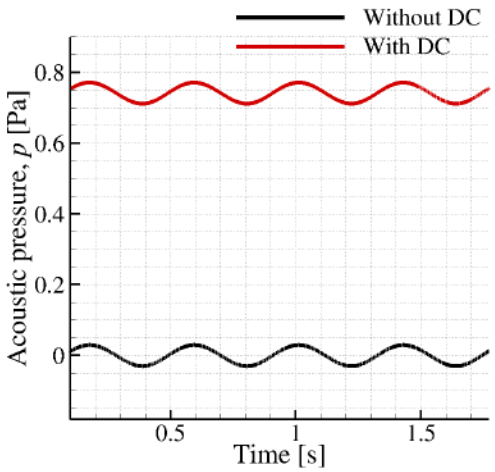

Fig. B.0.1. FW–H body definition.